Volumetric Data Analysis for Reverse Engineering and Solid Additive Manufacturing: A Framework for Geometric Metrological Analysis

by

Zhaohui Geng

Master of Arts in Statistics, University of Pittsburgh, 2018

Master of Science in Industrial Engineering, University of Pittsburgh, 2016

Bachelor of Engineering in Electronic Science and Technology, Nankai University, 2014

Submitted to the Graduate Faculty of
the Swanson School of Engineering in partial fulfillment
of the requirements for the degree of

Doctor of Philosophy

University of Pittsburgh

2021

UNIVERSITY OF PITTSBURGH

SWANSON SCHOOL OF ENGINEERING

This dissertation was presented

by

Zhaohui Geng

It was defended on

April 26, 2021

and approved by

Bopaya Bidanda, Ph.D., Ernest E. Roth Professor, Department of Industrial Engineering

Arman Sabbaghi, Ph.D., Associate Professor, Department of Statistics, Purdue University

Xiayun Zhao, Ph.D., Assistant Professor, Departmental of Mechanical Engineering and Material Science

Jayant Rajgopal, Ph.D., Professor, Department of Industrial Engineering

Mostafa Bedewy, Ph.D., Assistant Professor, Department of Industrial Engineering

Dissertation Director: Bopaya Bidanda, Ph.D., Ernest E. Roth Professor, Department of Industrial Engineering

Volumetric Data Analysis for Reverse Engineering and Solid Additive Manufacturing: A Framework for Geometric Metrological Analysis

Zhaohui Geng, PhD

University of Pittsburgh, 2021

Poor geometric quality is one of the main constraints that hinders the wide adoption of reverse engineering (RE) and additive manufacturing (AM). RE models from a single scan will most likely generate inaccurate representations of the original design due to the uncertainties existing in individual parts and scanning procedures. On the other hand, metrological methodologies for AM significantly differ from those for the traditional manufacturing processes. Conventional statistical methodologies overlook these three-dimensional (3D) feature-independent processing techniques.

In this dissertation, we develop a novel statistical data analysis framework—volumetric data analysis (VDA)—to deal with the uniqueness of both technologies. In general, this framework also addresses the rising analytical needs of 3D geometric data. Through VDA, we can simultaneously analyze the measured points on the outer surfaces and their relationships to acquire manufacturing knowledge. The main goal of this dissertation is to apply the proposed framework in multiple RE and AM applications related to their geometric quality characteristics.

First, we demonstrate a novel estimator to increase the precision of RE-generated models. We built a Bayesian model with prior domain knowledge to model the landmarks' uncertainty. We also proposed a bi-objective optimization model to answer the RE process-planning questions, e.g., how many scans and parts are required to achieve the precision requirements.

The second major contribution is a study of tolerance estimation procedure for the remanufacturing of legacy parts. We propose a systematic geometric inspection methodology for the RE and AM systems. Moreover, based on the domain knowledge in production-process design and planning, we developed methods to estimate empirical tolerances from a small batch of legacy parts.

The third major contribution of this dissertation is to design an automated variance modeling algorithm for 3D scanners. The algorithm utilizes a physical object's local geometric descriptors and Bayesian extreme learning machines to predict the landmarks' variances.

Lastly, we introduce the VDA framework to AM-oriented experimental analysis. Specifically, we propose a high-dimensional hypothesis testing procedure to statistically compare the geometric production accuracy under two AM process settings. We present new visualization tools for deviation diagnostics to aid in interpreting and comparing the process outputs.

Table of Contents

List of Tables

List of Figures

Preface

This dissertation is the final work of my graduate studies at the University of Pittsburgh (Pitt). It serves as documentation of my student life and research during this period. It presents the combined results of three major fields in which I have been working: industrial engineering, statistics, and advanced manufacturing. At Pitt, I have had the most memorable and valuable time in my life. I want to take this opportunity to express my sincere thanks to many people for being with me during this experience.

At the very beginning, I would like to extend my deepest gratitude to my advisor, Dr. Bopaya Bidanda, for his extraordinary guidance, constant support, and insightful advice. His vision, knowledge, and encouragement always inspired me and helped me overcome many obstacles in my personal and professional life. Without him, the research would not have been as successful or as enjoyable. He is not only my role model as a great researcher, but he is also an exemplary mentor. Dr. Bidanda has made me become a better version of myself than I could ever be without his constant help.

I want to extend a special thanks to my committee. I sincerely appreciate Dr. Arman Sabbaghi for his many thoughtful and insightful suggestions and valuable comments. I am also grateful to Drs. Jayant Rajgopal, Xiayun Zhao, and Mostafa Bedewy for their time, generous support, and critical insights along this journey.

Special thanks are due to Dr. Joel Haight. He first introduced me to the field of industrial and safety engineering, and he constantly supported me during my early years at Pitt.

Thanks to Dr. Howard Kuhn for his insightful advice and suggestions, especially during my periods of confusion. I want to thank Dr. Sungkyu Jung for his outstanding support and guidance during my experiences at the Department of Statistics and his introduction to the fascinating field of statistical shape analysis.

I also thank many faculty members at Pitt: Drs. Natasha Vidic, Bo Zeng, Paul Leu, Lisa Maillart, Ravi Shankar, Hoda Bidkhori Satish Iyengar, Kehui Chen, and Zhao Ren, from whom I have learned things that will be useful throughout my personal and professional life.

I am indebted to friends I made here at Pitt: Yuwen Yang, Shan Gong, Junfeng Gao, Chaosheng Dong, Yanfei Chen, Ke Ren, Xueyue Shi, Yubo Xiong Wei Wang, Liang Xu, Ruichen Sun, Kai He, and so many others, for making this journey a unique and fulfilling one.

My special thanks go to my parents and parents-in-law for their endless support, infinite patience, great understanding, and constant encouragement throughout my life.

Finally and foremost, this thesis is dedicated to my beautiful wife, Qing Zhao, who gives me unconditional love and support. Her happiness and smile are the most beautiful things that I could ask for, and I am so grateful to travel through life with her.

1.0 Introduction

1.1 Background

Reverse engineering (RE) and additive manufacturing (AM) play significant roles in manufacturing industries. RE can transform a physical object from the physical or biological spheres to the digital sphere. At the same time, AM can directly translate this digital model to a physical or biological product. This combination is critical in the advancement of Industrial 4.0, whose duty is to blur the lines among these spheres [191]. However, the lower quality of models generated by RE or AM constrains the broader adoption of both by the industry. One major bottleneck is the lack of suitable analytical methodologies to fit their unique process characteristics.

The major research objective of this dissertation is to develop a novel analytical framework to bridge this gap. This framework aims to analyze the geometric accuracy and precision for these models, physical or digital, created by RE or AM. More importantly, it can link other advanced analytical methodologies and advanced manufacturing techniques for process analysis and parameter optimization to improve their geometric quality characteristics.

1.1.1 Reverse Engineering

RE plays an important role in shortening the throughput time in the manufacturing cycle. In manufacturing-related applications, RE is defined as a set of systematic processes that extracts design information from an existing physical product [55]. Specifically, geometric design information of mechanical parts is of great importance for redesign and reengineering purposes and for providing re-manufacturing with a much easier solution [13]. The legacy parts in turbine manufacturing [112] and aerospace industries [52] need to be reverse-engineered for repair or reproduction. In biomedicine, tissue, such as bone [37] or tooth [25], can be easily scanned by RE and reproduced by AM for various applications [58], such as education [155] or operative planning [142]. It is also more accessible for designers to start from a clay model in a mechanical design project [13]. After the design is tested or optimized, the clay model is transformed into a computer-aided design (CAD) file through RE for manufacturing process design and planning. RE needs can be categorized as follows [55]:

- Design of new product: In most cases, design, especially for products designed from model testing (streamlined design, turbine blade design, injection mold design, etc.) or products with aesthetic lines or design, often starts from a physical prototype without CAD information.
- Modification of existing products: Designs are often iteratively modified to get higher functionality or performances. However, after modification, CAD models for the product will not be available and need to be reverse engineered to store digital design data.
- Loss of product design data: In some instances, existing parts need to be re-manufactured; however, the CAD model is no longer available, or the data file is corrupt.
- Verify the product: The RE system can extract the dimensional information of the part. The comparison between the RE model and the design can determine the part's deviation for inspection purposes.

Figure 1 illustrates the main steps in a traditional manufacturing process and a RE-embedded one. Traditional manufacturing processes, or forward manufacturing processes, start from a design stage and then progress to the manufacturing of physical products. RE, on the other hand, initiates from a physical object, not an original design. It then scans and translates this object into a digital model for re-manufacturing this existing part. A critical assumption under RE is that the physical part contains the major product specifications, such as material, manufacturing process signature, geometric information, etc. The geometric information is of the most interest and importance since it determines the tool selection, production plan, and parameter design of the re-manufacturing processes. Digitization, the first step of RE, translates the physical object from the physical world to the digital world by surveying the surface points. The raw data format of the collected points is three-dimensional (3D) point clouds. However, the CAD model is the *de facto* language utilized in the context of a manufacturing system for communication and documentation. Therefore, RE can be

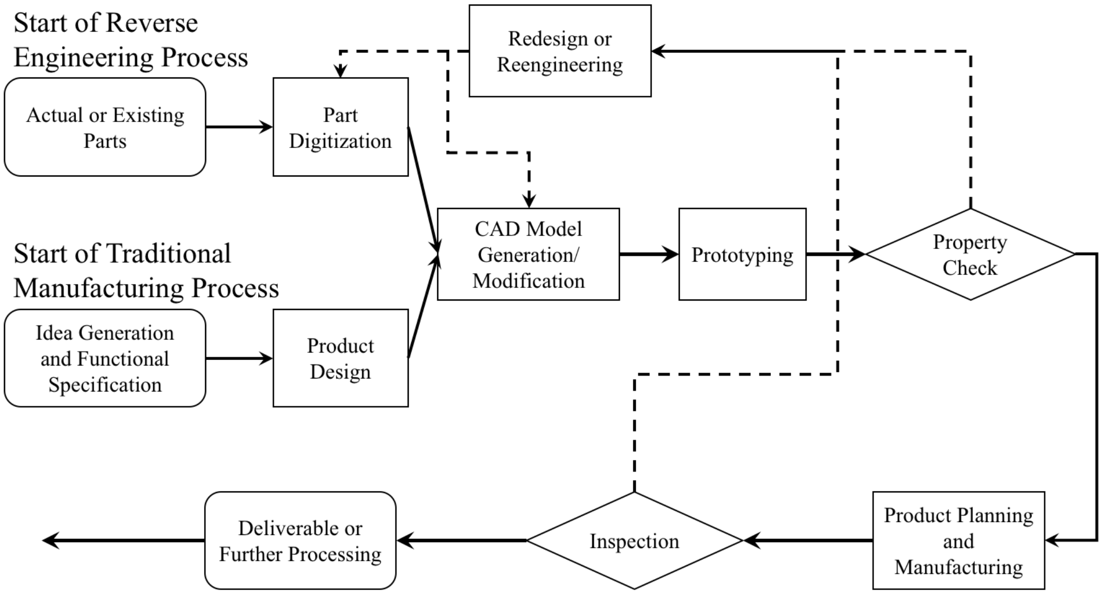

Figure 1: Traditional vs. RE manufacturing processes.

broadly separated into two sequential steps: (1) to transform the object from the physical sphere to the digital sphere and (2) to interface with other manufacturing processes, as shown in Figure 2.

RE starts with geometric information collection or digitization processes to transform the object from the physical world to the digital world. Traditionally, the name "digitization" comes from taking discrete points from 3D surfaces with specific machines, e.g., coordinate measuring machine, laser beam, etc. However, with the emergence of new technologies, such as stereo vision, machine vision techniques, and computed tomography, the digitization process can be summarized as acquiring dimensional data from undefined surfaces, synonymous with scanning. Recent research has focused on developing strategies, such as path planning and sampling, to improve the precision of the scanning techniques, which are crucial for the quality of the 3D model.

After digitizing the part, an essential process is to convert the point cloud to a geometric form. This form should be compatible with the CAD platforms to interface with other manufacturing processes. Without this conversion, data are just a sea of coordinates with little

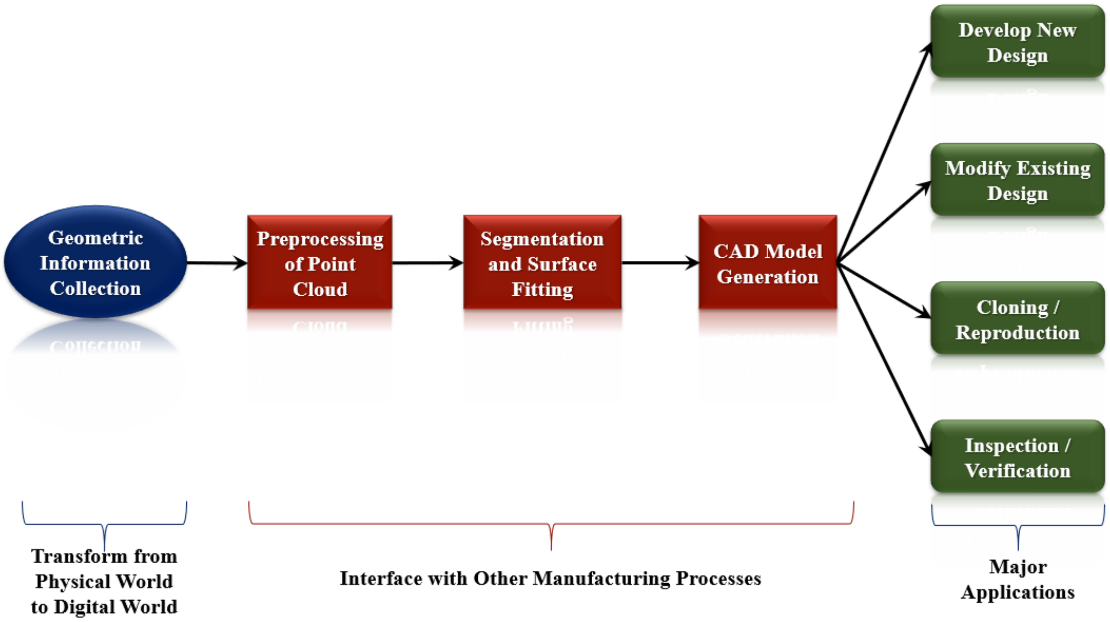

Figure 2: Conventional RE steps.

meaning. The data collected by digitization have random noises, which needs preprocessing step to transform it into a usable format and exclude the outliers. Then, different surface representations are available to describe the outside surface of the target. There are three forms of representations: algebraic, parametric, and nonparametric. With each type of surface representation, external surfaces can be fitted from data clouds; based on these surfaces, a surface-based CAD model is available for subsequent processes. We combine these separate processes as a way to interface with other manufacturing techniques. However, an automated procedure of this integrated process with high precision remains a future challenge; although the human eye and brain can easily identify the surfaces, they are not sensitive to a set of sensors and an intelligent set of algorithms.

Even though the steps in Figure 2 seem sequential, the RE processes in practice are cyclic, and several iterations may be required to achieve the final CAD model with high accuracy and precision.

1.1.2 Additive Manufacturing

AM, also known as 3D printing or rapid prototyping, is a set of manufacturing techniques sharing a common basis by adding materials bottom-up. In 2012, the AM industry standard, ASTM F2792 [78], determined to use additive manufacturing as the official term for all technologies based on this layer-upon-layer manufacturing process. In this dissertation, we follow the standard and adopt AM to describe this entire set of technologies. After first introduced by Charles (Chuck) Hull in the 1980s [75], AM processes quickly gained popularity in the defense, automobile, and aviation sectors to create part prototypes for design improvement and validation. With the recent advancement of accuracy and expansion of printable materials, AM could also make finished products for much broader industrial applications. The revenue of AM products and services worldwide exceeded \$7.3 billion in 2017 and more than doubled in 2020, with a surge to \$35.6 billion by 2024 [176].

AM is an attractive manufacturing technology because of its design flexibility, ease of access, and high customizability. Adding material layer-by-layer, AM can produce parts with flexible geometric designs and intricate structures directly from the CAD design models. Some issues in traditional manufacturing processes, such as complex process planning, time-consuming design decomposition, and assembly, may become insignificant in AM processes. Thus, AM is widely used in high value-added industries, including turbine manufacturing [12, 174], aerospace [106, 166], and biomedicine [110, 80], whose designs are either highly customized or extremely complicated.

The input of AM processes is usually CAD models. The most common model is the STL (short for STereoLithography, Standard Triangle Language, or Standard Tessellation Language). An STL file can be directly translated from other 3D CAD models drawn by the designers or 3D point clouds generated by the RE process as an output. CAD models may not exist in many applications, such as biomedicine or re-manufacturing of legacy parts. Moreover, due to the high geometrical complexity in these applications, creating a CAD model may take too much time for manual design—or not even be accessible. The capability of manual design is also limited by the capacity of CAD packages and the accessibility of the visualization, which makes the designs suboptimal. Therefore, RE is an essential companion of AM and plays a vital role in many AM applications.

The next step that includes material, process selection, and simulation is iterative or parallel. The researchers and AM practitioners usually list critical properties that the final products must satisfy beforehand, such as mechanical properties, bio-compatibility, and biodegradability. These properties, which dominate the material selection and structural design, are verified by mechanical or biomechanical simulation. On the other hand, the materials selected and the mechanical properties also determine the manufacturability for specific AM processes. Even though the layer-by-layer printing of AM appears to be conceptually straightforward and various printing options and techniques are now available, each of them has different properties and material limitations due to their specific mechanism.

1.2 Research Motivation

This section presents the generic problems we identified in the current-state-of-the-art development of RE and AM. The requirements for potential solutions to these problems are analyzed and presented for methodology development in later chapters. We first clarify the distinction between two RE-related definitions as well as their importance in practice. This distinction raises important questions regarding the RE models' accuracy, precision, and tolerance design in a re-manufacturing system. Then, the unique features of AM are analyzed in detail, which demands a unique set of AM-oriented metrology and analytical tools.

1.2.1 The RE Process and RE Systems

RE is a broad definition and has various meanings in different contexts. In this dissertation, we will first differentiate between two practical definitions based on the RE: RE process (REP) and RE system (RES). REP is the one that most researchers and practitioners adopt; its objective is to accurately reconstruct the CAD model of one unique object [55]. Therefore, REP takes one physical object as input and outputs a part-specific CAD file. Next, REP can be integrated with other processes, such as redesign, re-manufacturing,

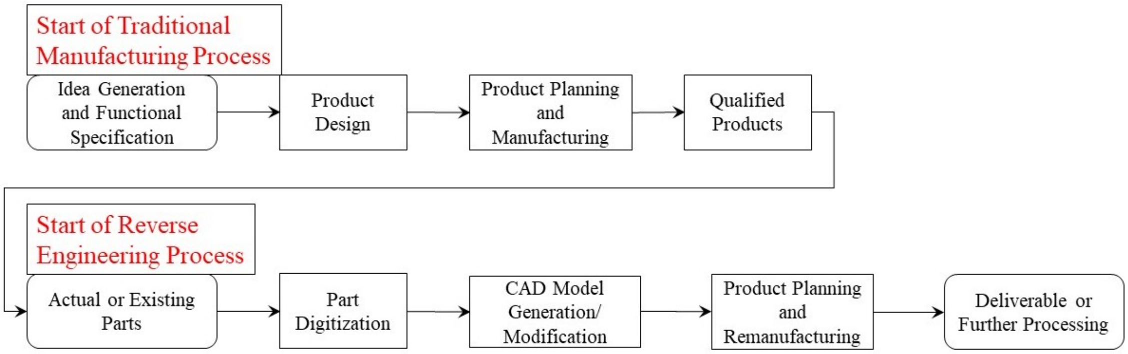

Figure 3: Complete manufacturing/re-manufacturing process map.

and inspection. On the other side, RES is a manufacturing system that combines REP and production systems for re-manufacturing purposes. Thus, RES takes physical parts as input, but its outputs are the reproduced parts that should be qualified by the initial design.

Conventionally, researchers and practitioners treat REP as an independent information extraction process. The 3D CAD model from one scan of a single part is often the practice of any RE applications. This idea is reasonable for RE practices when only a unique part or applications, such as inspection, exist. With high precision scanners and flexible surface fitting algorithms, the model generated can be close to the scanned physical part. However, two significant questions emerge when considering RES from a systematic view. The first is the complete manufacturing sequence, including the initial design and production process, which is shown in Figure 3. Instead of being an independent process, REP in this system is a manufacturing process that bridges the physical parts—the output of the initial production system, and the CAD model—the input of the subsequent re-manufacturing process. Accordingly, REP's variability would partially cause the final reproduced products to deviate from the initial design. Even in some applications, such as biomedicine, where no initial design is available, deviations from the physical parts, other than the ones from the re-manufacturing process, exist due to REP. This type of variability is usually overlooked and may cause concerns in tolerance analysis of multistage manufacturing processes.

The second major issue is the re-manufacturing of mechanical parts, where an original design exists but is unknown. In a manufacturing setting, qualified products should have dimensions within the designed tolerance regions, while high-quality products are qualified products whose dimensions are as close to the original design as possible [114]. Since the objective of RES is to re-manufacture the parts for industrial applications, the recreated products must be usable and with as high a quality as possible. However, usual RE applications tend to lack both the original design and the tolerance information. Current RE practice relies on scanning a single part [100]. However, this part is just one realization or one sample from the initial production process. The reconstructed CAD model only represents the geometric information of the specific scanned object. Therefore, the model generated by one scan of a single part always deviates from the initial design. The following re-manufacturing process can further add variability to this CAD model, and the reproduced products are easily out of tolerance. Yet, due to the missing tolerancing information, the practitioners cannot determine whether the recreated parts are qualified. Although it is possible to make a tolerance redesign or tolerance stack-up analysis, both tasks are complicated and time-consuming. Also, these approaches may call for a high precision re-manufacturing process to produce qualified parts without an appropriate tolerance design.

In summary, our first research motivation lies in the different functionalities of RE. First, RE is a manufacturing process that possesses variability. The process analysis and planning of RES should consider tolerancing for REP. Second, RE is an information extraction technology. If an original design of the parts of interest exists, RE's final objective is to reconstruct this design.

1.2.2 Dimensional Tolerance Issues

As shown above, RE is the first step of computer-aided manufacturing (CAM) and engineering (CAE) and an important design task. In addition, RE is also treated as an input to AM since the input for AM is CAD files and STL files, both of which are RE's output. Moving a physical part to a 3D printed part helps set up the process between RE and AM and is a trend for future manufacturing and service industries. For example, in the healthcare industry, customized products, such as organs, stem cells, and tissues, can be reverse-engineered through bioprinting techniques [185]. However, tolerance design, without which the geometric design may diminish the product's usefulness and functionality, must be carefully observed throughout the whole process. The consensus is that the manufacturing of the parts whose dimension is the same as the design is impossible; thus, manufacturing two products that are the same is not achievable.

The entire process, including design, manufacturing, RE, and AM, is shown in Figure 4. For example, a product whose size is A mm was designed for some specific purpose that requires high precision with tolerance 2δ mm; therefore, the required output product should be within $A \pm \delta$ mm. After design and production, a manufacturing error is added to the initial design $A \pm \delta_M$ mm. An RE process is required to gain the design information when the original design is unknown. After scanning, data processing, and generating a CAD file, an RE error is added to the model, which results in the measure of $A \pm \delta_M \pm \delta_{RE}$ mm. The CAD file is then used for AM. After reproduction, an error of AM, δ_{AM}, is also added to the final product, whose measure is $A \pm \delta_M \pm \delta_{RE} \pm \delta_{AM}$ mm. The product's final measure is easily out of the range of the design requirements $A \pm \delta$ mm, which makes the entire reproduction process and final product ineffective.

Because of the highly unpredictable error in each step of the RE manufacturing process, the superposition error often occurs and is not easy to solve. Therefore, process controlling techniques should be investigated throughout the process to guarantee that the superposition error can be managed under an appropriate tolerance level. A more robust system that includes tolerance analysis and control techniques may be required to ensure the product is deliverable, reproducible, and feasible for high-quality reproduction.

1.2.3 Metrology and Analysis for AM

The nature of AM—adding material layer-by-layer—makes it distinct from traditional manufacturing processes. Traditional manufacturing processes can directly create features on the bulk material. AM, on the other hand, decomposes the 3D design into many thin layers. Then, these layers are sequentially printed along with the build orientation. In this

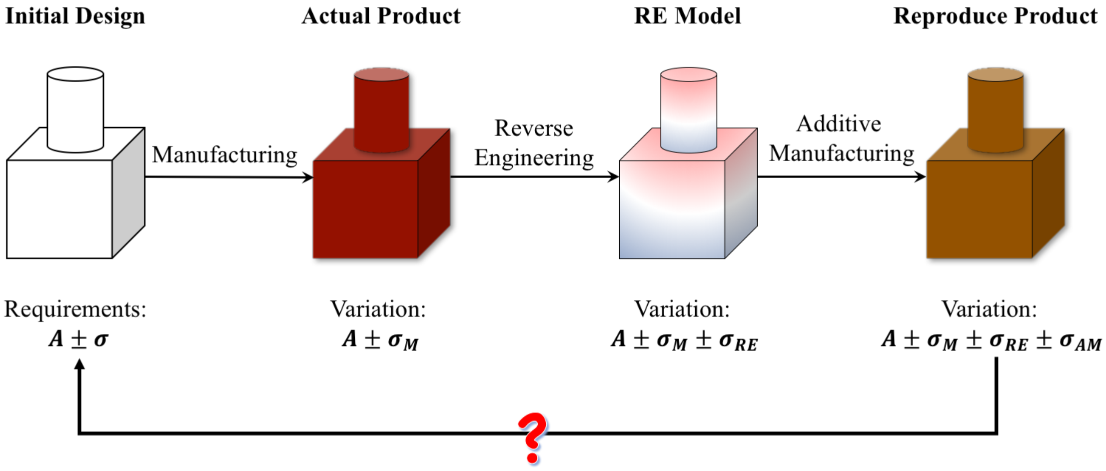

Figure 4: Process flow for product reproduction with error superposition.

way, most of the features are ”byproducts” of this process—that the part surfaces are the layers’ surrounding profiles. This property also correlated all features. Two types of feature correlations are formed by these thin layers: (1) the outline of each thin layer can be part of several features and (2) features with a different set of layers still correlate because of the bottom-up fabrication process.

Traditional metrology techniques for manufacturing products are to measure the dimensions of the features or surfaces. In profile monitoring, the 3D surface point cloud can be used to analyze the shape of a freeform surface [189]. Thus, these metrology technologies are usually feature- or surface-independent. They are suitable for the parts manufactured by traditional manufacturing processes that could generate the features or surfaces. However, these methods may not fit AM products due to the complex correlation structure of the features. Also, the AM is known for the sophisticated shapes it can produce, which cannot be analyzed using state-of-the-art metrology and analysis tools.

For example, to produce a box-shaped product, classical machining processes can directly produce six flat outer surfaces. The surface dimensions can be fully described by measuring a few points on each of them. Manual measurement or CMM can survey these points with high accuracy and precision. However, this type of measurement strategy is not appropriate for the AM-created parts, as shown in Figure 5. In Figure 5 (a), the bottom and upper surfaces of the products can be directly printed, while others are just the "byproduct" of the surrounding edges of the thin square plates. Therefore, measurements of the side surface using the traditional CMM method only provide the dimensional information of, at most, a few layers. Furthermore, in Figure 5(b), if the box-shaped part is built along an arbitrary direction, CMM measurements could provide little information about the true dimensions of any features. Therefore, the classic feature definitions can be problematic in the AM-oriented metrology if we consider some unique AM process parameters, such as infill, printing orientation, layer thickness, etc.

On the other hand, conventional analytical tools, such as the design of experiments (DOE) [113] and statistical process control (SPC) [114], are usually based on the measurement with a simple data structure. The methods are either univariate- or multivariate-based, suitable for the data collected from traditional metrology tools. During the past decade, researchers have proposed a branch of methodologies based on functional data analysis for manufacturing process monitoring and improvement [40, 81, 89]. These methods treat surfaces as smooth functions and analyze them through their functional properties or dimensional reduction techniques. However, the functional data analysis is limited to smooth 3D surfaces, which are not suitable for AM with complex features and sophisticated dependency structures.

Therefore, a new set of metrological and analytical techniques oriented towards AM processes is urgently required. These techniques could analyze the point clouds collected from AM-produced parts for process analysis, optimization, and monitoring.

1.3 Classification of Manufacturing Processes

RE and AM have a unique nature when compared to traditional manufacturing processes. As shown in the previous discussion, the AM-created features may not be identified by the 3D printers. Instead, most features are "byproducts" of the thin layers. A similar idea–that

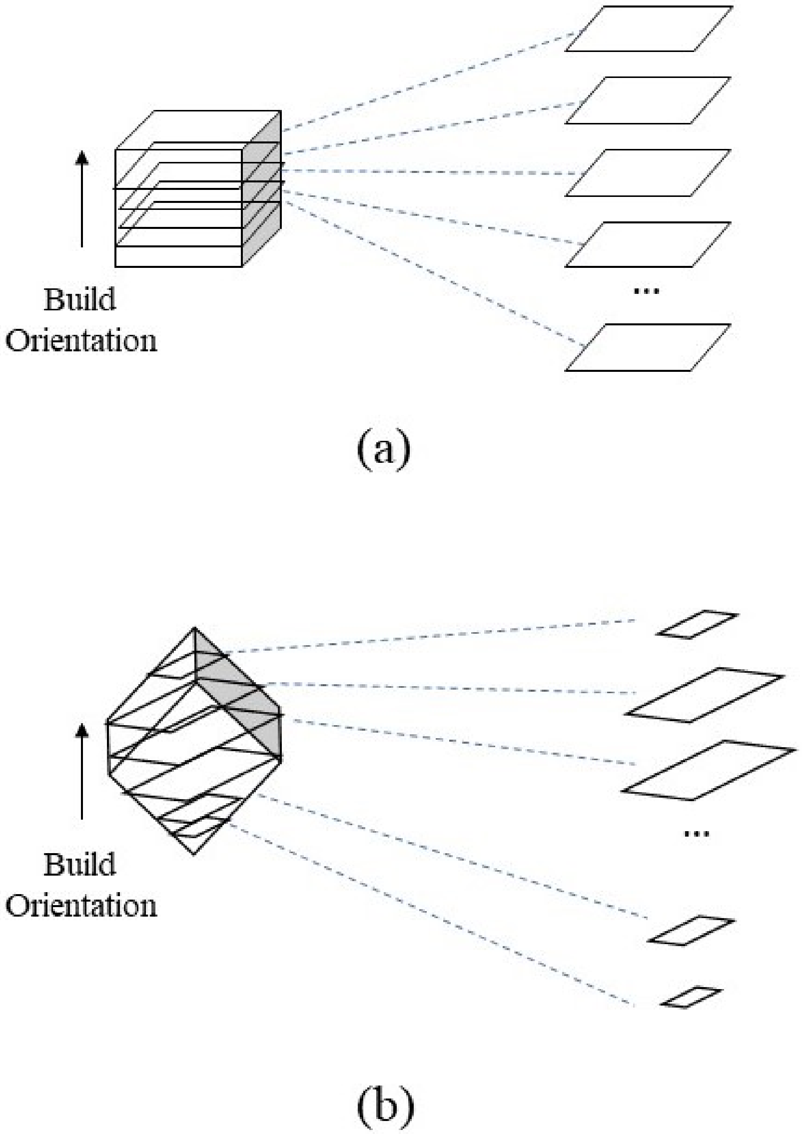

Figure 5: Major issue in dimensional metrology of simple box-shaped objects printed by different build orientations: (a) if the build orientation is parallel to the vertical edges, the side surfaces are the "byproduct" of the surrounding edges of the layers, where the classic CMM metrology only provides little dimensional information of a few layers and (b) if the build orientation is an arbitrary direction, all the outer surfaces are "byproduct," and little information about the true dimensions of any feature can be directly measured by the CMM.

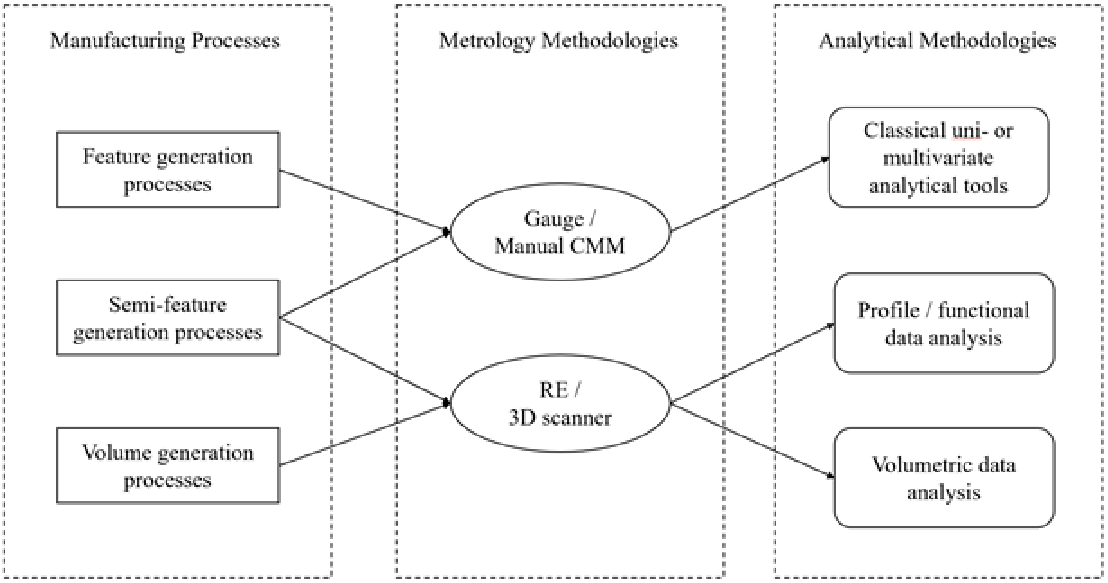

Figure 6: Three classes of manufacturing processes and their corresponding metrological and analytical tools.

the scanners do not actively differentiate the features—applies to RE. Therefore, we propose a novel way to classify manufacturing processes based on their corresponding metrological and analytical methodologies: direct feature generation processes, semi-feature generation processes, and volume generation processes (Figure 6).

Feature generation processes cover most of the current extensive machining processes. These machining processes can directly generate the product features. For example, the drilling process can generate hole features, while the surface milling process can generate flat surfaces. In this category, traditional point-based metrology tools, such as gauge, or manual CMM, are useful. Classical DOE methodologies, such as ANOVA, can be implemented to seek the best production settings for the processes of this category; traditional process monitoring techniques, such as $\overline{X}$ and S^2 control charts [114], or profile monitoring [1, 36], can be used to monitor and control the processes.

Volume generation processes, on the other hand, do not directly generate features. Instead, the processes create most of the features as "byproducts." All the AM and RE processes belong to this category. Based on this nature, 3D scans of the whole volume are a better choice for metrology purposes. Moreover, whole-body point cloud analytical methodologies, such as the methodologies proposed in this study, are suitable for analyzing these processes.

The semi-feature generation processes are in the middle of the feature and volume generation processes. The techniques generate all the features; however, the feature generations are not independent. Die-related manufacturing, such as die-casting and die-forging, are in this category. Both traditional metrology and 3D scans can be selected for different purposes. Also, a mixture of both classical methodologies and our proposed framework could work for this category.

1.4 Research Objectives

This study aims to develop a set of methodologies that can analyze the 3D point clouds and improve the RE and AM processes' geometric quality. Specific objectives are summarized below:

- Develop a statistical framework that provides multiple point clouds with statistical analyzability and mathematical tractability.
- Propose a set of novel methods under the above framework for more accurate RE and re-manufacturing with cost-effective solutions.
    - Provide a method to reconstruct a CAD model based on several scans of a unique part or several scans of several parts, which is close to the dimension of the specific part or original design with a low variance;
    - Propose a process planning model that provides suggestions for the RE practitioners to find the minimum number of required parts and scans to reconstruct the RE model and achieve the predetermined precision requirements;
    - Develop a technique that can estimate the initial tolerance design based on the statistical analysis of several parts with the same design and the knowledge of the original production system; and

  - Design an automated variance modeling technique to study the uncertainties of a 3D scanner.
- Develop a hypothesis testing procedure to analyze how the AM process parameter settings affect the geometric production accuracy.

1.5 Summary and Thesis Outline

This chapter discusses the background and geometric quality issues in both RE and AM processes. These problems seem to be independent of each other. However, they share some similarities and are highly related. First of all, RE can be used as a metrology tool for AM. Instead of surveying the profile data, RE can provide a complete description of the AM-produced parts. Thus, if RE could generate a detailed point cloud with high precision, the AM-produced products could be precisely described and measured. Secondly, the point cloud is the *de facto* data type for analysis to survey the accuracy and precision or make decisions regarding the RE process. Because the whole-body point cloud measured by RE includes correlation structures of all the features for AM, it is more suitable to deal with the whole-body point cloud for offline analysis and AM processes control. In summary, we plan to build a statistical framework that can be used to deal with whole-body, or closed-shape, 3D point clouds.

In this proposal, Chapter 2 provides a summary of the literature about the advancement in RE techniques as well as AM-oriented statistical tools. The first part of this chapter presents the advancement of the current state-of-the-art methodologies in both hardware and software that are applied in RE. The following part reviews AM techniques and quantitative methods that are devoted to improving AM accuracy.

Chapter 3 proposes a new statistical framework—volumetric data analysis—which focuses on high-density 3D closed-shape point clouds, to achieve the objectives presented in this chapter. General ideas and major components of this framework are discussed. The concept of volumetric data analysis and related research are first summarized at an abstract level for methodology development. Then, this chapter presents specific techniques for each step in detail.

Chapter 4 first applies the framework to generate the mean surface configuration based on the data clouds collected from several scans and multiple parts, if any. A Bayesian model with prior knowledge of production processes and scanners is built to model the uncertainty and make the inference of this configuration. The marginal posterior of the mean surface configuration outperforms the single scan model with lower variance, concentrating around the physical object or the initial design. Furthermore, a bi-objective optimization model is proposed to answer the RE process-planning questions, such as how many scans and parts are required to achieve specific precision requirements.

A systematic geometric inspection and tolerance estimation methodology for the RE system is offered in Chapter 5. We develop a set of tools to extract various geometric dimensional values from the point clouds or the mean scan models of several scans for each type of tolerances. Moreover, based on the domain knowledge in production process design and planning, methods are developed to estimate empirical tolerances from a small batch of legacy parts.

Chapter 6 develops an automated variance modeling algorithm that utilizes a physical object's local geometric features and Bayesian extreme learning machines (BELMs). Our proposed ensemble and residual BELM-variants are trained by a scanning history composed of multiple scans of other distinct objects. A new empirical Kullback-Leibler divergence selects the specific scanning history that is geometrically similar to an object of interest.

Chapter 7 introduces the framework to AM-oriented metrological and experimental analysis. A high-dimensional hypothesis testing procedure is proposed to compare the geometric production accuracy under two printing settings. New visualization tools for deviation diagnostics are presented to aid in interpreting and comparing the process outputs. The proposed methods are illustrated with a real experiment to compare the printed parts' accuracy under different layer thicknesses in a filament deposition modeling printer.

Chapter 8 outlines the main conclusions and potential future directions from the current study.

2.0 Literature Review

This chapter reviews the body of knowledge regarding this dissertation's two main themes, e.g., RE and AM. The first part of this chapter (Sections 2.1, 2.2, and 2.3) reviews the major advancement in the field of RE. It includes the literature review on digitization technologies, RE modeling methodologies, and techniques to improve RE's accuracy and precision. The second part (Sections 2.4 and 2.5) surveys the state-of-the-art AM processes and the work of AM-oriented quality improvement tools. A significant portion of the remainder of Chapter 2 appears in [55] and [58].

2.1 Digitization Techniques in RE

Current state-of-the-art RE techniques are reviewed in several papers [14, 38, 42, 55, 92, 160, 168]. In this dissertation, we focus on the RE techniques and procedures that significantly affect the model accuracy and precision.

Accurate geometric data collection, also known as digitization, is invariably the starting point and a critical step for every RE process. Digitization is a process that collects the data of surfaces of the objects and converts them to a digital form. As the first stage of reverse engineering, digitization processes have severe impacts on each subsequent step's accuracy and precision via the point clouds. Also, the digitization step requires more time when compared to the steps after it since the following steps involve a set of computer algorithms, which is usually faster. Therefore, to get the data points with high accuracy, high precision, and fast speed, digitization techniques have attracted much interest from researchers during the past few decades.

Effective digitization can be achieved by employing several different techniques. Each uses a physical mechanism to either directly or indirectly acquire the coordinates of specific part features. Figure 7 presents the taxonomy of currently available technologies. These technologies can be broadly classified into three categories based on whether physical contact appears on the target's surface or volume: contact, non-contact, and hybrid methods.

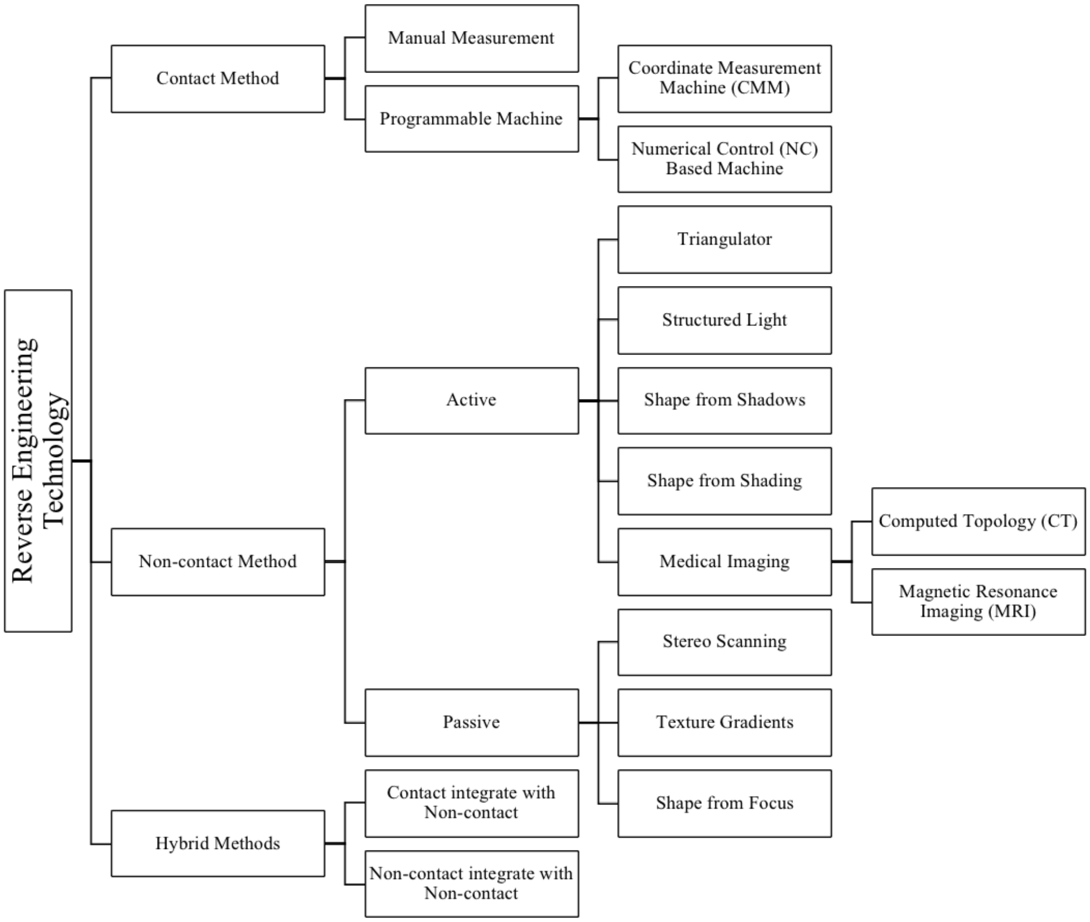

Figure 7: Taxonomy of reverse engineering techniques.

As a more traditional method when compared to non-contact methods, contact methods have been utilized for several decades. These methods require mechanical contact between the interested surfaces and a measuring device, usually using a contact probe or stylus. Contact measurements tend to obtain more accuracy, higher precision, and higher quality of surface finish but are more time-consuming.

Compared to the probe or stylus to contact the surface, non-contact methods do not have mechanical contact with the part to be studied. This class of techniques typically uses a medium, such as light, laser, sound, magnetic fields, or X-rays, as the tool for deducing surface information. There are two subgroups of the non-contact methods: active and passive techniques. Compared to the contact method, the non-contact methods require less time for the scanning process; however, these methods cannot measure hollow structures or small features on the surface of transparent materials.

2.1.1 Contact Methods: Manual Measurement

The contact methods can be traced back to manual measurement ages that occurred around half-a-century ago. Several critical dimensions across the parts are identified by experienced workers and then can be used for blueprint drawings. The instruments include calipers, measuring gages, angle finders, etc. With the development of computer-aided design systems, key points from the measurement of a surface can be entered into a CAD system, wherein curves and surfaces that interpolate these points can be generated, followed by the generation of a 3D CAD model. The manual measurement process is flexible since the workers can determine the key points by experience. However, the disadvantages are significant: the poor accuracy and precision of measurement because of subjectivity, the limitation of the form of surface or object, and the tremendous level of person-hours required. This manual method is rarely used today for a reverse engineering process but might help generate constraints in surface fitting steps.

2.1.2 Contact Methods: Coordinate Measuring Machine

Introduced as a machine for part dimensional inspection in the early 1960s, CMM is the first and still one of the most popular RE digitizers. This device uses contact stylus to measure spatial points on a workpiece's surface and then translate it into a three-dimensional Cartesian coordinate system. The contact stylus is generally a highly sensitive pressure sensing device triggered by any contact with the part surfaces. Three issues of a CMM that determine its measuring performance (i.e., accuracy, flexibility, measurable workpiece dimension, the throughput of measuring process, and costs) are types of configuration, control types, and fixture designs (Figure 8).

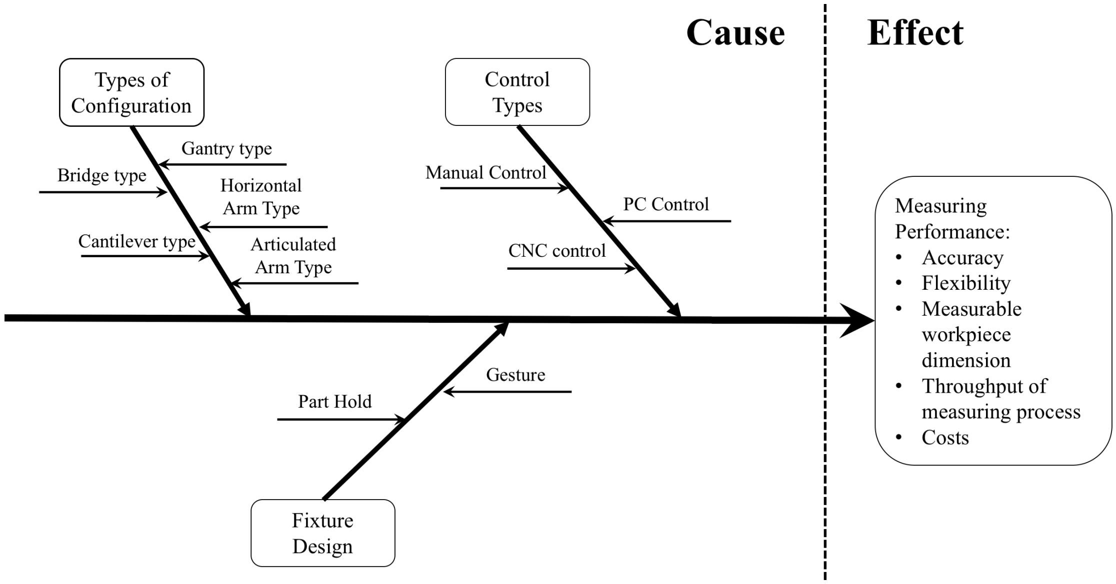

Figure 8: Fishbone diagram of casual factors of CMM measuring performance.

CMM machines have been well researched in efforts to improve their performance. Some researchers develop CMM planning algorithms to avoid the collision of CMM probes [4, 103]. ElKott and Veldhuis [46] and Yu et al. [186] propose adaptive sampling methods to scan freeform surfaces using CMM. However, most of the inspection methods are CAD-correlated. A trend of CAD-free, automation inspection path planning of CMM has emerged; this path planning first appeared in the area of freeform surface inspection. Chiang and Chen [30] propose a surface skinning method, incorporating an iterative procedure for the reverse engineering of sculptured surfaces. Li et al. [99] and Li and Nomula [98] generate methods of both CAD-guided and non-CAD-guided to increase the accuracy of CMM in measuring external profiles of porous objects.

2.1.3 Contact Methods: Numeric Control-Based Machine

Because the price of CMM is prohibitive, researchers and practitioners intended to find a substitution that could be modified into scanning equipment. The numerical control (NC) based machine was introduced in the 1940s and 1950s; its intention was to mount existing tools on a programmable motor for automated manufacturing. Using an NC-based machine mounted with the stylus is a practical solution since NC-based machines are widely used in industries that are easily programmed. Furthermore, an NC-based machine is easily changed with current-state-of-the-art scanning techniques [28, 148], and up-to-date path planning algorithms [111].

2.1.4 Non-Contact Active Methods: Triangulation

Triangulation is a well-established active technology for accurate geometric data acquisition based on the principle of triangulating a measurement point on the part from a well-designed system, including a source and a detector. Both single light triangulators and laser strips share the same underlying principles. Figure 9 shows a typical system configuration. Points P_L and P_C are the exit pinpoints of the laser source and the camera's entrance pupils. S' is the point reflected from point S of the object. Also, the angle between the points and the rotary table axes is known as α. Therefore, we have

$$z_s = \frac{d\,l}{B'S' + l\tan(\theta)} \tag{2-1}$$

and

$$x_s = z_s \tan(\theta), \tag{2-2}$$

where z_s and x_s are x- and z-coordinates of the point S in 3D coordinate system, d is the distance between P_L and P_C, θ is the angle between the laser beam and predefined z axis, and l is the distance between pupil and camera [16].

The scanning process starts from either the bottom layer of the part and proceeds upwards to each layer or from a vertical line layer before proceeding either right or left to each layer with user-defined intervals. Therefore, when the scanning process is complete, the data are a collection of the points' locations organized with equal interval cross-sectional layers, which can be used for further processing. Generally, laser-scanning technologies can produce accurate data repeatable to less than 0.001-inch [37]. Also, the laser scanner is the most common method used in reverse engineering applications because, relative to other methods, it is fast and robust [51, 105].

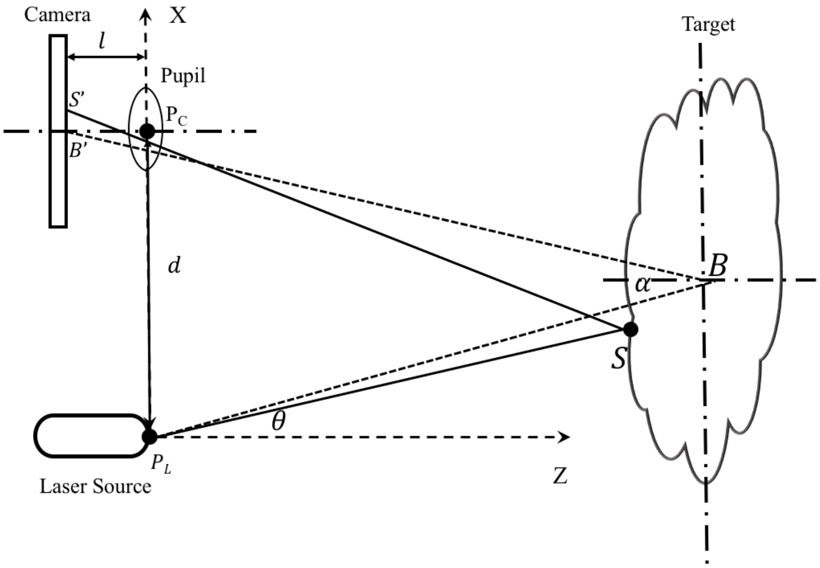

Figure 9: Representation of the triangulation principle.

2.1.5 Non-Contact Active Methods: Structured Light

Systems based on structured light share the same active approach as mentioned in triangulators. Instead of a single beam or strip of light, structured light involves projecting light patterns onto a surface; the surface's geometric information can be generated by analyzing the resulting patterns projected on the video camera. The projection of different patterns in terms of accuracy and throughput time has been extensively studied. Le Moigne and Waxman [94, 95] use multi-resolution grid pattern light projected on the objects for robot vision. Morita et al. [116] proposed a pattern made from an M-array, which is a two-dimensional (2D) extension of an M-sequence, to correct pattern disorders. Maruyama and Abe [108] present a method for acquiring range data by projecting multiple slits with random cuts. Also, some researchers [154, 158] have explored the projection of fringe patterns, which are particularly suitable to maximize the resolution of measurement with a faster speed.

2.1.6 Non-Contact Active Methods: Shape-from-Shadows

The shape-from-shadows method is a variant of the structured light approach. Instead of obtaining geometric information through analyzing the reflection of patterned light projected onto unknown parts, the 3D model can be rebuilt by capturing and analyzing the shadow of a predefined object projected onto the target with moving light [47, 187]. Despite its low cost and simple equipment benefits, this method is rarely used in the RE field because of its low accuracy and precision.

2.1.7 Non-Contact Active Methods: Shape-from-Shading

Similar to the shape-from-shadows technique, the shape-from-shading approach also uses the shadow phenomena to obtain geometric information. However, the shape-from-shading requires directly projecting light onto the object of interest, which will generate shading onto the background. The shading on the target surface will change according to the varying position of the light source. A thorough review of algorithms able to extract the shape information from this type of method can be found in the reference [69]. Nevertheless, this approach has shortcomings in the accuracy obtained, especially for a small scale of target and in the presence of external factors that influence the reflectance of surfaces [175].

2.1.8 Non-Contact Active Methods: Medical Imaging

Magnetic resonance imaging (MRI) and computed tomography (CT) are utilized to acquire geometric information for biomedical purposes. MRI is a versatile, powerful, and sensitive tool that incorporates the principles of nuclear magnetic resonance. This process utilizes the absorption and emission of energy by atomic nuclei in a surrounding magnetic field to generate thin-section images of any part of the body, like organs, bones, and ligaments, from any angle and direction. The quality of the image under MRI is closely related to the strength of the magnetic field. However, due to the magnetic field setting, measuring any metallic object is potentially inapplicable.

On the other hand, a CT scanner is another tool for viewing the human body's internal structure that can scan metallic subjects [104]. Its fundamental principle is to send a thin X-ray beam at the target from multiple angles measuring the varying amounts of X-ray beams after attenuating by different densities from the opposite side. Both the MRI and CT can now acquire high accuracy and can solve difficulties when measuring the target's holes or internal structures; however, the cost of these imaging techniques can be prohibitive.

2.1.9 Non-Contact Passive Methods: Stereo Scanning

Stereo scanning is the process of acquiring geometric data of an object by concurrently integrating the photographs captured by two or more cameras from different perspectives. With the same principle of triangulation, stereo scanning requires no additional equipment, e.g., specific light sources, except for cameras, which give it advantages such as simplicity and low cost. However, stereo scanning often requires human participation or enormous computational efforts to identify the image pairs' common points to reconstruct the 3D model. A significant amount of research has been published in the area of stereo scanning [161]. Considerable advancements have enabled the development of new algorithms and the augmentation of existing algorithms to produce more accurate results and achieve real-time performance in obtaining these results. However, because of this method's mechanism, its data quality depends heavily on the surface texture's sharpness, which is affected by surface reflectance. Stereo scanning has significant applications in areas that do not require high precision acquisition data, like computer vision or robotics; its fast feature detection is more critical in motion planning or collision avoidance.

2.1.10 Non-Contact Passive Methods: Texture Gradients

The main idea behind surface reconstruction through texture gradients is based on two facts: (1) the further away from an object one is, the smoother its surface will appear to be and (2) the image of certain texture elements (texels) relates to the surface orientation [157]. Therefore, the distance of certain texels from a known viewpoint can be estimated by inspecting the perceived texture at that distance. This method has simple, low-cost equipment requirements. However, it has a limited performance on accuracy and precision.

2.1.11 Non-Contact Passive Methods: Shape-from-Focus

Shape-from-focus techniques utilize the focal properties of a lens to determine the depth and range information of the target [119]. A lens is employed as a range finder through the ”depth of field” phenomenon. The image is blurred when it is located to a distance proportional between the target and the in-focus object plane. This technique has evolved from a passive approach to an active scanning technique to improve its resolution and accuracy. However, this method is still inadequate for commercial reverse engineering systems due to its low accuracy and non-uniform spatial resolution.

2.1.12 Hybrid Methods

Each of the methodologies detailed earlier has both pros and cons. For example, contact digitizers, e.g., can provide accurate and reliable measurement results through CMMs. Their data acquisition processes require much time due to inefficient planning; these contact digitizers also depend upon human intervention. Non-contact digitizers, on the other hand, are capable of medium to high-speed data generation and significant time reduction, but the level of accuracy is comparatively lower than that of contact ones. Hybrid methods meet the increasing requirements of both fast scanning speed and high measurement accuracy, together with the flexibility and high level of automation of the digitization process. These methods, which incorporate two or more digitization methods to provide ”smart” path planning with a high-speed and high precision, are increasingly applied to the RE field.

2.2 Interfacing Reverse Engineering with Other Manufacturing Processes

RE systems’ real power and flexibility lie in their capability to combine other manufacturing processes to reproduce the products through CAD/CAM platforms. The digitization processes will result in a ”raw” data cloud acquired through a reverse engineering system; however, this data cloud must be ”massaged,” including preprocessing and transforming into specific forms to be used by computer platforms [13]. At the beginning of the massaging process, the raw data should be smoothed and the outliers removed. The data cloud is then typically transformed into a specific format that a CAD system can identify. The language of CAD is geometric-based.

Three primary modeling techniques are widely used: wire-frame modeling, surface modeling, and solid modeling [183]. Wire-frame, the first-developed and most basic method, is stored in a data file as a collection of points, lines, and types of curves. This method, which requires a low volume of data storage, was used for data reduction for RE systems [117]; however, wire-frame modeling techniques cannot fully satisfy the increasing demand for customizable, complex designs and freeform objects. Furthermore, because reverse-engineering includes the digitization of the target object's surfaces, surface modeling techniques, which primarily consist of a set of faces, are more versatile and flexible, with the ability to model the edges and surfaces.

Multiple options for surface modeling from data clouds exist. Polygonal meshes offer the simplest option. The main idea for polygonal meshes is to convert the discrete data clouds into piecewise smooth, continuous models through small patches. Polygonal meshes are important in computer graphics and animations because of their simplicity and flexibility, especially for freeform surfaces [7, 91]. However, small gaps between surface patches exist due to missing scanned data, especially when scanning a complex part, like cavities, where it is impossible to acquire all parts of scanned surfaces. Various hole-filling algorithms are found in archival journals [32, 39, 85, 101].

Another major option is the curve and surface fitting of the point cloud data. Chivate and Jablokow [31] provide a thorough but not up-to-date overview of surface representations and fitting mechanisms. In general, surface representations can be divided into two categories: algebraic forms and parametric forms. Algebraic forms assume that the target surface can be represented by an implicit equation $f(x, y, z) = 0$ in 3-space or by a homogeneous polynomial equation $f(x, y, z, w) = 0$ in a 4-space [17]. Under this representation, algorithms, such as least-squares fitting or least median of squares, deal with computing the equation's coefficients. However, due to the global form in the algebraic function, any modification of the data set would cause refitting of the whole surface.

Another type of surface or curve representation form is the parametric form, including Bézier's and B-spline, and non-uniform rational basis spline (NURBS) surfaces or curves. This category is called parametric form because the surfaces or curves are represented in terms of two parameters—u and v. The main differences among the above three representations lie in the basic functions. Specifically, Bézier's surface/curve utilizes Bernstein polynomials as its basis function; B-spline surface/curve uses polynomials as its basis function defined over a knot vector; NURBS surface/curve employ rational polynomials as its basis function. Fitting data cloud into these three surface representations has attracted a lot of interest [50, 77, 107, 143, 165].

With the state-of-the-art surface fitting algorithms, surface models generated from measured data can be obtained. A surface model inside CAD platforms can be rendered into a solid model; its versatility allows it to be used with finite-element analysis, fluid flow analysis, and numerical control-part programming for CAM.

2.3 Techniques for Accurate RE

The techniques that could improve RE's accuracy can be broadly divided into point cloud level and model generation level improvements. The point cloud level techniques are usually the methodologies that reduce the error and variation in the surveyed data coordinates. As the first step in RE, point clouds' accuracy profoundly affects the following steps and the final model. This type of method usually improves the accuracy from the scanners' point of view since the point clouds are their direct outputs. One primary idea is to integrate two types of scanners—a less accurate one with low resolution and an accurate one with high resolution known as hybrid digitization techniques [55]. The less accurate scanners are superior in scanning speed, which can be used for process planning, while the high accurate scanners are used to extract precise geometrical information. Current research on hybrid methods of RE primarily focuses on sensor selection, scanning path planning, and coordinate system unification. Methods are proposed by researchers, such as Bradley and Chan [18], Carbone et al. [22], Li and Wei [100], Motavalli et al. [118], and Sładek et al. [151], to integrate non-contact scanning techniques onto a CMM; the non-contact methods are used for path planning and the CMM is followed for accuracy data collection. Chan et al. [26] introduce a multi-sensor approach for rapid digitization by integrating a CCD camera for path planning and a laser scanner for accurate data collection. Li et al. [96] present a tactile-optical system where a tactile probe was used to compensate the data from a laser line scanner. Lu and Wang [105] mount the point laser probe next to CMM to scan the next path and provide path planning for the contact scanning probe.

Another method for accuracy improvement at point cloud level is scanner calibration. The principal idea is to use a highly accurate point cloud to calibrate the less accurate one. Bešić et al. [11] find the bias term between CMM and laser scanner and calibrate the point cloud through compensation of the bias. Xia et al. [182] propose a Bayesian hierarchical model to integrate two misaligned point clouds collected from two scanners with different resolutions. Later, Colosimo et al. [35] solve a similar problem using the Gaussian process model. Recently, Wang and Fugee [171] used a Bayesian generative model and high-resolution metrology data to calibrate the point cloud collected by the low-resolution scanner. In summary, the calibration problem is close to the generalized regression problem in statistical learning, where the response is the accurate point clouds with high resolution, and the predictor is the one with lower resolution and accuracy. A major assumption in this field is that the CMM can provide highly accurate measurements. In a real application, the accuracy of a CMM is measured through calipers for standard dimensions, while the variation for calipers is quantified as a univariate variable and analyzed by gauge repeatability and reproducibility (R&R) analysis [21]. Thus, the variation for such point clouds still exists, and no current available methods can analyze or make inferences for their variability.

On the other hand, the point cloud needs to be transformed into a CAD format for redesign or reproduction. The polygonal mesh model is one of the widely-used outputs, as shown in Section 2.2. However, this method suffers from two significant problems. First, if small gaps between surface patches exist due to the scanner's limitations, such as the area near sharp edges, it is impossible to generate a closed surface model for redesign and re-manufacturing. Second, since the polygons constitute the surrounding surfaces, the generated outer surfaces are not smooth. Another class of methods is to fit the point clouds to parametric surfaces if the operators could identify the types of surfaces. However, the surfaces are limited to only a few types because of the parametric functional form. Nonparametric methods are introduced to the 3D scanning field to solve this problem. Roca-Pardiñas et al. [137] use a kernel smoother to reconstruct one feature from point clouds. Del Castillo et al. [41] propose a geodesic Gaussian process to fit the freeform surface, which also filters the measurement noise and provides the inferential capability to the surface.

The parametric models are as flexible as the polygonal meshes while providing smooth surfaces. Fitting point clouds into these forms have attracted much attention. Ma and Kruth [107] propose a NURBS surface fitting scheme based on singular value decomposition (SVD). A functional neural network is proposed to fit the point cloud to B-spline surfaces [44] and, later, Bézier's surfaces [76]. The same group also suggests a particle swarm optimization algorithm to reconstruct a NURBS surface for a given point cloud [51]. Sarfraz [143] and Sarfraz and Raza [144] offer evolutionary heuristic techniques to solve the curve-fitting problem using NURBS. Still, all the surface algorithms are suitable for a single point-cloud. If there are multiple scans of the same part, the only option is to register the point clouds and perform the surface fitting for the registered point cloud. Thus, these methods cannot analyze the variational behavior among scans or parts or provide an accurate estimator other than the single scan of a single part model. However, these surface fitting algorithms provide a continuous surface fitting for the discretized point cloud, which can be used to generate landmarks in our framework construction.

2.3.1 Tolerancing in RE

Following the RE-generated model, the re-manufacturing processes are utilized to reproduce the part. Traditional manufacturing processes, such as machining, have been developed for mass production; thus, their high setup costs can be split into a large number of produced parts [15]. However, in a re-manufacturing setting, where the batch of products is usually small, the setup costs for traditional manufacturing could be prohibitive. Moreover, each of the features is created by a specific tool because of the specially designed tools. Sophisticated and time-consuming process planning may be required for re-manufacturing processes [102], which could further increase the time and cost. AM, on the other hand, is more versatile for small batch production. It could directly create the parts with complex features from the CAD model without complicated setup and process planning. Therefore, AM is a more suitable option for small batch and highly customizable parts reproduction.

Significant issues can be raised in RE- and AM-embedded re-manufacturing systems because of their primary objective, i.e., reproducing parts qualified by original equipment manufacturer (OEM) specifications. The current practice of RE only focuses on reconstructing the nominal design by scanning the physical object without assigning any tolerance to the feature and dimension. Other types of design information are also essential components of the product and manufacturing design [183]. Geometric dimensioning and tolerancing (GD&T) specification is one of the most critical pieces of information that dominates both the manufacturing process selection, planning, and part inspection [146]. Tolerance is a major OEM geometric specification that is often overlooked [55]. Even though the nominal design is of great importance, tolerance specification within CAD design is also critical for designing and planning manufacturing processes [67, 68]. Tolerances are assigned to the feature dimensions to enable them to fit into an assembly. According to engineering drawing standard [124], tolerances are required to be assigned to each of the feature dimensions in the design to avoid confusion in both the design and manufacturing departments. Moreover, qualified parts are ones whose geometric dimensions should be at least within the original GD&T specification for application purposes. However, most of the design information is either missing or inaccessible in RE embedded re-manufacturing applications.

Little research has been developed to deal with this issue. Jamshidi et al. [79] propose a method to approximate the tolerance region by collecting information about the original manufacturing processes by examining the parts' surface finish. Even though the surface signature could provide information about the manufacturing processes, the process variations are related to the process parameter settings and process planning, which are unknown and difficult to estimate. Kaisarlis et al. [87] present the idea of a knowledge-based system based on several GD&T standards with functional requirements. Later, the same group proposes a method for positional tolerance assignment [86]. It was clear to the authors estimating the GD&T specifications that there is a research gap that needs to be bridged in current RE-embedded re-manufacturing systems.

2.4 Additive Manufacturing Processes

2.4.1 Stereolithography

Stereolithography (SLA) was developed in the mid-1980s by Charles (Chuck) Hull [75]. It makes use of radiation curable resins, or photopolymers, to create solid objects by additive successive 2D layers that build on each other. The liquid materials undergo a sequence of a photopolymerization process, which is a curable chemical reaction, to become a solid object (Figure 10). Various types of radiation are available for SLA, such as gamma rays, X-rays, UV light, etc., while the materials are limited to photopolymers, which can be expensive. SLAs generate accurate physical objects with smooth surface finishes, but due to the liquid nature of photopolymers, the support structure must be carefully designed to hold the printed parts.

2.4.2 Selective Laser Sintering

Selective Laser Sintering (SLS), shown in Figure 11, is also called the powder bed fusion process and uses a CO_2 laser as the thermal source for inducing fusion between powder particles [3]. Instead of liquid resins like SLA, the thin layers of powder are spread across the build bed by a roller, which provides proper support to the printed parts. Thus, there is no need for support structures in the design. Also, this fusion process can print various materials, such as metal, plastic, ceramic, etc. However, these fused small particles can cause rough surface finishes on the printed parts. Thus, post-processing is often required for the SLS process. Also, preheating the powder bed is always helpful to improve the fusion process, which may cause the powder particles to become sticky and, further, diminish the accuracy of the SLS process when compared to SLA and other AM techniques.

2.4.3 Inkjet Printing

Inkjet printing is one of the least expensive and most simple AM techniques [150]. This process uses a printer head to create tiny ink droplets or continuous filament onto a powder

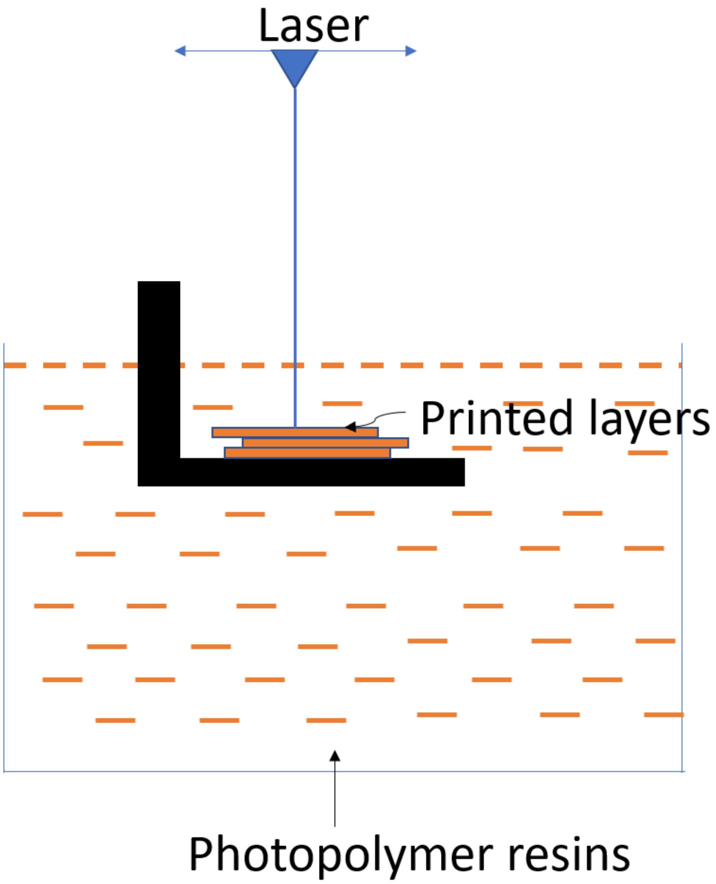

Figure 10: Mechanism of the SLA (stereolithography) processes.

bed (Figure 12). After deposition, the inks are transformed and then solidify to achieve the desired properties of the finished products. The transformation is primarily due to the surrounding natural environment and the ink properties; however, post-processing steps, such as heating, are also required. Since inkjet printing relies on a power bed like the SLS, there is no need for a designed support structure. However, the introduction of ink materials eliminates the ”fusion” process, and the process lacks accuracy.

One exciting application of inkjet printing in medicine is to print organs due to the simplicity of mechanism and flexibility. Instead of binding ink, the printer head can print living cells onto a biological scaffold to generate organs or cell cultures [121]. Furthermore, inkjet printing also provides the possibility of personalized medicine and accurate drug delivery.

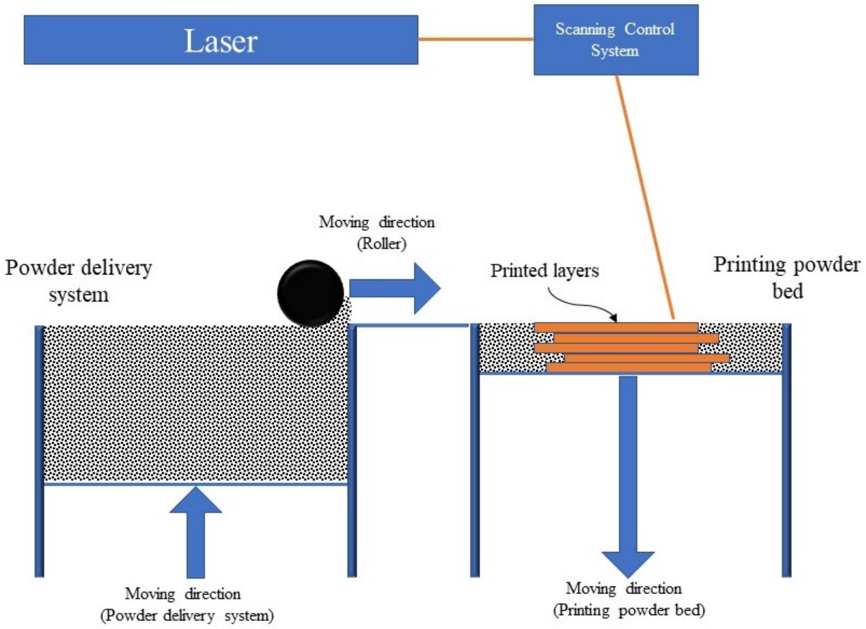

Figure 11: Mechanism of the SLS (selective laser sintering) processes.

2.4.4 Extrusion-Based System

The extrusion-based system, shown in Figure 13, forces the material from the reservoir through a heated nozzle to generate a semi-solid state material filament and to fully solidify on the target surface [61]. Materials including acrylonitrile butadiene styrene and other thermoplastics are typically used for extrusion-based systems. One example of an extrusion-based system is fused-deposition modeling (FDM). Overall, the extrusion-based system does not have fine detail and good mechanical properties of the other AM techniques and, therefore, requires post-processing for good surface finishes. Also, unlike the SLS and inkjet printing, which are powder-bed-based methodologies, an extrusion-based system requires a support structure to prevent model collapse. However, the lower price of this system has given it popularity in medical applications. Beyond printing biomaterial, an extrusion-based system can also directly print cells or multicellular systems through the high-viscosity cell-laden hydrogels for various medical purposes.

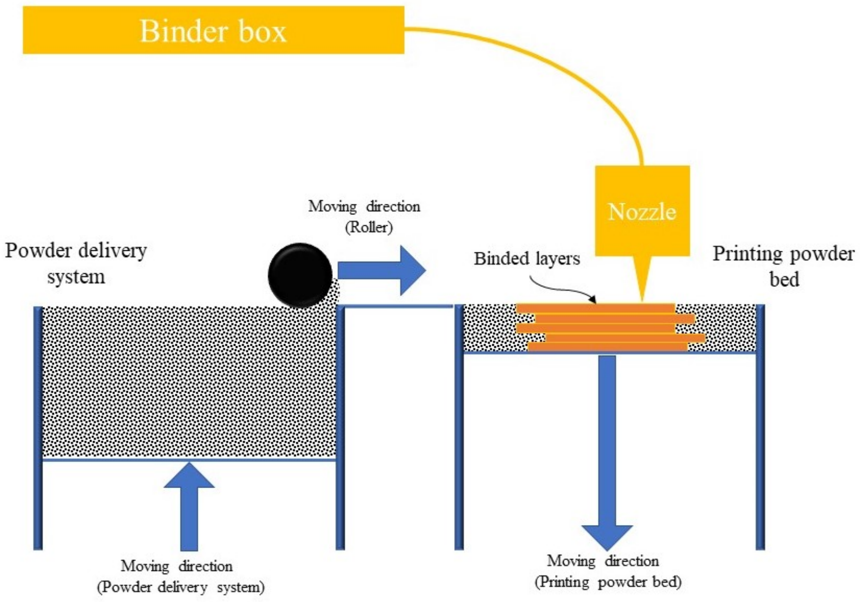

Figure 12: Mechanism of the inkjet printing processes.

2.5 AM-Oriented Accuracy Improvement Tools

The first AM technique, stereolithography, was invented in the 1980s. With decades of expansion, the AM family has expanded to several techniques with many classes of materials [61]. However, the accuracy of AM still has not achieved the industrial requirements, which prevents its broader adoption. Therefore, part of the AM community has shifted its focus from technology development to product quality improvement [33].

2.5.1 Shape-Based Statistical Techniques for Manufacturing Processes

In the literature, geometric data are often treated as profile data in the field of SPC or shape data in statistical shape analysis (SSA) [43]. Most of the studies in production analysis or quality engineering utilize profile monitoring to deal with point clouds of 2D profiles or 3D surfaces [34, 82, 129]. Profile monitoring is one subject of the multivariate statistical process control method. Its main idea is to use a parametric or nonparametric model to describe the

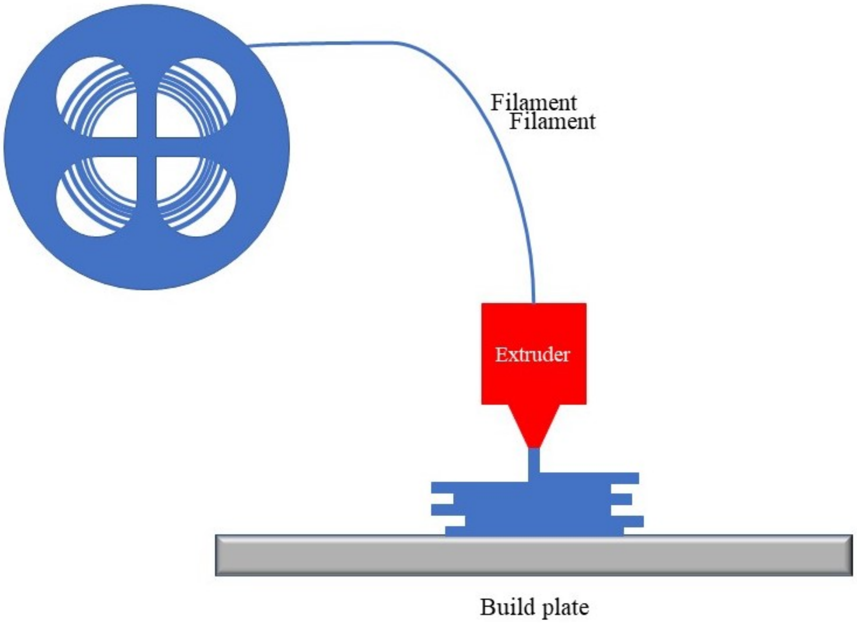

Figure 13: Mechanism of the extrusion-based printing processes.

point cloud in a functional form. The geometric data first train a model; then, multivariate SPC methods can be applied based on the monitoring of the model parameters. If both the response and covariates are coordinates or shape-related 3D data, the response can be one of the coordinates, and the others can be utilized as the covariates. Detailed reviews on profile monitoring can be found in [120, 178, 179].

Nevertheless, there are limitations to these techniques when applied to the AM-created parts. First, profile monitoring requires an assumption of a functional form between the response variable and covariates. However, in terms of AM inspection, our objective is to make the inference of or monitor the whole-body point clouds collected from the product. These point clouds are closed-shaped based on the assumption that the functional form can be invalid. Second, profile monitoring can only be applied to 2D or 3D surfaces, where the correlation between features is underestimated. Therefore, profile monitoring or functional data analysis may not be appropriate for the analysis of AM processes.

The other field of methods is based on SSA. Del Castillo and Colosimo [23] first introduce SSA-based analysis of variance technique to manufacturing applications for process improvement. Their technique is based on the shape data obtained by measuring the parts at specific landmarks or correspondence points among objects. However, there are limitations to this methodology when applied in high-precision manufacturing applications. First, the landmarks should be found and matched for each target product. In SSA, these points are either manually selected and matched or generated based on the domain knowledge. However, thousands to millions of points are surveyed from the RE process based on random sampling procedures, within which the landmarks are difficult to find. Second, the shapes' similarity is free of rotation, translation, and isometric scaling effects in SSA. For a manufacturing setting, even though rotation and translation will not influence the quality of the final products, the scaling factors and the dimensions of a feature are essential quality characteristics.

Other models, such as the Gaussian process models [34], are more flexible in dealing with surface fitting problems regarding the geometric data. However, these models, again, are used for surface data instead of point clouds. Moreover, the Gaussian process models may be infeasible to handle point cloud data collected from RE because of their prohibitive computational cost for large data sets.

2.5.2 Statistical Geometric Quality Engineering Techniques in AM

AM-oriented statistical analysis has attracted much attention during the past few years. In this research, we only focus on offline analysis and monitoring for the geometric aspects of AM. One of the most active fields in AM accuracy improvement includes CAD model compensation schemes. Tong et al. [163] and Tong et al. [162] are the pioneers in this field. However, their compensation scheme only considers the three-coordinate directions independently, which is not consistent with the manufacturing process. To solve this issue, Huang et al. [74] and Jin et al. [83] use a polar coordinate system to develop a compensation scheme for layer shrinkage, which is more consistent with the AM processes. Later, Sabbaghi et al. [139] consider the interference behavior for the compensation of the thin circular plate to further improve the compensation performance. In addition, the same group [140] built a Bayesian model to extend the compensation scheme to general shapes, such as polygons. Sabbaghi and Huang [141] proposed using transfer learning that enables deviation models to transfer across processes with limited runs. Other models, such as the Gaussian process [29], are also proposed for prediction and compensation of the in-plane shape deviations. While these methods are suitable for layer-wise compensation, they overlook the inter-layer dependency.

On the other hand, continuous production becomes a vital trend in the AM community. Process monitoring, control, and optimization are critical components for inline AM process-quality engineering. However, few studies focusing on this area have been developed. Recently, Zang and Qiu [189, 190] have offered novel Phase I/II monitoring schemes for the nonlinear profile data collected from AM. Their algorithm combines the essences of both conventional profile-monitoring methods and SSA. However, this study fails to capture the unique character of the AM process. Instead of producing profiles or features, AM directly creates the products by adding material layer by layer. Even though their methodology is close to SSA, the grids generated in their model are not landmarks. This algorithm uses equally spaced points, which cannot guarantee the same number of corresponding points for all surfaces.

2.6 Summary

This chapter provides a review of the RE and AM techniques. It also highlights the major advancements in the current state-of-the-art techniques for geometric quality improvement and monitoring. However, a significant research gap exists in applying the currently available methodologies to RE and AM because of their unique processing characteristics. Therefore, there is an urgent need to develop a framework capable of bridging the gap between the whole body of point clouds and advanced analytical toolsets. In the next chapter, a novel volumetric data analysis framework is developed to model and analyze these 3D point clouds collected from RE or AM.

3.0 Volumetric Data Analysis: The Framework

In this chapter, a novel volumetric data analysis (VDA) framework is proposed to model the uncertainties of the 3D point clouds. The general flow of the VDA framework is shown in Figure 14. The VDA framework is based on a similar foundation as the classic SSA framework, whose key idea is briefly reviewed in this chapter. The core differences between the two frameworks are presented in Section 3.1. Next, the technical details of the VDA framework are discussed. Section 3.2 develops the landmark generation algorithms, which automatically transform multiple unstructured point clouds into landmark configurations. These landmarks possess two main properties: corresponding relationship and high volume. Section 3.3 presents the registration step in the framework. The registration algorithms play two important roles in the VDA framework: (1) they align the point clouds by removing the translational and rotational factors and (2) they transform the landmarks from the configuration space to the size-and-shape space. Section 3.4 provides the proven statistical properties of the landmarks in this space and builds the data models for the registered configurations. Lastly, Section 3.5 discusses the considerations regarding the density of the generated landmarks. A significant portion of the remainder of Chapter 3 appears in [57] and [60].

3.1 Statistical Shape Analysis

Many statistical modeling and inferential techniques are applied in RE and AM, such as regression analysis and classic analysis of variance for a univariate or multivariate response. For example, NURBS are widely utilized to model smooth surfaces from point clouds [192]. These regression methods are flexible in that they can fit a wide range of smooth or piecewise smooth surfaces. However, regression-based methods usually focus on a single surface or feature but overlook the relationship among features. The parts' functionality in a manufacturing setting is determined by both the feature design and, more importantly, their

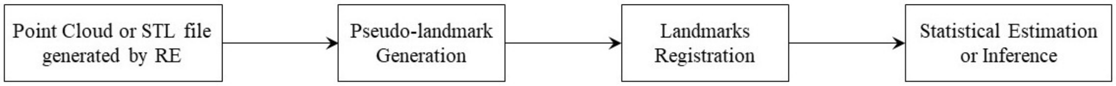

Figure 14: Flow chart of general volumetric data analysis framework.

spatial relationships. Also, as the features are "byproducts" of the AM processes, regression methods can provide little information about the fabrication process, as presented in 1.3. Variations are unavoidable in AM-created parts because of the uncertainties in the fabrication processes. Thus, multiple AM-created parts should be considered to understand process variations and make statistical inferences. Classic methodologies, such as functional analysis, could be utilized to analyze or monitor the variations in the parameters in the regression models of parametric forms. However, the nonparametric models, such as B-spline or NURBS, can be involved in such an analysis.

SSA, on the other hand, is more suitable for the analysis of point-cloud-based data. The landmarks that are the points of correspondence among objects are utilized as the geometric descriptor to bridge the gap between shape space and the multivariate statistical methodologies [43]. With multivariate analysis, the uncertainties of both the individual points and their correlation are analyzed simultaneously, without any parametric assumptions on the shape's form. The general SSA methodologies assume the landmarks are either given or extracted from the shape by the experts. The landmarks utilized in SSA are usually manually selected by domain knowledge. Therefore, the number of landmarks is often at a small level. With the advancement of high-resolution cameras and scanning technologies, the number of surveyed points increases exponentially. However, only a few selected or inferential points are utilized as the landmarks for analysis due to the different research interests. Therefore, the configurations' dimensions, the matrices whose rows are the 2D or 3D coordinates of the landmarks, are usually small.

Then, the sample configurations are registered and transformed into the shape space by removing the size, translational, and rotational factors. In SSA, the widely used method is

Table 1: Comparisons of the interested problems between the SSA and the VDA frameworks.

Framework	Number of landmarks	Major focus
VDA	Large ($> 10^4$)	High-dimensional 3D size-and-shape space
SSA	Small to medium ($10 - 10^2$)	2D shape space

the general Procrustes analysis (GPA) [43]. Even though other popular registration methods are available, such as iterative closest points, GPA offers the theoretical foundation for the following statistical analysis by providing analytically tractable distributions of the registered configurations in the shape space. When the size is essential in the analysis, GPA can be modified only to remove the translational and rotational factors, which becomes the partial Procrustes analysis. The configurations are then transformed into the size-and-shape space. However, this space is underdeveloped, especially the 3D size-and-shape space, when compared to the high-dimensional spherical shape space. Statistical inferential techniques, such as hypothesis testing and regression analysis, can be applied to the registered configurations within the shape space.

When compared to the SSA framework, the VDA shares similar steps (Figure 14). However, the size of the part is also an important quality characteristic. Therefore, instead of dealing with the shape space, the primary focus of the VDA is to make statistical inferences in the 3D size-and-shape space. Furthermore, because of the flexible shape designs and the complicated fabrication process of the AM, a large number of landmarks can provide a more detailed geometric description of the AM-created parts. As a result, the dimension of the 3D size-and-shape space is much higher when compared to that of the classic SSA problems. The comparison between the two frameworks is summarized in Table 1.

3.2 Landmark Generation

Both SSA and VDA frameworks rely on the definition of landmarks. Landmarks are defined as the points on each object with correspondence between and within populations [43]. For example, in applications, landmarks often possess domain-specific meanings, which are known as scientific landmarks. Another way to select landmarks relies on mathematical or geometrical properties, such as high curvature points or extreme points. This type of landmark is called mathematical landmarks; it is widely used in computer vision or image recognition. Pseudo-landmarks are usually the points that locate between scientific or mathematical landmarks. While these landmarks may not possess any interpretable meanings, they do provide more geometrical details of the objects. Configuration, or configuration matrix, is the matrix whose rows are the 3D coordinates of these landmarks. Thus, each configuration provides a complete description of the size and shape of the object of interest. Since the main objective of SSA is to analyze how the shape changes or to identify different shapes, the number of rows for the configuration matrix is generally small—usually tens, or, at most, thousands. Del Castillo and Colosimo [23] first introduced SSA to the manufacturing community. They proposed SSA-based tests to analyze a lathe-turning process. However, their analysis cannot be easily generalized to other manufacturing processes. The machined parts they selected have circular profiles. Due to the invariant property, all circles are similar, allowing for the landmarks to be generated by uniform angle sampling. This landmark generation strategy is not suitable for designs other than a cylinder or ball. Another strategy is to take equal distance points on a surface proposed by Zang and Qiu [189]. Although the surface types do not limit this method, the one-on-one correspondence restriction cannot be ensured.

In summary, three problems emerge if we utilize the landmark generation techniques in SSA as the solution to the geometric quality issues in an advanced manufacturing setting. First, the points on the point cloud are almost randomly distributed on the surface. Even though a CMM machine could plan an equal distance scanning grid, the points still lack correspondence between scans or parts because of random starting points or part position. Second, the mathematical landmarks are not suitable since 3D scanners are of low fidelity when scanning the vertices or edges [168]. Because of the scanning mechanism, the points near the vertices or edges, especially the sharp ones, cannot be digitized as accurately as the points on a smooth surface. Choosing meaningful geometric landmarks, such as vertices or pseudo-landmarks along the edges, may deteriorate the following analysis. Third, the deviations among manufactured parts are generally minor and sometimes located in random areas within each feature. Therefore, the analysis that relies on a small number of landmarks can be unreliable and insensitive to local deviation—and cannot meet the high accuracy requirements in an industrial setting. Therefore, many in-feature or in-surface pseudo-landmarks are required for RE and AM applications to provide a detailed description of the objects. However, it can be time-consuming to select a massive number of landmarks, and the current landmark generation algorithms are usually suitable for mathematical landmarks. In this section, we propose two classes of automatic pseudo-landmark generation algorithms. Both can start from either point cloud files or STL files. Since the landmark types do not affect the following analysis, we do not differentiate the landmarks from the pseudo-landmarks.

A general landmark generation algorithm should satisfy two major requirements:

- The generated points should be of correspondence among different scans, and
- The generated points should locate on the surface defined by the original point clouds.

3.2.1 Feature-wise Characteristic Plane Projection Algorithm

The first type of landmark generation algorithm is the feature-wise characteristic plane projection (F-CPP). The basic logic behind the proposed algorithm is to generate landmarks with a hierarchical correspondence structure. Among the well-segmented point clouds, each point cloud is separated into several subsets, called features [126]. It is easy to see that these features are one-on-one correspondence across all scans. Therefore, the landmark-generation problem can be simplified to generate landmarks for each feature. Without loss of generality, the features are assumed to be any surfaces—flat, curved, or, in general, freeform surfaces.

The primary idea is to generate a grid of points on a unique plane to the feature, named characteristic plane (CP), and then find the coordinates of the corresponding grid points on the surface. Figure 15 presents the procedures of the F-CPP algorithm. The first and

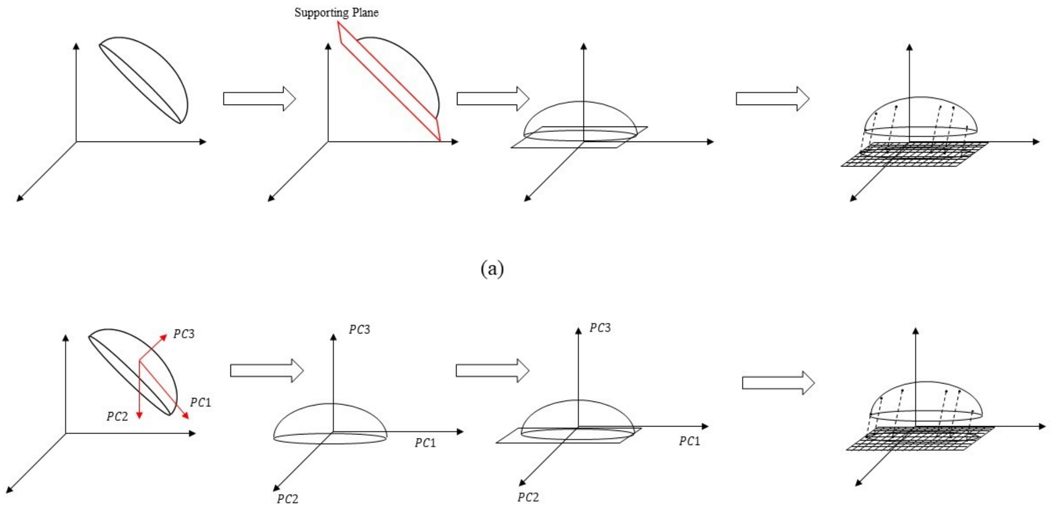

(a)

(b)

Figure 15: Feature-wise characteristic plane projection algorithms: (a) supporting plane projection and (b) principal component plane projection.

most crucial step is to find the CP for the feature. CP has two types: supporting plane and principal component plane. In the supporting plane, all the feature points are above, while the sum distance to the plain is minimized. This plane should be unique to the feature because of the minimization problem. However, the orientation of this plain can be sensitive to the boundary points. This issue could potentially cause correspondence distortion. The principal component (PC) plane, on the other hand, is more robust to the noise. Let A be a $k \times 3$ matrix containing all x-, y-, and z-coordinates of k measured points on the feature. First, the matrix Γ with columns of the eigenvectors of $A^T A$ is calculated. These three eigenvectors represent the most, second, and least variation directions of the point clouds [169]. Since the noise within the point clouds is much smaller than the design variation, these three directions should be almost identical among different scans. Thus, if the point clouds are surveyed uniformly on the surface, these three eigenvectors are unique characteristics of the target feature and robust to the noises. If the point densities are not uniform on the surface, subsampling algorithms with equal distance can provide a more robust solution. One particular case is that the feature is symmetric about the feature axis. These symmetric features may cause the eigenvectors to differ in direction among the point clouds. In this case, a part posture can be predetermined to guide the PC directions. This coordinate system does not need to be precise, but the axis directions should be similar among point clouds.

Then, a rectangular envelope that covers all projections of the corresponding feature point clouds can be found on the CP plane. For calculation simplicity, the whole point cloud is rotated towards the CP plane. The sides of the rectangular envelope are parallel to the x- or y-axis. The side lengths are the range of x and y values for the projection points. Next, a well-defined grid is generated within this rectangular envelope. Finally, the surface points of the corresponding grid points can be predicted using surface fitting techniques. Theoretically, any surface-fitting algorithms can be selected as long as they provide a continuous feature surface. In this dissertation, we adopt the Nadaraya-Watson local constant kernel (NWLCK) smoother, since it is superior in terms of computational efficiency [134]. The NWLCK smoother for z-coordinate, z_i, of grid points (x_i, y_i), $i = 1, \dots, k$, where k is the number of grid points, is

$$\hat{z}_i = \frac{\sum\limits_{\{j:(A_{1j},A_{2j})\in\Omega(x_i,y_i)\}} A_{3j} K\left((A_{1j}-x_i)/h, (A_{2j}-y_i)/h\right)}{\sum\limits_{\{j:(A_{1j},A_{2j})\in\Omega(x_i,y_i)\}} K\left((A_{1j}-x_i)/h, (A_{2j}-y_i)/h\right)}. \tag{3-1}$$

where $h > 0$ is the predetermined bandwidth, $\Omega(x_i, y_i)$ is the circular neighborhood of location (x_i, y_i) whose radius is h, and K is a 2D circular symmetric kernel function, such as flat kernel or Gaussian kernel.

After applying the F-CPP to all segmented features and stacking all the feature-wise landmarks to a matrix, the configuration that fully describes the part is created. One potential issue that could diminish the correspondence structure is that the landmarks may locate in the blank area on the projection plane. The grid points located in the empty spaces among all configurations can be safely ignored by setting the z-value to null and will not affect the correspondence. However, some grid points, especially those near the projection profile, may not have value among all point clouds. This phenomenon can block the following analysis since the configuration matrices of different scans or parts have varying dimensions. Therefore, if the rows with null z-values can be found in one configuration matrix, all the corresponding rows should be removed from the entire configuration matrices. Even though this procedure may lead to the missing of many landmarks in certain regions, it will not significantly affect the analysis for several reasons. First, these landmarks usually lie around the vertices or boundaries, where the accuracy is comparatively lower and unreliable for either CMMs and laser scanners [53]. Second, to preserve the accuracy of original point clouds, many pseudo-landmarks are generated, while the points without correspondence usually appear on the boundary of the parts. The number of these points is relatively trivial compared to the total number of landmarks.

3.2.2 Bread Slicer Algorithm (BSA)

Another way to generate pseudo-landmarks is inspired by the guided bread slicer. Instead of performing surface fitting and feature segmentation, the raw STL file can be used here. It is widely used in RE and AM and is capable of describing complex shapes. An STL file describes the surface through a set of triangles with unit normals, flexible and native to CAD packages. The STL model can accurately describe complex geometric objects, such as the bone or teeth. Since features may not be well-defined in complex shapes, F-CPP may not be suitable for generating landmarks.

Figure 16 illustrates the main idea of the bread slicer algorithm. The primary strategy is similar to the hierarchical correspondence decomposition in F-CPP. Instead of generating a 2D envelope for projection points, we find a 3D bounding box for each point cloud. Then, the cubic envelope is cut along one or all three predetermined side directions into slices. The spacing for the slices is proportional to the side length of that direction. Each slice contains a rectangle from the cubic envelope and a profile of the scan from the STL file. Next, lines that are parallel to both the length and the width of the rectangle are generated. The distance between the adjacent parallels should be proportional to the corresponding length or width. The landmarks are generated by the crosses of these parallels and the profile outline. Instead

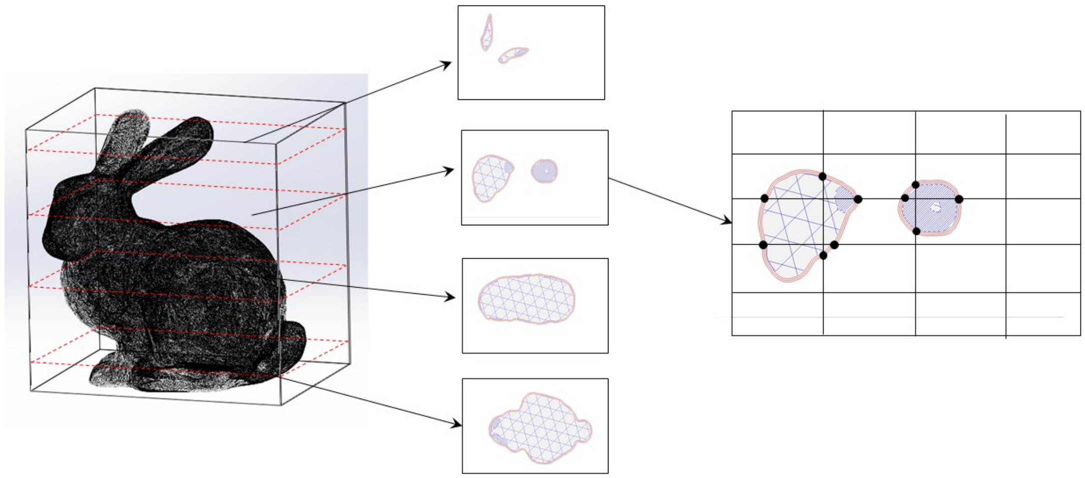

Figure 16: Bread slicer algorithm.

of the correspondence between feature grids, these pseudo-landmarks are indexed through the slice order, parallel order, and the cross order from a predefined orientation, e.g., from left to right. The pseudo-landmarks from different point clouds are of correspondence if their indices are the same.

The enclosing box should be unique to the entire point cloud, which maintains the correspondence of the landmarks. Instead of a rectangle in 2D space, one idea is a 3D cubic envelope with a minimum volume covering the whole point cloud. The 3D cubic envelope can be found by [125], which is an $O(n^3)$ algorithm. Again, this algorithm is sensitive to the randomness of the points located on the box surfaces. Another approach is to generate the box constructed by the three principal components of the point clouds. As the principal component plane, the box formed by principal components is unique to the point clouds. More importantly, this method is computationally more efficient and robust to the noise in the point clouds since the design shape dominates the variation.

Unlike the direct correspondence between corresponding grid points, the landmarks generated by BSA are corresponding through indices. The first two indices—slice order and parallel order—are guaranteed to have correspondence, while it is potentially problematic for the cross order when missing points on some scans. The "or" logic proposed in F-CPP cannot be applied to this situation since the boundaries here are surfaces in original point clouds. Removing the entire parallels from all scans, at least one of which is not consistent with the others, may make the configurations insensitive to local variations. Thus, the best way is to remove the corresponding crosses that are missing from the profiles. However, the indices only record the cross orders, which makes the removal process impossible to perform. Luckily, one facet of the crosses can simplify the analysis: the numbers of crosses generated by a parallel and the profile are always even. The profiles determine the boundary between material and empty space, and the rectangular envelope covers the whole profile. A line enters the material area from the space for general profile shapes, which causes a landmark. A second cross must then exist from the material area since the rectangular envelope is always located in the empty area. Therefore, the entering crosses and existing crosses always come in pairs. Assume the number of crosses formed by one line and the profile is $2m$. Next, the parallel can be divided into m equally spaced segments by $m - 1$ points. In this way, the pairs of crosses can be indexed by the nearest breakpoint. If one pair of crosses is missing from one scan, then the corresponding crosses with the same index should be removed from other scans. Finally, it can be ensured that the generated pseudo-landmarks among all scans are of correspondence.

3.2.3 Comparison of F-CPP and BSA

Both F-CPP and BSA can be used to automatically generate many pseudo-landmarks. The underlying ideas for both algorithms are similar. First, separate the unordered point clouds into small subsets of correspondence that are much easier to manipulate. Then, generate the landmarks at the same relative location in matching subsets. However, subset separation mechanisms are quite different. F-CPP treats every single feature as a subset, while BSA uses sliced profiles. Thus, each of these approaches has advantages and disadvantages; because of their mechanism, they are suitable for different applications.

Since F-CPP generates landmarks separately for each feature, it is superior in accuracy. For example, if the machining process produces the part, each feature is created individually. The random errors can be divided into two levels: feature-level deviation and local error. If BSA is applied to generate landmarks, the feature-level deviation, such as feature dislocation, may cause correspondence disorder or may miss many landmarks. Also, since the features are generated individually, it is more suitable for feature-wise landmark generation. However, F-CPP is not suitable for complex shapes, such as bone or teeth, where the features are not well-defined. Furthermore, F-CPP consumes a considerable amount of computational resources if complicated shapes appear.

On the other hand, BSA is a more general algorithm compared to F-CPP. The box envelope is theoretically general for any shapes, and it can process any 3D shapes without considering features. Also, BSA is more computationally efficient than F-CPP. Therefore, BSA is suitable for complex-shaped products or freeform parts.

In summary, if the product is produced by traditional manufacturing processes or has simple features, such as application of RE for re-manufacturing, F-CPP is a better choice; if the part has a complex shape structure, such as biomedical applications or AM-produced parts, BSA is the one to be selected.

3.3 Registration Algorithm

The point cloud generation algorithms help to generate a large set of well-structured landmarks. Let X be a $k \times m$ configuration matrix, where $m = 3$, containing the 3D coordinates of all k landmarks. In conventional landmark-based SSA, the shape is defined by the remaining geometric information in X when translation, size, and rotation are removed. On the other hand, the size and shape of the configuration matrix X contains complete information in X when translation and rotation are removed from X. The majority of the SSA theories and methodologies rely on the shape space. However, the accuracy of size is also an important quality factor in manufacturing processes. The definition of size and shape is more suitable for our applications. Therefore, the raw configurations need to be transformed into size-and-shape space. This process is also known as registration in other fields, such as computer vision, computational geometry.

In this section, two registration algorithms, partial Procrustes analysis and datum-guided registration, are discussed. The SSA community develops partial Procrustes analysis to map X to size-and-shape space, where statistical properties have been studied [43]. This algorithm is suitable for AM process analysis and RE process without datum constraints since the landmarks as a whole can be registered and analyzed. However, in traditional manufacturing processes, parts are produced and measured by fixing the datum features. Therefore, it is reasonable to register the configurations by aligning the datum features. In this case, we developed a modified version of the partial Procrustes analysis.

3.3.1 Partial Procrustes Registration Algorithm

A point cloud registration algorithm is usually required after the landmark generation step to remove the translational and rotational factors. Partial Procrustes analysis (PPA) is a registration algorithm that is widely used in SSA research. Let X_i be the ith configuration, the matrix whose rows are the coordinates of the landmarks, for $i = 1, \ldots, n$. The PPA can be formulated to solve the following minimization problem:

$$G_P = \inf_{\Gamma_i, \gamma_i, \mu} \sum_{i=1}^{n} ||(X_i \Gamma_i + \mathbf{1}_k \gamma_i^T) - \mu||^2 \tag{3-2}$$

where G_P is called the Procrustes distance, Γ_i is 3D rotation matrix, $\mathbf{1}_k$ is a vector of k ones, γ_i is the location parameter, for $i = 1, \ldots, n$, and μ is the sample mean configuration. PPA is a particular case of the generalized Procrustes analysis which is developed by Gower and Ten Berge [159], which includes an extra step to remove the scaling factor. The PPA algorithm proceeds as follows to solve the above least squares problem:

1. Center the configuration to remove location. The centering process can be done by multiplying each configuration matrix with a Helmert submatrix H [43],

$$X_i^P = H X_i. \tag{3-3}$$

The specific Helmert submatrix that we utilize is the $(k-1) \times k$ matrix whose jth row is $(h_j, \ldots, h_j, -jh_j, 0, \ldots, 0)$, where $h_j = -\{j(j+1)\}^{-1/2}$ is repeated j times, and the remaining entries consist of one occurrence of $-jh_j$ and $(k-j-1)$ zeros.

2. For the ith configuration matrix, let

$$\bar{X}_{(i)} = \frac{1}{n-1} \sum_{j \neq i} X_j^P \tag{3-4}$$

3. Do ordinary Procrustest registration (OPR), involving only rotation, of X_i^P's onto $\bar{X}_{(i)}$ to generate new X_i^P for all i.
4. Repeat steps 2 and 3 until G_P converge.

In the algorithm, the OPR is a simplified version of PPA that only registers one configuration, X_1, onto another one, X_2, whose locations have been removed. The objective of OPR is to solve

$$\min_{\Gamma} ||X_2 - X_1\Gamma||^2. \tag{3-5}$$

This problem is well studied by Horn et al. [70] and Goodall [63]. The minimizer is given by $\hat{\Gamma} = UV^T$, where U and V can be obtained through the following singular value decomposition problem,

$$\frac{X_2^T X_1}{||X_1||||X_2||} = V\Lambda U^T. \tag{3-6}$$

The PPA algorithm possesses many advantages. First, the PPA algorithm usually converges in a few steps. The computational speed for this algorithm is very fast. Even though the configuration dimension is high in AM applications, the registration step for the configurations usually takes only a few seconds on a regular personal computer. Second, the configurations registered by the PPA algorithm have nice statistical distribution approximations. When the variations of the landmarks are small, Goodall and Mardia [64] provide a normality approximation of the PPA-registered configurations coordinate-wise independence. This approximation will be utilized as the theoretical foundation for statistical inference in VDA.

3.3.2 Datum-Guided Registration Algorithm

In a manufacturing setting, parts are produced and inspected by fixing the defined datum features in traditional manufacturing, especially machining processes [128]. The datum features define a reference system for machining or metrology by restricting the degrees of freedom, which plays a critical role in drawing, tolerancing, and measuring. Therefore, it is reasonable to register the whole landmarks by aligning the datum for near-real practice solutions. Identifying the datum features is part-dependent and requires design and engineering knowledge, which is omitted here.

In order to register the entire set of landmarks by datum features, we first split each configuration matrix X_i into two configurations: the one containing the rows of all landmarks of the datum features, X_{id}, and the one including the remaining rows, X_{if}. Then, we apply the conventional PPA to X_{id}'s to find the rotation parameters, Γ_i's, and translation parameters, γ_i's, by solving,

$$G_{dp} = \inf_{\Gamma_i, \gamma_i, \mu} \sum_{i=1}^{n} \| \left(X_{id}\Gamma_i + \mathbf{1}_k \gamma_i^T \right) - \mu \|^2. \tag{3-7}$$

Next, the Γ_i's and γ_i's can be applied to X_{if}'s. Therefore, all the configuration matrices are registered through the datum features. A modified version of PPA—datum guided PPA (DGPPA) algorithm—is shown as follow:

1. Center the configurations to remove the location of X_{id}'s by a centering matrix C using

   $$X_{id}^P = C X_{id} = H^T H X_{id},$$

   where H is a Helmert submatrix.
2. Remove translations for X_{if}'s,

   $$X_{if}^P = X_{if} - \left(X_{id} - X_{id}^P \right) = X_{if} - (I - C) X_{id}.$$

3. For the i th datum configuration matrix, let

   $$\overline{X}_{(id)} = \frac{1}{n-1} \sum_{j \neq i} X_{jd}^P.$$

4. Perform OPR, involving only rotation, of X_{id}^P's onto $\overline{X}_{(id)}$ to generate new X_{id}^P for all i. Record the minimizers, $\hat{\Gamma}_i$'s,

$$X_{id}^P \leftarrow \hat{\Gamma}_i X_{id}^P, \quad i = 1, \ldots, n.$$

5. Apply $\hat{\Gamma}_i$ to the corresponding X_{if}^P to generate new X_{if}^P for all i,

$$X_{if}^P \leftarrow \hat{\Gamma}_i X_{if}^P, \quad i = 1, \ldots, n.$$

6. Repeat steps 2 to 5 until G_{dp} converge.
7. Stack X_{id}^P and X_{if}^P to get the registered configuration matrix X_i^P.

If DGPPA is implemented to register all configurations from a sample, the mean scan configuration can be calculated by

$$\overline{X} = \frac{1}{n}\sum_{i=1}^{n} X_i^P. \tag{3-8}$$

3.4 Distribution of the Configurations

The distribution is required to understand and investigate the configurations' statistical properties for making inferences in the later chapters. The distribution, together with its inference, of the configurations, which are matrices, can be generally complex, such as tensor-based statistical models [184, 188]. In shape analysis, for high-dimensional size-and-shape space, if the landmark-wise variance is small, each row of the configuration approximates an independent multivariate normal random variable [43]. Thus, the coordinates, or the three columns of the configurations, can be seen as independently distributed. Assume X_i's, $i = 1, \ldots, n$, are configurations from the same population. Let $X_i(x)$, $X_i(y)$, and $X_i(z)$ represent the columns of the ith configuration after registration, corresponding to x-, y-, and z-coordinates, and let $\mathcal{X} = \{X_1, X_1, \ldots, X_n\}$ be the set containing all the surveyed point clouds. Therefore, the basic models of the configurations for each of the coordinate are as follows:

$$X_i(x) \sim \mathrm{MN}\left(\mu_x, \Sigma_x\right), \tag{3-9a}$$

$$X_i(y) \sim \mathrm{MN}\left(\mu_y, \Sigma_y\right), \tag{3-9b}$$

$$X_i(z) \sim \mathrm{MN}\left(\mu_z, \Sigma_z\right), \tag{3-9c}$$

where MN represents the multivariate normal distribution, μ_x, μ_y, and μ_z are column vectors of length k and Σ_x, Σ_y, and Σ_z are $k \times k$ covariance matrices for each of the x-, y, and z-coordinates.

3.5 The Density of Landmarks

One hyperparameter that is worth mentioning in the VDA framework is the number of generated landmarks—the density of landmarks. In Section 3.2, the landmarks are generated by a grid in F-CPP or slices in BSA, whose width is proportional to the sides. The density of the grid points also determines the precision and resolution of the generated digital model. Denser grid design usually provides a high precision mean model with more details. In our study, we recommend that the grid width be close to the resolutions of the scanner or re-manufacturing process, e.g., AM. A sequential point selection method, such as model-based design [66], can be utilized to add details to the configurations by minimizing the predictive uncertainty.

4.0 Process Planning in Reverse Engineering

In this chapter, we utilize the VDA framework proposed in Chapter 3 to develop a Bayesian model for the configurations in the size-and-shape space and make decisions for the planning of RE processes. The proposed estimator based on the several scans of multiple parts (SSMP) outperforms the one created by the one scan of a single part (OSSP) procedure. Next, this estimator is utilized to answer critical RE process-planning questions, such as how many scans and parts are required to achieve predetermined precision requirements. The remainder of this chapter is organized as follows. In Section 4.1, a Bayesian model incorporating production and scanning knowledge is built to model the statistical properties of the configurations. Next, we propose the process-planning problem as a bi-objective minimization problem with precision requirement constraints in Section 4.2. Section 4.3 presents simulation studies and two industrial cases to verify the proposed framework and to illustrate the practical implementations. This chapter concludes with a summary of the presented application. The remainder of this chapter can be found in [60].

4.1 Bayesian Model and Estimation for Original Design

The configurations' distribution is required to understand and investigate the statistical properties of the mean-scan and the mean-part models for original design estimation. We assume that several parts based on the same design are available, and the distribution of the mean-part configuration is derived as the general model. For unique objects, the production-related components can be removed from this general model to get the mean-scan model. One critical fact is that the numbers of available parts and scans are usually constrained due to budget limitations or time constraints. The sample sizes for either the multiple-scan or the multiple-part projects are small in practice. Therefore, the knowledge of the production systems and the scanner's specifications is incorporated into a Bayesian model for the more accurate inference of the distributions based on small sample sizes.

Let $X_{ij}(x)$, $X_{ij}(y)$, and $X_{ij}(z)$ represent the columns of the configurations for the jth scan of the ith part after registration, $i = 1, \ldots, m$, $j = 1, \ldots, n$, corresponding to x-, y-, and z-coordinates, and let $\mathcal{X} = \{X_{11}, X_{12}, \ldots, X_{mn}\}$ be the set containing all the surveyed point clouds. Based on the distribution of the registered configuration presented in Chapter 3, the likelihood models of the configurations for each of the coordinate are as follows:

$$X_{ij}(x) \mid \mu_x, \Sigma_x \sim \mathrm{MN}\left(\mu_x, \Sigma_x\right), \tag{4-1a}$$

$$X_{ij}(y) \mid \mu_y, \Sigma_y \sim \mathrm{MN}\left(\mu_y, \Sigma_y\right), \tag{4-1b}$$

$$X_{ij}(z) \mid \mu_z, \Sigma_z \sim \mathrm{MN}\left(\mu_z, \Sigma_z\right), \tag{4-1c}$$

where μ_x, μ_y, and μ_z are column vectors of length k, and Σ_x, Σ_y, and Σ_z are $k \times k$ covariance matrices for each of the x-, y-, and z-coordinates. The prior distributions of these parameters are designed in a "weakly" informative fashion:

$$p(\mu_x, \Sigma_x) \propto |\Sigma_x|^{-k-2} \exp\left(-\frac{1}{2}\mathrm{tr}\left(\frac{t_p^2 + t_s^2}{3}\Sigma_x^{-1}\right)\right) \tag{4-2a}$$

$$p(\mu_y, \Sigma_y) \propto |\Sigma_y|^{-k-2} \exp\left(-\frac{1}{2}\mathrm{tr}\left(\frac{t_p^2 + t_s^2}{3}\Sigma_y^{-1}\right)\right) \tag{4-2b}$$

$$p(\mu_z, \Sigma_z) \propto |\Sigma_z|^{-k-2} \exp\left(-\frac{1}{2}\mathrm{tr}\left(\frac{t_p^2 + t_s^2}{3}\Sigma_z^{-1}\right)\right) \tag{4-2c}$$

where $\mathrm{tr}(\cdot)$ represents the trace of matrices, and t_s and t_p represent the standard deviations of the scanner and original production processes, if any, surveyed or derived from domain knowledge, such as past experiences, pre-experimental trials, or equipment manuals. For example, the repeatability or maximum deviation are usually reported in the manuals of the CMM or the laser scanner, which is approximately three times the corresponding standard deviations. Jamshidi et al. [79] establish a relationship between the geometric hints in the physical machined parts, such as surface textures, and their corresponding machining processes for tolerance estimation. In Chapter 5, we propose a framework to extract geometric dimensioning information from the multiple point clouds, together with the process-control knowledge, to estimate the original tolerance design. Combined with this field knowledge, or prior knowledge in the Bayesian modeling, the estimated distributions of the coordinates are more suitable for limited samples, e.g., available parts or a small number of scans. Therefore, the corresponding posterior distributions can be written as follows:

$$p(\mu_x, \Sigma_x \mid \mathcal{X}(x)) \propto |\Sigma_x|^{-k-2-mn/2} \exp\left\{-\frac{1}{2} \operatorname{tr}\left[\Sigma_x^{-1}\left(\frac{t_p^2+t_s^2}{3} I_k + S_{0x}\right)\right]\right\}, \tag{4-3a}$$

$$p(\mu_y, \Sigma_y \mid \mathcal{X}(y)) \propto |\Sigma_y|^{-k-2-mn/2} \exp\left\{-\frac{1}{2} \operatorname{tr}\left[\Sigma_y^{-1}\left(\frac{t_p^2+t_s^2}{3} I_k + S_{0y}\right)\right]\right\}, \tag{4-3b}$$

$$p(\mu_z, \Sigma_z \mid \mathcal{X}(z)) \propto |\Sigma_z|^{-k-2-mn/2} \exp\left\{-\frac{1}{2} \operatorname{tr}\left[\Sigma_z^{-1}\left(\frac{t_p^2+t_s^2}{3} I_k + S_{0z}\right)\right]\right\}, \tag{4-3c}$$

where I_k is the $k \times k$ identity matrix, and S_{0x}, S_{0y}, and S_{0z} are the sums of squares matrices with respect to the means of the corresponding coordinates,

$$S_{0x} = \sum_{i=1}^{m}\sum_{j=1}^{n} (X_{ij}(x) - \mu_x)(X_{ij}(x) - \mu_x)^T, \tag{4-4a}$$

$$S_{0y} = \sum_{i=1}^{m}\sum_{j=1}^{n} (X_{ij}(y) - \mu_y)(X_{ij}(y) - \mu_y)^T, \tag{4-4b}$$

$$S_{0z} = \sum_{i=1}^{m}\sum_{j=1}^{n} (X_{ij}(z) - \mu_z)(X_{ij}(z) - \mu_z)^T. \tag{4-4c}$$

To evaluate the precision of these estimators, we are more interested in the marginal distribution of the mean configuration μ, whose columns are μ_x, μ_y, and μ_z, respectively. The corresponding posterior marginal distributions for the mean vectors can be derived and written as follows:

$$\mu_x \mid \mathcal{X}(x) \sim t_{mn+3}\left(\overline{X}(x), \frac{(t_p^2+t_s^2)/3 \cdot I_k + S_{xx}}{mn(mn+3)}\right), \tag{4-5a}$$

$$\mu_y \mid \mathcal{X}(y) \sim t_{mn+3}\left(\overline{X}(y), \frac{(t_p^2+t_s^2)/3 \cdot I_k + S_{yy}}{mn(mn+3)}\right), \tag{4-5b}$$

$$\mu_z \mid \mathcal{X}(z) \sim t_{mn+3}\left(\overline{X}(z), \frac{(t_p^2+t_s^2)/3 \cdot I_k + S_{zz}}{mn(mn+3)}\right), \tag{4-5c}$$

where t_{mn+3} is the multivariate t distribution with $mn + 3$ degrees of freedom, and S_{xx}, S_{yy} and S_{zz} are the sums of squares matrices with respect to the sample means of the corresponding coordinates,

$$S_{xx} = \sum_{i=1}^{m}\sum_{j=1}^{n} \left(X_{ij}(x) - \overline{X}(x)\right)\left(X_{ij}(x) - \overline{X}(x)\right)^T, \tag{4-6a}$$

$$S_{yy} = \sum_{i=1}^{m}\sum_{j=1}^{n} \left(X_{ij}(y) - \overline{X}(y)\right)\left(X_{ij}(y) - \overline{X}(y)\right)^T, \tag{4-6b}$$

$$S_{zz} = \sum_{i=1}^{m}\sum_{j=1}^{n} \left(X_{ij}(z) - \overline{X}(z)\right)\left(X_{ij}(z) - \overline{X}(z)\right)^T, \tag{4-6c}$$

and $\overline{X}$ is the mean configuration from the above PPA or DGPPA algorithms.

So far, the Bayesian models for the SSMP procedure, where several parts are available ($m > 2$), have been built, and the posterior marginal distribution of the general mean part configuration has been derived. As for the unique part cases, which only require several scans, the results can be easily derived by setting $m = 1$ and $t_p = 0$ in the Equation 4-5.

4.2 Process Planning for Effective RE

4.2.1 Process-Planning Model

It has been shown in Equation 4-5 that the posterior mean part configuration has a lower variance as the numbers of parts and scans increase. A further question can be raised: How many scans n and parts m are required to achieve certain precision requirements? In a RE project, the major resources consumed by the practitioners, other than the cost of the scanning hardware or software, are the costs related to either purchase or find the available legacy parts and the time spent on the scanning project. In other words, the two objectives we consider in the context of implementing a general RE project is the minimization of both the number of parts and the number of scans for each part:

$$\min_{m} \quad m \tag{4-7a}$$

$$\min_{n} \quad n \tag{4-7b}$$

where m is the number of required parts, and n is the number of scans for each part.

The above objectives are subject to several groups of constraints, which result from the practical requirements on the precision of the models:

1. The precision requirements for the mean scan configuration have limits on the number of scans. According to the marginal posterior distributions in Equation 4-3, increasing the number of scans could lower the variance of the mean configuration. The number of scans for each of the objects can be limited by an upper scanning precision requirement, δ, which is designed or predetermined by the project requirements or application standards. Therefore, the mean scan configuration precision constraint should be included in the model:

   $$\max_{i \in \{1,\ldots,k\}} \left(q \left[\left(\Lambda_{x,i}^{n,1} + \Lambda_{y,i}^{n,1} + \Lambda_{z,i}^{n,1} \right) \right]^{1/2} \right) \leq \delta, \tag{4-8}$$

   where $\Lambda_{x,i}^{n,1}$, $\Lambda_{y,i}^{n,1}$, and $\Lambda_{z,i}^{n,1}$ are (i,i)th elements of the covariance matrices of the three coordinates, $\Lambda_{x}^{n,m}$, $\Lambda_{y}^{n,m}$, and $\Lambda_{z}^{n,m}$ are calculated in Equation 4-5 by setting $m = 1$, and q is the coefficient that is corresponding to the credible band width of the point-wise posterior marginal distribution of the mean configuration. Based on our experience, q value selected between the interval $[2, 3]$ is recommended.
2. After observing m parts, each of which has n scans, the precision requirements for the mean part configuration have a limit on the total number of scans, mn. Similar to the above constraint, the total number of scans for m objects can be limited by an upper-precision requirement of the final RE model, ϵ, which is also designed or predetermined by the application of the RE model. Therefore, the precision constraints of the mean-part configuration should be included in the following model:

   $$\max_{i \in \{1,\ldots,k\}} \left(q \cdot \left[\left(\Lambda_{x,i}^{n,m} + \Lambda_{y,i}^{n,m} + \Lambda_{z,i}^{n,m} \right) \right]^{1/2} \right) \leq \epsilon. \tag{4-9}$$

One point worth mentioning is that the value of δ should be much smaller than the value of ϵ so that $\delta << \epsilon$. The reason is a two-folded one. First, there are two sources of variations in the mean part configuration, while only one of them exists in the mean scan one. We will come back to this one later—that the sum of squares in the covariance matrices of the posterior marginal distribution can be decomposed into two components. The other reason stems from a practical perspective. When the scanner is selected for an RE project or metrology purposes, the scanner should have much higher precision than the production processes. Otherwise, the metrological conclusion made by this scanner is not valid.

3. The values of the numbers of scans and parts should be integers in practice,

$$m, n \in \mathbb{Z}^{+}. \tag{4-10}$$

Notice that the model constraints are both nonconvex and approximately biquadratic to m and n. Combined with integer requirements, this model seems to be hard to solve at first glance. Therefore, before solving this minimization problem, some practical issues need to be considered, which could simplify this model.

The first thing that needs to be noticed is that, since the process plans are designed after the practitioners collect a few scans of some parts, the posterior marginal distributions of the optimal n and m are unknown in advance. In practice, one part is selected to be scanned multiple times at first. Assume s scans of the first part are already collected and that their corresponding sum of squares, S^s_{xx}, S^s_{yy}, and S^S_{zz}, can be calculated according to Eqaution 4-6 by setting $m = 1$. As for the variances of n scans, they can be approximated by

$$\Lambda^{n,1}_x \approx \Lambda^{s\to n}_x = \frac{(t^2_s)/3 \cdot I_k + n/s \cdot S^s_{xx}}{n(n+3)}, \tag{4-11a}$$

$$\Lambda^{n,1}_y \approx \Lambda^{s\to n}_y = \frac{(t^2_s)/3 \cdot I_k + n/s \cdot S^s_{yy}}{n(n+3)}, \tag{4-11b}$$

$$\Lambda^{n,1}_z \approx \Lambda^{s\to n}_z = \frac{(t^2_s)/3 \cdot I_k + n/s \cdot S^s_{zz}}{n(n+3)}. \tag{4-11c}$$

On the other hand, to approximate the variances of m parts after collecting p parts ($p \leq m$), we need to first decompose the total sums of squares in Equation 4-6 as

$$\begin{aligned}
S_{xx} &= n \cdot SP_x + SS_x && \text{(4-12a)}\\
&= n \cdot \sum_{i=1}^{m} \left(\overline{X}_i(x) - \overline{X}(x)\right)\left(\overline{X}_i(x) - \overline{X}(x)\right)^T \\
&\quad + \sum_{i=1}^{n}\sum_{j=1}^{m} \left(X_{ij}(x) - \overline{X}_i(x)\right)\left(X_{ij}(x) - \overline{X}_i(x)\right)^T, && \text{(4-12b)}\\
S_{yy} &= n \cdot SP_y + SS_y && \text{(4-12c)}\\
&= n \cdot \sum_{i=1}^{m} \left(\overline{X}_i(y) - \overline{X}(y)\right)\left(\overline{X}_i(y) - \overline{X}(y)\right)^T \\
&\quad + \sum_{i=1}^{n}\sum_{j=1}^{m} \left(X_{ij}(y) - \overline{X}_i(y)\right)\left(X_{ij}(y) - \overline{X}_i(y)\right)^T, && \text{(4-12d)}\\
S_{zz} &= n \cdot SP_z + SS_z && \text{(4-12e)}\\
&= n \cdot \sum_{i=1}^{m} \left(\overline{X}_i(x) - \overline{X}(z)\right)\left(\overline{X}_i(z) - \overline{X}(z)\right)^T \\
&\quad + \sum_{i=1}^{n}\sum_{j=1}^{m} \left(X_{ij}(z) - \overline{X}_i(z)\right)\left(X_{ij}(z) - \overline{X}_i(z)\right)^T, && \text{(4-12f)}
\end{aligned}$$

where $\overline{X}_i(x)$, $\overline{X}_i(y)$, and $\overline{X}_i(z)$ are the coordinate vectors of the scan-mean configuration of the part i, and SP and SS are the between-part and between-scan sums of squares. Since the scanning precision is controlled at a much smaller level at the first constraint, the between-scan sums of squares are negligible components in the posterior covariance matrices when compared to the between-part variance part. It is valid in real practice that the RE practitioners should select a CMM or scanner, which has higher precision than the process generating the parts ($t_p >> t_s$). Therefore, our posterior marginal distribution, Equation 4-5, for the mean part model can be approximated here by

$$\mu_x \mid \mathcal{X}(x) \approx t_{m+3}\left(\overline{X}(x), \frac{t_p^2/3 \cdot I_k + SP_x}{m(m+3)}\right), \tag{4-13a}$$

$$\mu_y \mid \mathcal{X}(y) \approx t_{m+3}\left(\overline{X}(y), \frac{t_p^2/3 \cdot I_k + SP_y}{m(m+3)}\right), \tag{4-13b}$$

$$\mu_z \mid \mathcal{X}(z) \approx t_{m+3}\left(\overline{X}(z), \frac{t_p^2/3 \cdot I_k + SP_z}{m(m+3)}\right). \tag{4-13c}$$

In other words, we can treat the mean scan configurations as the "observations" for the Bayesian models, and Equation 4-13 is the corresponding posterior marginal distribution of the mean. In practice, the decomposition, SP and SS components in Equation 4-12, can also be applied to check the above assumption, $t_p >> t_s$, using the analysis of variance techniques [114].

Similar to the case of multiple scans, assume p parts, each of which is scanned n times to achieve the required precision, are already collected, and the corresponding between-part sum of squares, SP_x^p, SP_y^p, and SP_z^p, can be calculated according to Equation 4-13. The variances of m parts can be approximated by

$$\Lambda_x^{n,m} \approx \Lambda_x^{p\to m} = \frac{t_p^2/3 \cdot I_k + m/p \cdot SP_x^p}{m(m+3)}, \tag{4-14a}$$

$$\Lambda_y^{n,m} \approx \Lambda_y^{p\to m} = \frac{t_p^2/3 \cdot I_k + m/p \cdot SP_y^p}{m(m+3)}, \tag{4-14b}$$

$$\Lambda_z^{n,m} \approx \Lambda_z^{p\to m} = \frac{t_p^2/3 \cdot I_k + m/p \cdot SP_z^p}{m(m+3)}. \tag{4-14c}$$

In summary, the RE process planning problem is modeling into an integer programming model with linear objectives and nonlinear constraints:

$$\min_m \quad m \tag{4-15a}$$

$$\min_n \quad n \tag{4-15b}$$

$$\text{s.t.} \quad \max_i \left(q \cdot [\Lambda_i^{s\to n}]^{1/2}\right) \le \delta \tag{4-15c}$$

$$\max_j \left(q \cdot \left[\Lambda_j^{p\to m}\right]^{1/2}\right) \le \epsilon \tag{4-15d}$$

$$m, n \in \mathbb{Z}^+, \tag{4-15e}$$

where $\Lambda_i^{s\to n}$ is the (i,i) element of the matrix $\Lambda^{s\to n} = \Lambda_x^{s\to n} + \Lambda_y^{s\to n} + \Lambda_z^{s\to n}$, and $\Lambda_j^{p\to m}$ is the (i,i)th element of the matrix $\Lambda^{p\to m} = \Lambda_x^{p\to m} + \Lambda_y^{p\to m} + \Lambda_z^{p\to m}$.

4.2.2 Algorithm to Solve the Planning Model

To solve the above RE process planning model (Equation 4-15), we need to change the form of the model constraints. First of all, the maximization constraints can be remodeled as

$$\begin{aligned} q^2 \cdot \Lambda_i^{s\to n} &\le \delta^2, \quad \forall\, i = 1, \dots, k && \text{(4-16a)} \\ q^2 \cdot \Lambda_j^{p\to m} &\le \epsilon^2, \quad \forall j = 1, \dots, k && \text{(4-16b)} \end{aligned}$$

Next, the definitions of the covariance matrices are plugged in and the constraints, after modification, can be written as

$$\begin{aligned} \text{s.t.} \quad & n^2 + a_i n - b_i \ge 0, \quad \forall\, i = 1, \dots, k && \text{(4-17a)} \\ & m^2 + c_i m - d_i \ge 0, \quad \forall\, i = 1, \dots, k && \text{(4-17b)} \end{aligned}$$

where the coefficients $a_i = 3 - q^2 \left(S^s_{x,i} + S^s_{y,i} + S^s_{z,i}\right)/(s\delta^2)$, $b_i = q^2 t_s^2/\delta^2$, $c_i = 3 - (SP^p_{x,i} + SP^p_{y,i} + SP^p_{z,i})/(p\epsilon^2)$, $d_i = q^2 t_p^2/\epsilon^2$, and $S^{s,p}_{x,i}$, $S^{s,p}_{y,i}$, and $S^{s,p}_{z,i}$ are the (i,i)th elements of the matrices $S^{s,p}_x$, $S^{s,p}_y$, and $S^{s,p}_z$. It is easy to see that both constraints have a quadratic form with respect to variables n and m, independently. Therefore, the constraints 4-17a and 4-17b are equivalent to

$$\begin{aligned} & n \ge \frac{-a_i + \sqrt{a_i^2 + 4b_i}}{2} \quad \text{or} \quad n \le \frac{-a_i - \sqrt{a_i^2 + 4b_i}}{2}, && \text{(4-18a)} \\ & m \ge \frac{-c_i + \sqrt{c_i^2 + 4d_i}}{2} \quad \text{or} \quad m \le \frac{-c_i - \sqrt{c_i^2 + 4d_i}}{2}. && \text{(4-18b)} \end{aligned}$$

Furthermore, it is worth noticing that b_i and d_i are always positive. This makes the values of $\frac{-a_i - \sqrt{a_i^2+4b_i}}{2}$ and $\frac{-c_i - \sqrt{c_i^2+4d_i}}{2}$ negative ones, and their corresponding constraints can be dropped. Therefore, the optimization problem can be further reduced to the following model:

$$\min_{m} \quad m \tag{4-19a}$$

$$\min_{n} \quad n \tag{4-19b}$$

$$\text{s.t.} \quad n \geq \max_{i\in\{1,\ldots,k\}} \frac{-a_i + \sqrt{a_i^2 + 4b_i}}{2} \tag{4-19c}$$

$$m \geq \max_{j\in\{1,\ldots,k\}} \frac{-c_i + \sqrt{c_i^2 + 4d_i}}{2} \tag{4-19d}$$

$$m, n \in \mathbb{Z}^+. \tag{4-19e}$$

Then, after reformatting the formulae, this model can be solved analytically, such that $n = \lceil \max_{i\in\{1,\ldots,k\}} \left(-a_i + \sqrt{a_i^2 + 4b_i}\right)/2\rceil$ and $m = \lceil \max_{j\in\{1,\ldots,k\}} \left(-c_i + \sqrt{c_i^2 + 4d_i}\right)/2\rceil$.

For applications, such as biomedicine, culture heritage, etc., where the part is unique, the model can be reduced to discover the required number of scans by dropping the objective and the constraints corresponding to m. Since n can be determined independently from m, the number of scans is just $\lceil \max_{i\in\{1,\ldots,k\}} \left(-a_i + \sqrt{a_i^2 + 4b_i}\right)/2\rceil$ in the above model.

4.3 Validations and Case Studies

4.3.1 Simulation Experiment

We now illustrate and validate the VDA framework mentioned above and process planning with a simulated hemispherical design. Configurations are simulated from a design with a hemispherical shape, whose radius is 20 millimeters (mm). The case in which one unique object is available is first studied. A multiple-scan procedure is implemented to construct a mean-scan configuration to achieve high precision. Assume the standard deviation for each of the points collected by the emulated scanner is $t_s = 0.01$ mm. Then, $\mathrm{N}(0, 0.01^2/3)$ independent and identically distributed (*i.i.d.*) errors in the unit of mm are added to each coordinate of the landmarks to emulate the random error in the scanning process. There are 100 layers in total, while 50 landmarks are simulated on each layer. The simulation experiment is designed in a sequential fashion so that the optimal number

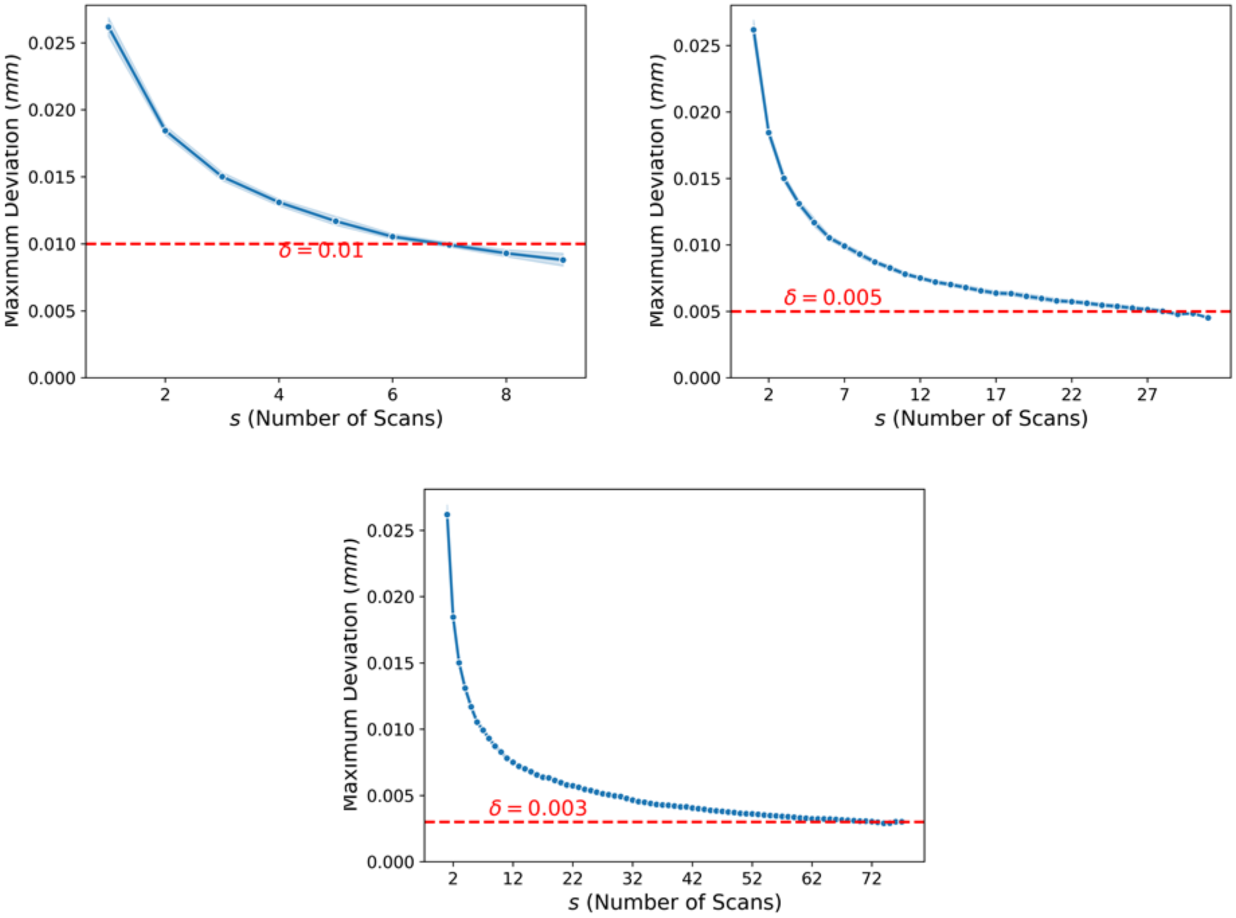

Figure 17: Process planning results of the simulation experiment that the multiple scans for a single hemispherical part are planned at three δ values: 0.01, 0.005, and 0.003 mm. The simulation experiment is replicated 30 times for each setting.

of scans is calculated by solving Equation 4-15 after each simulated scan is obtained, with 30 replications. The emulated scanning process stops once the optimal number of scans is reached or, in other words, the current number of scans is greater than or equal to the optimal number. The process-planning model's performance is evaluated by setting the δ value, or the precision of the mean-scan configuration, at three different levels: 0.01 mm, 0.005 mm, and 0.003 mm. Simulation results are presented in Figure 17. As the number of scans increases, the mean scan configuration moves closer to the nominal design regarding

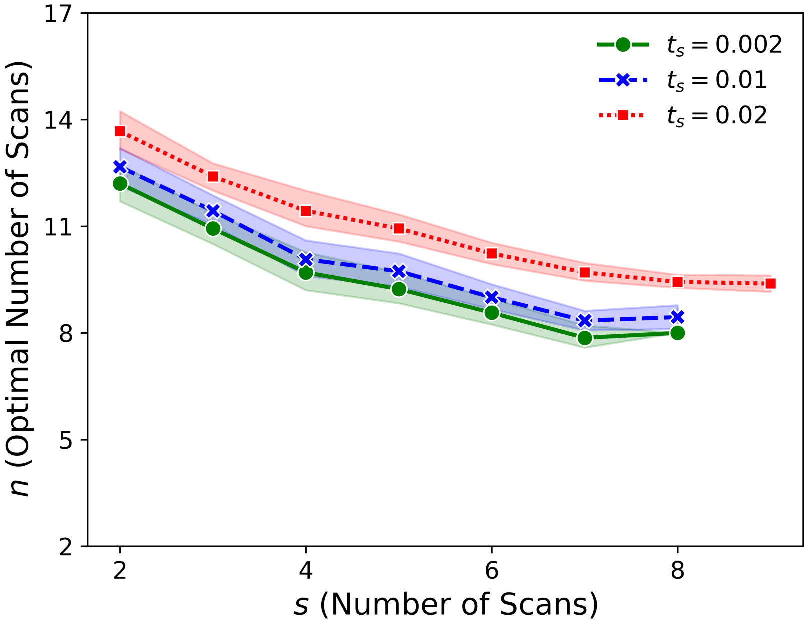

Figure 18: Process-planning results for multiple scans of a single hemispherical part with three different prior settings of t_s: 0.01, 0.002, and 0.02.

the maximum deviation among all the corresponding points. Furthermore, this result verifies that the process-planning model could provide an accurate number of scans to achieve the target precision requirement. One interesting observation is that the decay is not linear in the maximum deviation to the increase of the scan number. The mean scan configuration has a fast precision improvement at the early stage when the number of scans is small; as the number of scans increases, the rate of the improvement tends to flatten. Even though the mean-scan configuration can improve the precision by increasing the number of scans, each scanner has a precision ”limit” due to the constrained resources.

Moreover, the prior information on the scanner variances, t_s, in the Bayesian model (Equation 4-2), is also evaluated using three values: the designed variance for the emulated scanner (0.01), a smaller value (0.002), and a larger value (0.02). The δ value is controlled at 0.01 mm. With the same stopping criteria as shown above, the result is presented in Figure 18. This prior information, t_s, could influence the optimal number of scans. If the

t_s value is much smaller than the true scanner variance, it has a risk of early stopping that leaves the model precision unsatisfied. On the other hand, if the t_s value is large, then it may require more scans for the RE project to reach the precision requirement. Therefore, a careful precision analysis of the utilized scanner, together with the precision specification in the scanner's manual, is recommended for t_s value determination. However, this prior information could fade out as the number of scans increases. The sum of square components in the covariance becomes more important, reflecting the scanner's "true" covariance structure.

We are also interested in re-manufacturing cases where multiple legacy parts of the same design exist. The simulated design is similar to the above hemispherical shape. Relatively large noises are generated from *i.i.d.* $\mathrm{N}(0, 0.1^2/3)$ in unit of mm for each simulated circular layer to emulate the variance caused by manufacturing process with variance $t_p = 0.1$. Simulated samples are also generated in a serial manner, similar to the real practice that the parts are collected and scanned sequentially. Similarly, $\mathrm{N}(0, 0.01^2/3)$ *i.i.d* errors are added to each coordinate of the landmarks to emulate the random error in the scanning process. The performance of the process planning model is evaluated at $\delta = 0.01$ and three ϵ values—0.1 mm, 0.05 mm, and 0.03 mm. The decision on the required number of parts is again made sequentially; for each replication, the project stops if the optimal target numbers of parts are reached. The simulation results are presented in Figure 19. The results are similar to those of the previous simulation on multiple scans. As the number of collected parts increases, the mean part configuration becomes closer to the design. Again, the relationship between precision, or the maximum deviations, and the part number is not linear. Another observation is that the proposed process-planning model works well when ϵ is controlled at a medium-to-large value; for a very small ϵ, compared with the process variation, an excessive number of parts may be required. This phenomenon is also caused by the shape of the decay function; at the tails of this decay, the shape becomes flat and very sensitive to little changes. With the optimized number of parts, the mean part model could reach the precision constraints with a few more scans. This validates our approximation of the posterior marginal distribution in Equation 4-13. However, since the process-planning model, Equation 4-19, is solved sequentially so that the number of scans for each part is solved first, we recommend in practical applications to control the scanning precision δ at a much smaller level than the

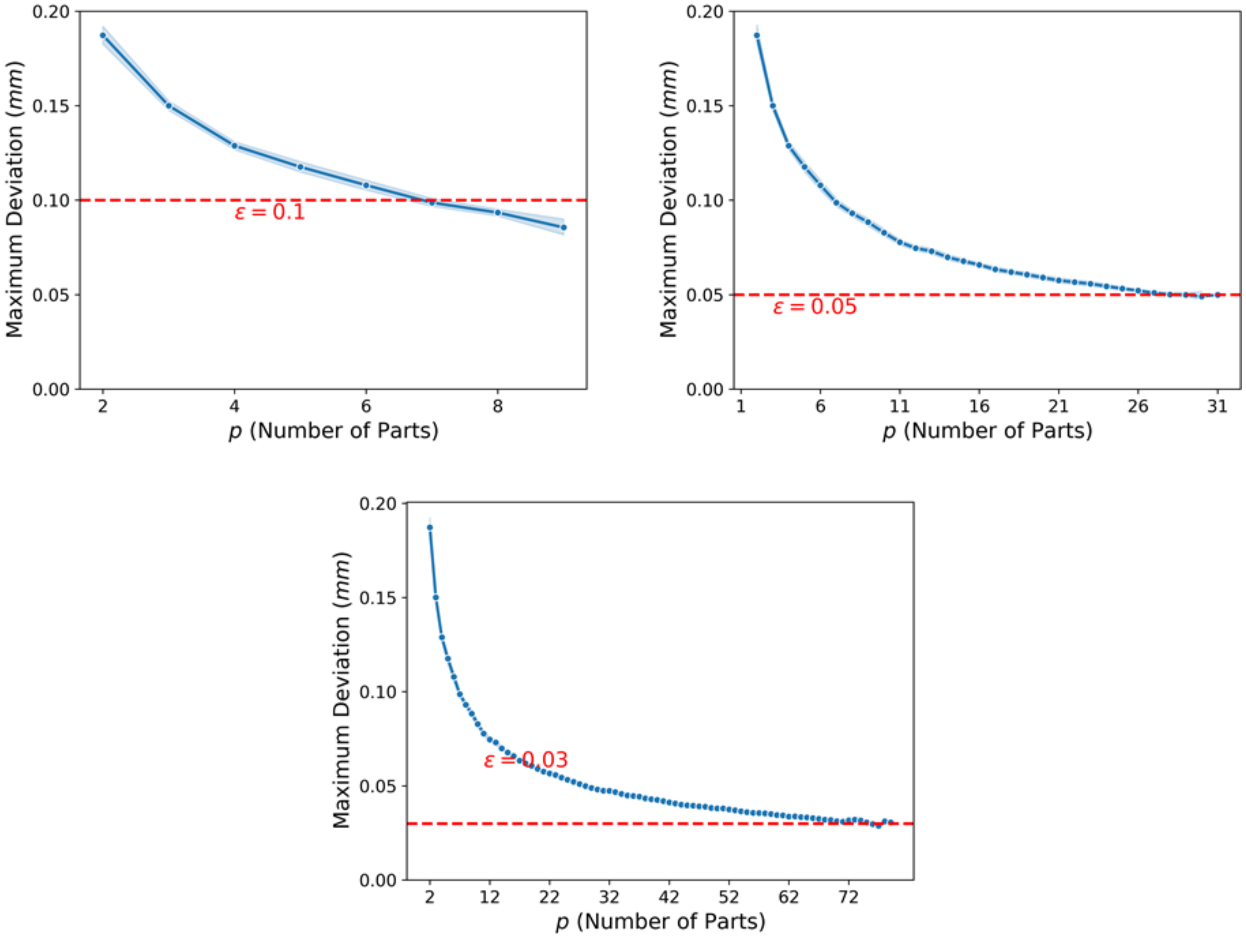

Figure 19: Process-planning results of the simulation experiment that the multiple scans of multiple parts with the same hemispherical design are planned at three ϵ values: 0.1, 0.05, and 0.03 mm and fixed δ value, 0.01. The simulation experiment is replicated 30 times for each setting.

final model precision ϵ to avoid excessive part requirement (recommended that δ is selected to be about 1/5 or 1/10 of ϵ). Otherwise, because the number of scans is optimized at first, as long as the scan-precision constraint is met, it may require many more parts to compensate for the precision constraints on the mean part configurations.

t_p value is also controlled at three levels—0.2, 0.1, and 0.02—for the sensitivity study of the prior information in the Bayesian modeling. Results are presented in Figure 20. If the

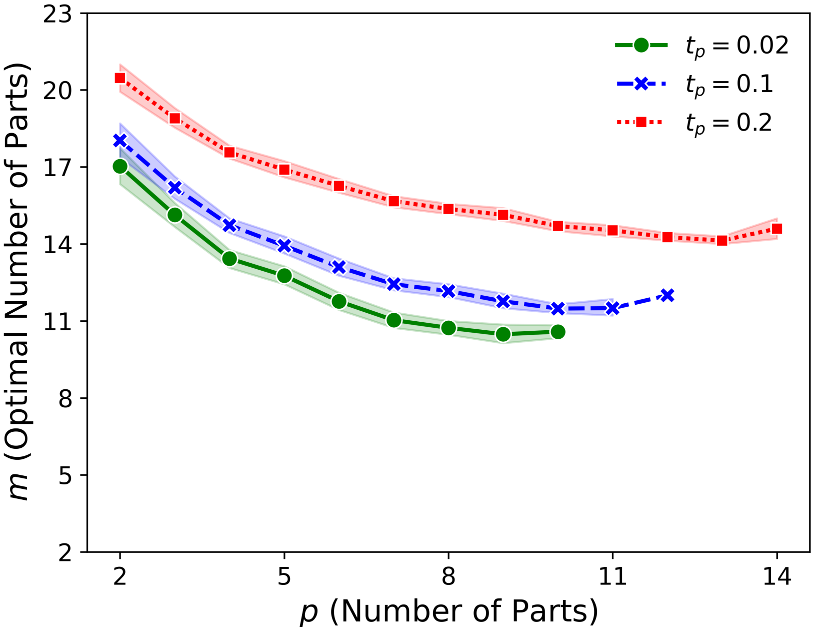

Figure 20: Process-planning results for multiple scans of several hemispherical parts with the same design at three different prior settings of t_p: 0.1, 0.2, and 0.02.

t_p value is set to be small, it has a risk of early stopping that the model precision can be lower than the requirement. Yet, if the t_p value is large, redundant parts are required, which increase resource consumption. Therefore, a careful precision analysis of the production variances based on the available parts or using the geometric hints is recommended for t_p value determination.

4.3.2 Unique Freeform Part

An arbitrary unique freeform object, shown in Figure 21, is printed by the LulzBot TAZ 3D printer (Figure 22(b)), an FDM machine, using gold metallic 2.85 mm polymer. The part is unique because the printed part is of high variability, which causes the part to deviate from the initial design and result in making the actual dimensions unknown. Therefore, multiple scans are required to meet certain predetermined precision. The point-cloud samples are collected through 25 independent sequential scans of the objects using the FARO Platinum

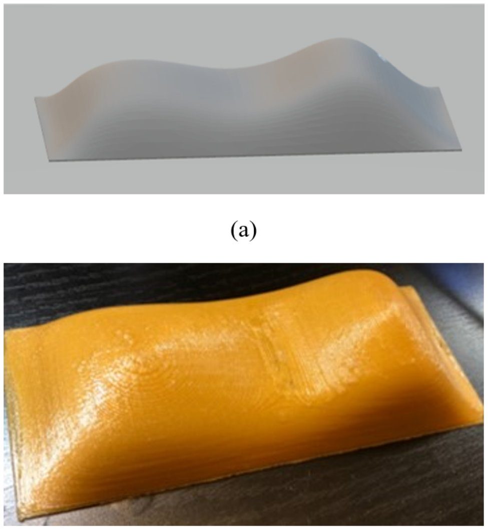

(a)

(b)

Figure 21: The design and the physical part of the freeform object.

8' Arm Laser Scanner (Figure 22(a)). According to the scanner's manual, the standard deviation t_s is about 0.05 mm, which can be used as the prior information to our process planning model. Since only the freeform surface is of interest and the bottom of the object is a flat surface, the support surface method can be implemented as CP to generate landmarks. The object does not have a datum feature; therefore, a PPA algorithm is implemented to register the generated landmarks, which can be used for the following analysis. The results of process planning are shown in Table 2, where the value δ is controlled at four levels. From the results, it can be easily seen that the number of scans is required to be higher when the predetermined scan precision is smaller, which is similar to the above simulation results. Also, the optimal number of scans is not linear to δ that, for high precision requirements, such as $\delta \leq 0.005$ mm, requires over 73 scans.

To see the performance of the mean-scan configurations over the different scan numbers, a "true" model of the object needs to be acquired. A mean-scan configuration based on another independent 25 scans is treated as the benchmark configuration. Both the Procrustes distance and the maximum deviation are utilized to measure the difference between the

(a) (b)

Figure 22: Experimental equipment: (a) FARO Platinum 8’ Arm Laser Scanner; (b) LulzBot TAZ 3D printer.

Table 2: Optimal calculated number of scans to meet the predetermined precision levels for unique freeform part.

Predetermined Scan Precision δ (mm)	Optimal Number of Scans n
0.05	2
0.03	4
0.01	27
0.005	104

benchmark and the mean-scan configurations over various scan numbers, as presented in Figure 23. The mean-scan configurations are built through a permuted scan order procedure with 30 replications. Both the Procrustes distances and the maximum deviations between the benchmark model and the mean scan configuration, as well as the confidence bandwidth,

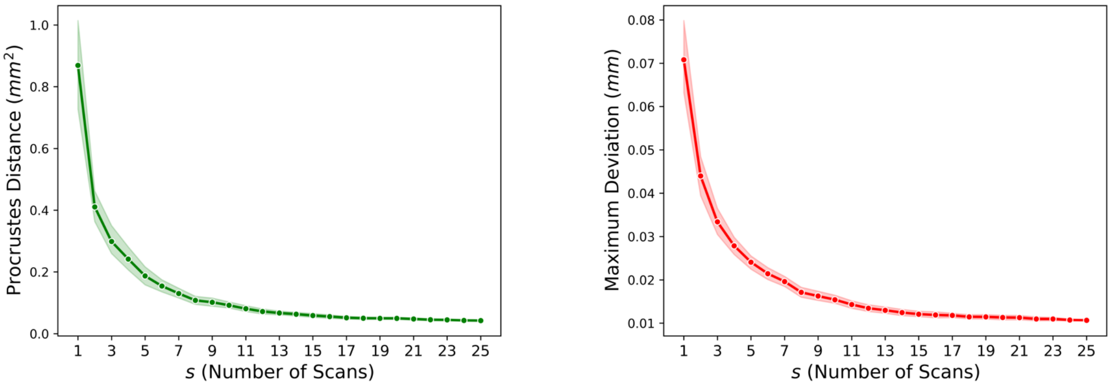

(a) (b)

Figure 23: The Procrustes distance and maximum deviation between the mean part configurations with different number of scans and the mean configuration from 25 independent scans for the freeform part in Figure 21.

become smaller as the number of scans increases. However, the trends are not linear in the number of scans. It can be seen that after about 12 scans, the trends in both figures tend to be flat; with more scans, the mean scan configurations do not improve significantly. Table 2 also illustrates this behavior. When the precision is controlled by less than 0.03 mm, the required number of scans increases exponentially.

4.3.3 Multiple Mechanical Parts

Another case study is based on RE for the re-manufacturing of legacy parts. Five mechanical parts were collected from the University of Pittsburgh's Manufacturing Assistance Center (MAC). Trainees from MAC using numerical control machines manufactured the mechanical parts. The CAD design and the raw point cloud and generated landmarks of the parts are shown in Figure 24 and Figure 25, respectively. After inspection, all the parts are within the tolerance requirements, identified as qualified parts. Due to the high precision of the numerical control machines, Renishaw Cyclone Touch Probe Scanner, a CMM, was used to survey the surface points. According to the manual, CMM's repeatability is 5 μm,

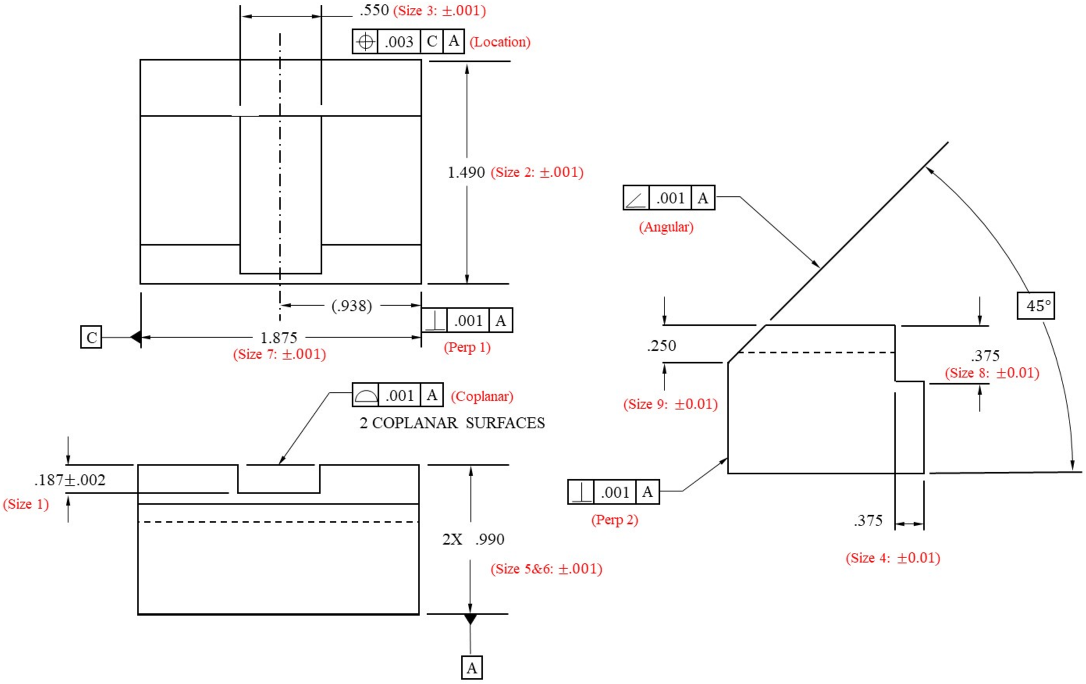

Figure 24: The original CAD design of the collected machined parts.

which implies that $t_s \approx 0.005/3$ mm. The point clouds from multi-view were registered and segmented using Geomagic Studio 2014. Since the digitization tools perform poorly near the sharp edges or vertices, the points near the edges are manually removed from the point clouds to prevent them from affecting the results. The edges and vertices are then interpolated through parametric surface-fitting algorithms. The PC plane is used in F-CPP to generate landmarks for each of the thirteen surfaces of the part. According to the design in Figure 24, the left, bottom, and back surfaces are the datum features. Then, the entire landmarks are registered using DGPPA by the ones on the datum features. Next, the registered whole-body landmarks can be used for process planning. The prior information of the machining processes is derived from Chapter 5, where detailed tolerance analysis is presented and summarized in Table 3. According to the table, t_p is selected to be about 0.0405 mm, since the maximum deviation is considered in our model.

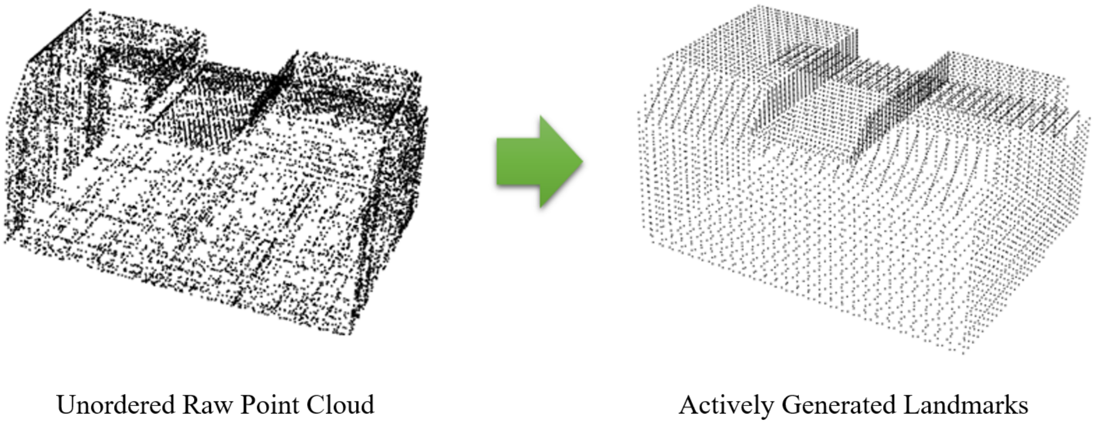

Figure 25: Raw-point cloud and generated landmarks of a machined part.

The process planning results are shown in Table 4. Only one scan is required for each part when the scanning precision is controlled at 0.005 mm. Therefore, mean scan configurations generated by three CMM scans, for conservative purposes, are accurate enough for controlling the scanning precision at 0.005 mm or lower when the number of parts is small and the part configuration constraint is controlled at relatively loose levels. In this case, the major source of variation in the mean part configuration is introduced through the original manufacturing process. The number of parts required tends to be large if the part precision is determined to be small.

On the other hand, the numbers of required parts calculated by the proposed process-planning model have a similar pattern to the simulation study. When the controlled precision value is smaller than or equal to 0.03, more than 33 parts need to be collected to reach the requirement. In real practice, the number of available legacy parts is usually small, for example, five in our case study. To collect extra parts in some cases could require excessive resources.

Since the initial design is known, the true configuration can be formulated according to the CAD design. The Procrustes distance and maximum deviation between the mean part configurations and the true configuration are shown in Figure 26. Both trends become

Table 3: Production variances for each of the tolerancing features.

Tolerancing Feature	Standard Deviation of Dimensions
Size 1	0.0152
size 2	0.0001
Size 3	0.0003
Size 4	0.0001
Size 5	0.0047
Size 6	0.0051
Size 7	0.0014
Size 8	0.0027
Size 9	0.0030
Perp 1	0.0004
Perp 2	0.0022
Coplanar	0.0038
Angular	0.0405
Location	0.0098

Table 4: Optimal calculated number of scans to meet the predetermined precision levels for machined parts (scan precision δ controlled at 0.005 mm; each part is scanned three times).

Predetermined Part Precision (mm)	Optimal Number of Required Parts m	Optimal Number of Required Scans n
0.15	3	1
0.1	10	1
0.05	46	1
0.03	132	1

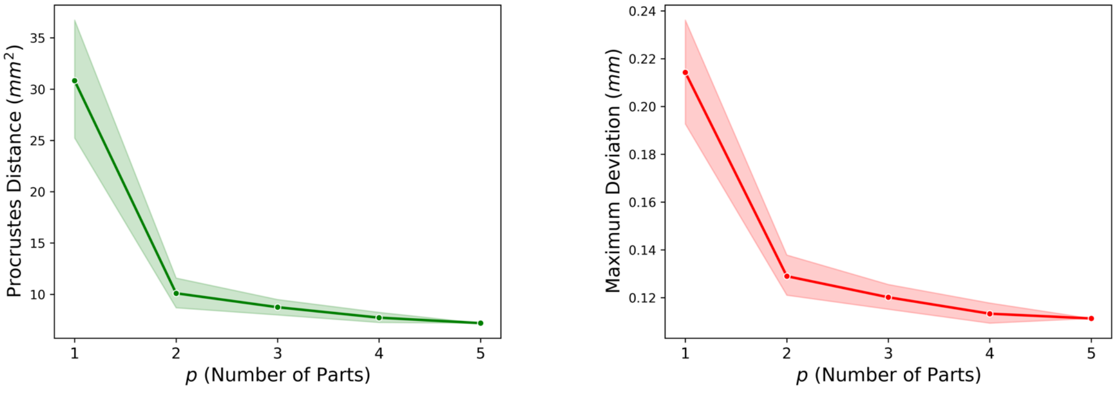

(a) (b)

Figure 26: The Procrustes distance and maximum deviation between the mean part configurations with a different number of parts and the true configuration for the machined part.

tighter with lower variance as the number of parts increases. Since the mean dimensions may deviate from the true design in a real production system, the Procrustes distance and the maximum deviation tend to converge to non-zero constants. This off-targeting behavior exists ubiquitously in the analysis of the production systems [180]. For RE applications, where the true design is unknown, the mean part configuration still provides a more robust estimator than any single-part model. A small point worth noticing is the maximum deviation for a single part in Figure 26. The mean and confidence band show that the maximum deviation of each part is between $(0.19, 0.24)$ mm (or $(0.0075, 0.0095)$ inch), which is out of the maximum tolerance in the design (Figure 24). Although DGPPA aligns the configurations by registering the datum features, the registration is based on the sum-of-squares-loss (Procrustes distance). Therefore, the resulting registered configurations do not minimize the maximum deviations among them. On the other hand, the tolerance design is based on the ASME Y14.5 standard, where the Taylor, or envelope, principle and ideal datum feature principle are defined. Therefore, the mean part configuration of the mechanical parts, even if it is a good estimator of the true design from the statistical point of view, cannot be directly used for tolerancing applications, such as tolerance estimation in [55].

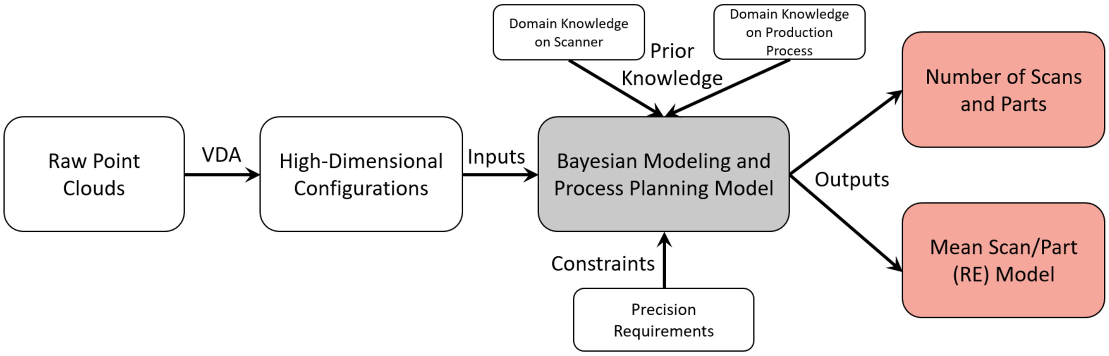

Figure 27: Process map of the process planning model presented in Chapter 4.

4.4 Summary and Conclusions

This chapter utilizes the VDA framework to create a new estimator with a smaller variance of the original design through scanning multiple parts with the same design, if any, and multiple times for each of them, as shown in Figure 27. This framework can be directly used in various applications, such as legacy parts re-manufacturing, producing customized prostheses, etc. A Bayesian model with "weakly" informative priors from the manufacturing and metrology domain knowledge is built for the mean configurations to describe the statistical properties. As one application of VDA, we describe a RE process-planning model based on the Bayesian posterior marginal distribution of the mean configurations after observing multiple point clouds. By controlling the precision requirements at both scanning and part levels, the optimization model provides an optimal required scan and part number for RE practitioners.

The types of manufacturing applications we studied focus on the products close to the original design with a small variance factor, which forms the framework's basic assumption. Simulation studies are presented to verify the performance of the proposed method. Two real case studies illustrate how to implement this framework and show that the mean scan and part configurations concentrate around the true object/design with lower variance. This framework addresses the major concerns for the precision of RE in real applications.

One area of future work lies in real applications. In the case study, we observe that the precision improvement in both the mean-scan configuration and the mean-part configuration is not linear to the number of scans. On the one hand, if the controlled precision is not well-selected, the process planning model may provide unreasonably large numbers of scans and parts. On the other hand, in real practice, the sample of available parts is usually small, which may not reach the planned number. We are developing a method to quantify the tolerance for mean scan and part configuration and integrate them into the tolerance stack-up analysis for re-manufacturing to solve these issues.

5.0 Tolerance Estimation for Reverse Engineering Based-Re-Manufacturing Systems

Tolerances are critical to the product's design, manufacturing, and quality. However, tolerances are often overlooked in a reverse engineering (RE) process for industrial applications, especially in legacy parts or spare parts re-manufacturing. Ignoring tolerances could either unnecessarily call for high precision re-manufacturing processes or make the reproduced parts unqualified. In this chapter, Section 5.1 first proposes a general routine for estimation of the tolerance based on the dimensions of several physical parts with the same design and the knowledge of production-process analysis. Next, we review and classify the tolerance classes defined in GD&T standards and develop the approaches to extract dimensions from the point cloud for each tolerancing type for both tolerance estimation and AM inspection purposes. The performance of the proposed framework is verified and evaluated via an RE case study. Tolerance-estimation results based on a small batch of machined parts are compared with their known tolerancing specifications with a discussion on the proposed method in Section 5.3. Finally, this chapter concludes with a discussion on how to choose an estimation routine in real practice. The tolerance-estimation method proposed here plays two important roles in this dissertation. First, as shown above, it helps to estimate the tolerance design for re-manufacturing and complete the design information for RE. In addition, this method also provides a rough estimation of the variance of the original production process. This variance estimation can be utilized for the accurate process planning presented in Chapter 4. The remainder of this chapter appears in [56].

5.1 A Methodological Framework for Tolerance Estimation

The concept of tolerancing stems back to the beginning of mass production. Due to the limitations of machining processes and specific functionality requirements, complex designs are usually decomposed to a set of simple designs for multistage machining processes [172], or simple parts and sub-assemblies for cost-saving purposes, such as simple process planning or part interchangeability [20]. With an increasing interest in global mass production during the past few decades, various topics have been developed along each manufacturing stage, such as tolerance analysis and tolerance allocation. Hong and Chang [68] provide a thorough review of each topic of tolerance research. However, all the topics are developed for the traditional manufacturing processes, from design and manufacturing to inspection. RE is a "non-traditional" manufacturing process that, instead of adding value to the materials, transforms the physical parts back to the digital world to estimate the original unknown design. Therefore, tolerance estimation can be seen as an inverse problem of classic tolerance topics. Previous research on tolerance analysis or synthesis usually transforms the dimensions of the actual feature into a new space for analytical convenience [109, 146, 147]. Two significant issues exist in these models when applied to RE research: (1) these models were developed for either tolerance stack-up analysis or assembly simulation purposes, which are not usually consistent with the GD&T standards and (2) a major foundation of most models is the assumption of known design, which is critical to the properties of the analytical spaces, such as T-Map® [6]. Little design information is known about RE applications other than the physical parts. Therefore, the tolerance information needs to be inferred directly from the point cloud. Recently, Schleich and Wartzack [146, 147] and Polini and Corrado [133] have proposed the concept of skin-model shapes for tolerance analysis and, generally, digital twin analysis. Their method simulates the point cloud from the CAD model and performs tolerancing studies, such as tolerance evaluation, assembly simulation, on the simulated points.

In production systems, the manufacturing processes are usually selected and planned based on the geometric and tolerance designs. Thus, to estimate tolerances from physical parts, the latent relationship between the tolerance specification and the parts' dimensions should be first set up. First, the original tolerance design determines the process planning and inspection processes. A primary assumption of this study is that all the dimensions of the parts are within the original tolerance specifications. Since all the parts are either collected from the original vendor or disassembled from the products, they pass the inspection or quality assurance by the manufacturer. Therefore, the regions determined by the upper and lower boundaries of the examined dimensional values should be at least within the original tolerance specifications. However, this type of estimation is conservative in that the estimated tolerance regions might be too narrow, which could unnecessarily call for high-precision re-manufacturing processes. Due to the variable nature of the original manufacturing processes, each dimension of the produced part can be modeled as a random variable. Boundary estimators are also random variables determined by both the part's dimensional value and the number of available parts. The number of available parts in an RE practice is usually small due to either the budget constraints or the parts' availability. In this case, this type of empirical tolerances may not be an accurate estimator of the original tolerance design.

One possible extension of the boundary estimator relies on the variable nature of the dimensional values. If a feature can be evaluated through a dimensional value, then this feature dimension can be modeled as a random variable whose distribution is controlled by the geometric design and the original manufacturing system. Here, the feature size in the American Society of Mechanical Engineers Y14.5 [123] standard is excluded since it is defined as the envelope of the feature instead of a specific dimensional value. This particular case will be discussed in the following section. Because of the variable nature of the dimensions, the manufacturers usually implement either the six-sigma (6σ) policy or the process capability ratio (PCR) policy for process design and planning. If the dimensional variable follows a univariate distribution, the region limited by the six standard deviations from the mean of the distribution could control the defective rate at a small level. Following this policy, the 6σ region of the dimension produced by the original manufacturing process should be within the tolerance specification [181]. Since the standard deviation of the actual process is unknown, it could be estimated from the parts' dimensions. Two standard deviation estimators are available to find the 6σ region based on different sample sizes [114]. One is based on sample range statistics if the sample size is less than 10. The other one is the square root of the sample variance if the sample size is relatively large.

Furthermore, another widely used process-control policy is based on PCR [88, 27], which is used extensively in manufacturing industries for process parameter and tolerance design [170]. The classic PCR, C_p, is defined as

$$C_p = \frac{USL - LSL}{6\sigma} \tag{5-1}$$

where USL and LSL are the upper and lower specification limits, respectively, and the $USL - LSL$ is the width between the tolerance limits. Even though other more advanced process capability ratios, such as C_{pk}, C_{pc}, etc., are available, these indices were developed to be more sensitive to the off-center processes or the non-normal distributions. Kotz and Johnson [90] provide a detailed review paper on this topic. However, in our situation, the original design is unknown, and information about whether the process is off-center or has a non-normal distribution is missing. Therefore, the C_p index is the only one that can be used in this case with the following assumptions:

- The dimension of interest has a normal distribution;
- The original manufacturing processes that produce the part is in statistical control; and
- The process means are located at the centers of the lower and upper specification limits.

With the σ estimation methods shown above, the width of the tolerance region, T, can be estimated by

$$T = 6\sigma C_p, \tag{5-2}$$

and the value of C_p can be assumed to have a standard value in industrial applications, such as 1.33 or higher [114]. The normality assumption in the C_p index is strong. A nonparametric version has been proposed by Polansky to relax such an assumption [131, 132]. The key idea is to inspect the probability p that is

$$p = P(X > USL \text{ or } X < LSL), \tag{5-3}$$

where X is the random variable representing the quality characteristic of the feature of interest. Without the normality assumption, the distribution of the random variable X is estimated by the inspected values from the created parts using nonparametric methods, e.g., kernel smoothers. Even though the parametric-distribution assumption can be relaxed, the nonparametric methods require a relatively large sample size to enjoy the nice asymptotic property for estimation. In the RE-embedded re-manufacturing applications, the number of available parts is usually small. Therefore, nonparametric methods may not be appropriate for our study.

5.2 Dimension Evaluation Algorithms for Tolerance Estimation

In Section 5.1, the methodology to estimate original tolerance design based on parts dimensions is proposed. Evaluating the dimensions from the point cloud is critical for both tolerance estimation and quality assurance for AM-created parts. Since the engineering design and inspection rely on tolerance specification from a GD&T standard, the dimension evaluation procedures also follow the standard. Two GD&T standards that are widely adopted around the world are the ASME Y14.5-2009 [123] and the International Organization for Standardization Geometrical Product Specification (ISO GPS) standards (ISO/TC 213). Tolerances can be broadly divided into six categories based on their definitions [68]: size/dimensional tolerance, form tolerance, location tolerance, orientation tolerance, profile tolerance, and runout tolerance, where the last five are known as geometric tolerances. For reverse engineering applications, only the first four types of tolerances are considered in this study. The profile-tolerancing zone is defined as the equal distance region around the design surface, which is usually unknown in RE applications. Further, the runout tolerance is often related to a rotational feature concerning the datum axis, which is either hard for the 3D scanner to capture or not scannable. As a result, this study omits these two tolerancing types.

Algorithms to extract dimensions related to all the other four tolerances from the point cloud will be briefly discussed in this section. First, algorithms for extracting dimensional values related to size/dimensional tolerances are proposed based on both ASME and ISO standards. Then, the algorithm to set up the datum system is discussed. Next, algorithms extracting dimensional values related to the other three geometric tolerances—form, location, and orientation tolerances—are presented based on their specific datums.

5.2.1 Size/Dimensional Tolerance

The dimensional tolerance or fit is used in ISO standards to define the limiting region for feature size. It is both critical and ubiquitous in GD&T standards. In ASME Y14.5-2009, the terminology with a similar purpose is size tolerancing. In this class of tolerance, two major types of features are considered: the planar feature, whose size is the distance between two planar features, and a cylindrical feature, whose size is the cylinder's radius of interest.

The definition of size tolerance is one of the significant differences between ASME and ISO standards. This difference is rooted in the inspection preferences of the manufacturing industries in North America and Europe. In North America, where the concept of mass production was developed, individual gauges are designed to test whether parts are intolerance for time-saving purposes, while in Europe, a CMM is widely adopted for inspection because of its versatility and flexibility. As a result, the ASME standard relies on the Taylor principle or envelope principle, often referred to as a preference for the "hard-gauge" standard. Therefore, ASME Y14.5-2009 considers the control of all points on the surface or a feature using the envelope or the maximum and least material conditions (MMC and LMC). In other words, the ASME standard requires calculating an envelope that covers all points on the feature. From the mathematical definition point of view, the MMC and LMC correspond to the envelopes covering the features with minimax and maximin distances. In inspection, both the minimum and maximum material conditions should be located within the tolerance region for the qualified parts. The algorithm to extract the sizes of the planar feature and cylindrical feature from the point cloud is illustrated in Figures 28 (a) and (b), respectively. For the planar feature, the convex hulls of both planes are computed via algorithms, such as the QuickHull algorithm [10]. Then, let f_{ijk} be the facet of the convex hull m_s determined by point i, j, and k on plane P_s, where $s \in \{1, 2\}$. The MMC and LMC for the planar feature can be computed by

$$MMC = \min_{s\in\{1,2\},\ t\in\{1,2\}\backslash s} \ \min_{f_{ijk}\in P_s} \ \max_{p\in P_t} d(f_{ijk}, p), \tag{5-4}$$

$$LMC = \max_{s\in\{1,2\},t\in\{1,2\}\backslash s} \ \max_{f_{ijk}\in P_s} \ \min_{p\in P_t} d(f_{ijk}, p), \tag{5-5}$$

where $d(f, a)$ is the Euclidean distance between plane f and point a. It is relatively difficult to extract the cylindrical feature for the MMC and LMC. In this study, a heuristic method—the least-squares algorithm—is implemented to calculate both boundaries, shown in Figure 28 (b). First, all the points of the cylindrical feature are projected to the 2D plane. The least-squares fitting algorithm is applied to the projected points to find both the centroid and the mean radius. Then, the values for MMC and LMC are the maximum and minimum distance between the projected points and the least-squares centroid.

Since the size tolerances are measured and represented through MMC and LMC, no dimensional values are directly extracted if ASME Y14.5-2009 is selected as the GD&T standard. Therefore, both the 6σ and PCR methods cannot be applied to this case. Fortunately, MMC and LMC are very sensitive to the outliers, and, therefore, the estimated tolerance would not be too narrow for re-manufacturing.

However, the ISO standards focus on the least-squares size of a feature known as "CMM Friendly." The algorithms for both the planar feature and the cylindrical feature are presented in Figures 28 (c) and (d). For the planar feature, the least-squares fitting algorithm is applied to one of the planes. Then, the dimension of the planar feature is the average of the distances between the fitted plane and the points on the other plane. In the case of cylindrical features, the algorithm is the least-squares fitting in the ASME method. Instead of finding the envelopes, the fitted mean radius is the size of the cylindrical feature. Unlike the ASME's philosophy, the sizes extracted according to ISO standards are usually robust to the outliers, making the boundaries of the surveyed dimensions comparatively tight. Yet, since the direct dimensions are provided by the ISO algorithms, 6σ and PCR methods can be implemented to further expand the estimated region.

5.2.2 Establishing the Datums

A datum plays a critical role in the following geometric tolerances, including form, location, orientation, and profile tolerances, from both the definition and inspection perspective. Since trivial differences exist between ASME and ISO standards, from now on, the definitions from ASME Y14.5-2009 [123] and ASME Y14.5.1M-1994 [122], the Mathematical Definition

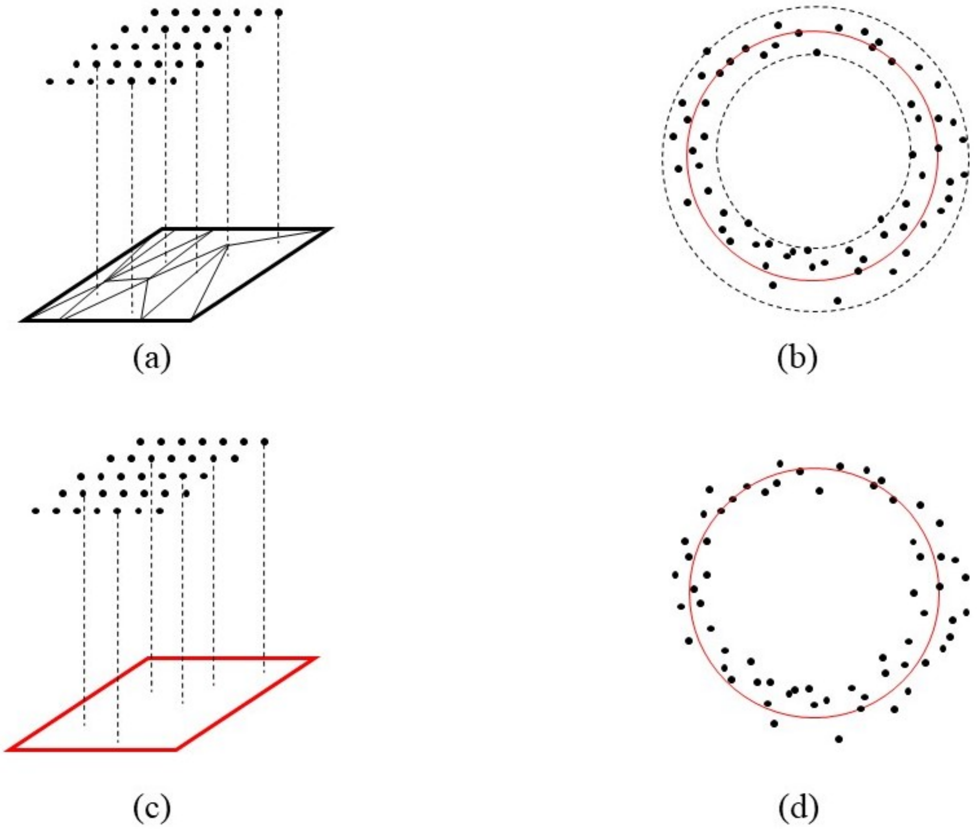

Figure 28: Methods to estimate tolerance of size from the point clouds: (a) extracting MMC and LMC for planar feature based on ASME Y14.5; (b) extracting MMC and LMC for circular or cylindrical feature based on ASME Y14.5; (c) extracting dimensional value for planar feature based on ISO standards; and (d) extracting dimensional value for circular or cylindrical feature based on ISO standards.

of Dimensioning and Tolerancing Principles, are utilized for datum frame establishing and dimension extracting. As for ISO standards, interested readers could refer to the work proposed by Schleich and Warzach [147], which is a similar but different framework to evaluate tolerances for skin model shape.

The concept of datum was developed to constrain the degrees of freedom of the parts for manufacturing and inspection purposes. In practice, the datum is usually established by attaching the part to a stable piece of equipment, such as the machine table or surface plates; in GD&T standards, it is presented as the datum feature simulator, which refers to ideal planes, points, or axes. Since the reverse engineering model in this study is either based on the whole-body scan or the mean configuration of several scans, the definition of a datum feature simulator is utilized to establish datums. Because the original process equipment is missing, the actual supporting structures and contact points are unknown. Therefore, the datum feature simulator is a more comprehensive and reasonable choice. Furthermore, choosing datum features heavily depends on the part designs and domain knowledge, and automated datum selection is still of research interest. In this study, we assume the datum features have been chosen. The plane-type datum features are considered in this study for reverse engineering applications.

Instead of defining a specific plane as the datum, multiple valid datums could be established from a datum feature. For example, if a planar feature is chosen as the datum feature, then the set containing all the planes defined by at least three points on the feature, and above which the entire point cloud lies, can be defined as a candidate datum set. The facet subset of the convex hull of the datum feature, which satisfies the above condition, is the minimum candidate datum set. The QuickHull [10] algorithm can be applied to determine the minimum convex hull. Then, the candidate datum set could be established through iteratively screening the facets by checking whether the point-to-facet direction is opposite to the out-of-material direction of the datum feature. Next, following the minimax and maximin conditions defined by the target tolerance, a specific datum and its corresponding dimensions could be found.

Since each datum establishes and fixes 3 degrees of freedom, a datum reference frame is required to remove all 6 degrees of freedom for manufacturing and inspection purposes, including translations in the x-, y-, and z-directions and rotations around them. One possible practice is to define three planar datum features to establish the datum reference frame. Like the candidate datum set, the candidate datum reference frame set can be established, within which the actual datum reference frame can be determined by the minimax or maximin condition for a specific tolerance type. The three planar datum features are ranked as primary, secondary, and tertiary datum features, respectively. The secondary datum is constrained to be perpendicular to the primary one, while the tertiary datum is defined to be orthogonal to both the primary and secondary datums. Therefore, within the tolerance estimation study, the candidate reference frame set can be found by finding the primary candidate datum set. For each primary datum candidate, the corresponding datum reference frame candidate is unique since the secondary and tertiary datums are restricted by the mutual orthogonal conditions and the points supporting constraints defined for datums. Specifically, the algorithm for the datum reference frame is as follow:

1. Apply the QuickHull algorithm to find the convex hull of the points corresponding to the predetermined primary datum feature;
2. Find the subset of the facets of the convex hull, F, within which the whole point cloud is on one side of the facet; and
3. For each component, f_{1i}, of $\mathcal{F}$:
   a. Find the plane f_{2i} with respect to the predetermined secondary datum feature, which is perpendicular to f_{1i};
   b. Find the plane f_3 with respect to the predetermined tertiary datum feature, which is perpendicular to f_{1i} and f_{2i}; and
   c. Append $f_{1i}, f_{2i}, f_{3i})$ to the set $\mathcal{D}$.

Then, the set $\mathcal{D}$ is the candidate reference frame set. Next, the algorithm to extract dimensional values for each type of geometric tolerances is discussed. From now on, let $\mathcal{F}$ and $\mathcal{D}$ be the candidate datum set for a specific datum feature and candidate reference frame set, respectively, which the application context determines.

5.2.3 Tolerance of Form: Straightness and Flatness

Four types of form tolerances are defined in ASME Y14.5-2009: straightness, flatness, circularity, and cylindricity. The definition and algorithms to find ”dimensions” from the point cloud for each type will be given in this section. Since ”dimensional” values or the

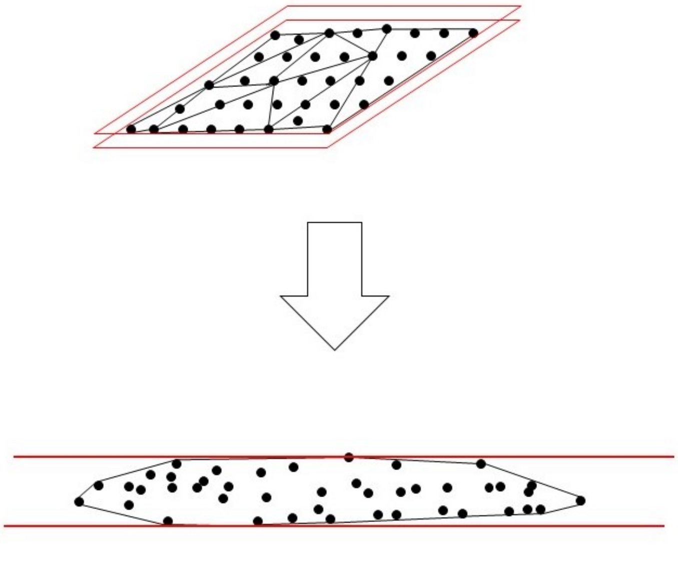

Figure 29: Extracting dimensional values to estimate the tolerance of straightness or flatness in 3D and 2D views.

deviations corresponding to all four tolerances can be extracted from the point cloud, both 6σ and PCR estimation methods could be applied.

The definition of straightness tolerance is given as a tolerance zone within which all the surveyed surface points should lie, as shown in Figure 29. In contrast, the flatness tolerance is defined by two parallel planes that cover the points of the planar feature. Theoretically, straightness refers to the properties of a line; in practice, such a line is ill-defined. Therefore, the evaluation algorithms for both types of tolerances have no significant differences. A convex hull of the plane needs to be computed to access either tolerance via the QuickHull algorithm. Then, the dimensional value is the minimax distance between each facet and the feature points.

5.2.4 Tolerance of Form: Circularity and Cylindricity

Similar to the relationship between straightness and flatness, circularity is defined on a circular profile, while cylindricity considers the 3D volume. Since the actual rotational axis is unknown, the deviations regarding the circularity and cylindricity could be computed similarly by calculating the envelopes for the circular feature discussed in the previous section.

5.2.5 Tolerance of Orientation: Parallelism

Parallelism, perpendicularity, and angularity are three major tolerances defined in both ISO and ASME GD&T standards. Each of these tolerances determines a specific orientation posture of the planar surface with respect to the datums. Algorithms to extract dimensional values from the point cloud are proposed in this section based on the definition of each type of tolerance that can be applied to estimate designed tolerances via 6σ or PCR methods.

Parallelism represents the equidistance condition of the planar surface to its corresponding datum, as shown in Figure 30. According to the standard, the tolerance zone is the minimax distance of two planes parallel to the datum feature and covers all the feature points. Based on the definition, the dimensional value of parallelism x^p for a specific feature can be calculated via

$$x_p = \min_{f \in \mathcal{F}} \max_{i,j \in \mathcal{P}} |d(f,i) - d(f,j)|, \tag{5-6}$$

where $d(f,a)$ is the Euclidean distance between plane f and point a, and $\mathcal{P}$ is the set of points in the feature of interest.

5.2.6 Tolerance of Orientation: Perpendicularity

Perpendicularity represents the ”right-angular” condition between the planar surface and the datum, as shown in Figure 31. The width of the tolerance zone is described by the distance of two parallel planes that are orthogonal to the datum. The points on the surface of interest are first projected to the 2D Euclidean space determined by the datum(s) associated with the feature and the datum that is assumed to be parallel to the feature. The

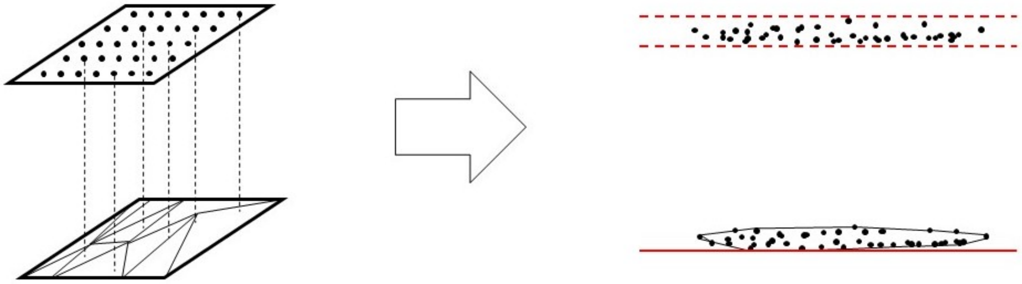

Figure 30: Extracting dimensional values to estimate tolerance of parallelism in 3D and 2D views.

dimensional value is the minimax distance of the points along the axis with respect to the original datum candidate set.

5.2.7 Tolerance of Orientation: Angularity

Perpendicularity is a particular case of angularity, within which the angle between the feature and datum is designed to be a right angle. Therefore, a similar dimensional value extraction algorithm can be applied to find the deviation region. However, unlike perpendicularity, the nominal angle between a feature and its associated datum is unknown in reverse engineering applications. Since the mean-part model proposed in Chapter 4 is an unbiased estimator to the nominal design with a lower variance, the angle value in the mean part model could be an estimator to the unknown design angle. Therefore, the first step is to find the mean part model through several scans of multiple parts. Next, the mean feature landmarks are projected to the 2D Euclidean space determined by the corresponding datums. With the least-squares fitting, the designed angle could be estimated by the angle between the fitted line and the datum.

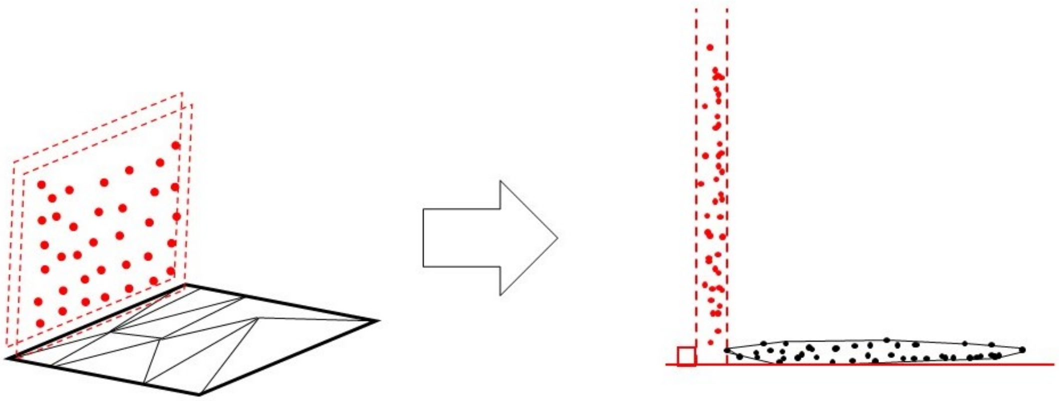

Figure 31: Extracting dimensional values to estimate tolerance of perpendicularity in 3D and 2D views.

Following a similar step as with perpendicularity, the points associated with the feature are projected to the 2D space for each point cloud. The dimensional value of angularity is the minimax distance between the envelope, determined by the angle estimator and the projected points with respect to the datum candidate set.

5.2.8 Tolerance of Location

Locational tolerancing is represented by a zone that constrains the range of an estimated centerline or axis—or center plane. Based on this definition, the primary job of estimating the dimensional value for locational tolerance is to determine the center axis or the center plane. The center axis of the cylindrical feature could be found through the least-squares fitting, as mentioned in the previous section. To infer the center plane, the points on the joint planar features that constrain the planar feature of interest are projected to the corresponding datum. By taking the boundary points on both of the least-squares lines, the center plane becomes the plane that passes the center of the points of both boundaries while remaining perpendicular to the projected plane. For both cases, finding deviation values of locational tolerance can be reduced to the parallelism problem between the center axis or plane and its associated datum.

Table 5: Designed tolerance regions versus the empirical tolerance regions, in inches, estimated by tolerance-inferencing methods based on ASME standard (Feature size/dimensional tolerance).

Tolerancing Feature	True Tolerance	ASME Estimator
Size 1	$(0.185, 0.189)$	$(0.18513, 0.18895)$
Size 2	$(1.489, 1.491)$	$(1.48996, 1.49017)$
Size 3	$(0.549, 0.551)$	$(0.54998, 0.55000)$
Size 4	$(0.374, 0.376)$	$(0.37449, 0.37534)$
Size 5	$(0.989, 0.991)$	$(0.98940, 0.99086)$
Size 6	$(0.989, 0.991)$	$(0.98969, 0.99097)$
Size 7	$(1.874, 1.876)$	$(1.87480, 1.87508)$
Size 8	$(0.374, 0.376)$	$(0.37429, 0.37529)$
Size 9	$(0.249, 0.251)$	$(0.24920, 0.24989)$

5.3 Case Study

We conducted a case study to validate the proposed tolerance estimation method. We estimated the feature tolerances based on a small batch of machine parts and, we then compared our findings with the design tolerance specifications.

The same five mechanical parts, whose design is shown in Figure 24, were collected from MAC as shown in Section 4.3.3. All the dimensions and tolerances are specified in inches, and ASME Y14.5-2009 is used for the GD&T design. Trainees from MAC manufactured the mechanical parts using numerical control machining equipment. According to their design specification, all the parts pass the inspection using a manual CMM. Renishaw Cyclone Touch Probe Scanner was used to survey the surface points for high precision points collection for reverse engineering practice. The point clouds from multi-view were registered and segmented using Geomagic Studio 2014. Since the probe of the CMM cannot accurately survey the points along the sharp edges or near the vertices, the points near the boundaries

Table 6: Empirical tolerance regions, in inches, estimated by different tolerance inferencing methods based on ISO standards (feature size/dimensional tolerance).

Tolerancing Feature	ISO Range Estimator	ISO 6σ Estimator	ISO PCR Estimator
Size 1	$(0.18590, 0.18869)$	$(0.18549, 0.18909)$	$(0.18490, 0.18969)$
Size 2	$(1.48978, 1.49018)$	$(1.48973, 1.49024)$	$(1.48964, 1.49032)$
Size 3	$(0.54999, 0.55000)$	$(0.54999, 0.55000)$	$(0.54999, 0.55000)$
Size 4	$(0.37491, 0.37507)$	$(0.37489, 0.37509)$	$(0.37486, 0.37512)$
Size 5	$(0.98976, 0.99063)$	$(0.98964, 0.99075)$	$(0.98946, 0.99094)$
Size 6	$(0.98985, 0.99079)$	$(0.98972, 0.99092)$	$(0.98952, 0.99112)$
Size 7	$(1.87485, 1.87511)$	$(1.87481, 1.87515)$	$(1.87475, 1.87520)$
Size 8	$(0.37464, 0.37514)$	$(0.37457, 0.37521)$	$(0.37447, 0.37532)$
Size 9	$(0.24932, 0.24959)$	$(0.24911, 0.24982)$	$(0.24899, 0.24994)$

are manually removed from the point clouds. However, for tolerance estimation purposes, the edges and vertices are interpolated through parametric surface-fitting algorithms. Each of the five parts is scanned twice, and the mean-scan configurations are calculated through the DGPPA method proposed in Chapter 3 to represent the accurate point cloud of the parts. The measurement error of the CMM, which is much smaller than the variation between parts, can be roughly estimated by the DGPPA method. Therefore, the measurement error can be ignored in the tolerance estimation study of the original manufacturing processes.

According to Figure 24, nine size tolerances and five geometric tolerances are specified in the original design. Even though the coplanar type of tolerance in the design is under the profile type tolerances that are not discussed in this chapter, both features are planar features, and this tolerance can be solved similarly as the parallelism. In this chapter, our major focus is on the tolerance estimation inconsistent with the ASME standards. As a comparison, the dimensional value extraction methods using ISO philosophy, or the squared loss method, are also presented as a comparison purpose. This method, similar to the skin model shape study [146], is briefly discussed in previous sections. This study extends this

Table 7: The ratio of the design tolerance region "explained" by inferencing tolerance region (feature size/dimensional tolerance). '-' in the table represents the tolerance estimator located outside the designed tolerance.

Tolerancing Feature	ASME Estimator	ISO Range Estimator	ISO 6σ Estimator	ISO PCR Estimator
Size 1	95.50%	69.75%	90.05%	-
Size 2	10.50%	20.00%	25.50%	34.00%
Size 3	1.00%	0.05%	0.05%	0.05%
Size 4	42.50%	8.00%	10.35%	13.00%
Size 5	73.00%	43.50%	55.50%	74.00%
Size 6	64.00%	47.00%	60.00%	80.00%
Size 7	14.00%	13.00%	17.00%	22.50%
Size 8	50.00%	25.00%	32.00%	42.50%
Size 9	34.50%	13.50%	17.75%	23.75%

method to the tolerance estimation methods by incorporating manufacturing processes and inspection knowledge. The estimated tolerances for both classes using methods proposed in this chapter are represented in Tables 5 and 6 for size tolerances, and Table 8 for geometric tolerances. Since the original tolerance is known, the ratios between the estimated tolerance widths and the original tolerance widths are illustrated in Table 7 and Table 9 for comparative purposes.

5.3.1 Discussion

In the case study, the results of size tolerances based on ASME and ISO standards are presented. As discussed in the previous section, ASME Y14.5-2009 is a "hard-gauge" standard sensitive to the outliers, while ISO standards are more robust since least squares are often implemented for dimension extraction. This phenomenon is verified in Table 1. Com-

Table 8: True tolerance regions versus the empirical tolerance regions, in inches, estimated by different tolerance inferencing methods (datum-related tolerance).

Tolerance Type	True Tolerance	Range Estimator	6σ Estimator	PCI Estimator
Perp 1	0.001	8.6568×10^{-5}	1.0959×10^{-4}	1.4575×10^{-4}
Perp 2	0.001	3.6724×10^{-4}	5.305×10^{-4}	3.989×10^{-4}
Coplanar	0.001	6.1425×10^{-4}	9.0126×10^{-4}	0.00120
Angular	0.010	0.00847	0.00956	0.01005
Location	0.003	0.00233	0.00232	0.00309

pared to the range tolerance estimations, the ranges based on ISO standards are universally narrower than the ASME estimated ranges. The least-squares are more robust to the outliers than the range statistics. With a small sample size, the least-squares fitted values have relatively lower variance and centering around the mean. Moreover, in actual practice, the 6σ policy or PCR policy is often implemented to control the manufacturing process based on ISO standards. With the assumption on both 6σ or PCR policies, the estimated ranges are close to the performance of the ASME method. However, since the parts are manufactured by trainees and inspection is conducted under ASME GD&T specification, some of the PCR-based estimators are outside the designed tolerance range. Therefore, if the parts can be assumed to be produced under ASME Y14.5-2009, the ASME-based estimator could perform better by conservatively providing a wider tolerance region. However, if the parts are produced under the ISO standards, the PCR-based estimators could provide a wider tolerance region to reduce production costs. More importantly, this framework provides an opportunity for the AM processes, which usually create parts with more significant variations, to re-manufacture the legacy parts with acceptable quality.

Since the dimensional values or deviations in the geometric tolerances can be directly extracted from the point cloud, both the 6σ method and the PCR method provide a wider empirical tolerance range than the range method. Because the parts are not produced by a manufacturing vendor, the process is not under statistical control. The major assumptions

Table 9: The ratio of the designed tolerance region "explained" by inferencing tolerance region (datum related tolerance). '-' in the table represents the tolerance estimator located outside the designed tolerance.

Tolerance Type	Range Estimator	6σ Estimator	PCI Estimator
Perp 1	8.66%	10.96%	14.56%
Perp 2	36.72%	53.05%	39.89%
Coplanar	61.43%	90.13%	-
Angular	84.7%	95.6%	-
Position	77.67%	77.33%	-

for the PCR method are violated, which makes most of its estimations invalid. In this case, empirical tolerances estimated by the 6σ method are more conservative than those for the PCR method and broader compared to those for the range estimator. However, the tolerances estimated by the PCR method are closer to the true tolerance in terms of value. Even though the estimated tolerances are a little wider than the designed ones, their differences are almost negligible. Therefore, the PCR method is still a better choice when our objective is to reduce reproduction cost and provide products with acceptable quality, while the reproduced products using the 6σ method are of higher quality.

5.4 Summary and Conclusions

Re-manufacturing has attracted increasing research interest because of its sustainability. This chapter introduces a toolset to complete the tolerance information for re-manufacturing systems when the original design is missing or inaccessible, as shown in Figure 32. This toolset estimates the tolerance design using the knowledge of production system control and inspection. Both ASME's and ISO's GD&T standards are considered for tolerance estimation. Furthermore, algorithms are developed to transform the point clouds to the

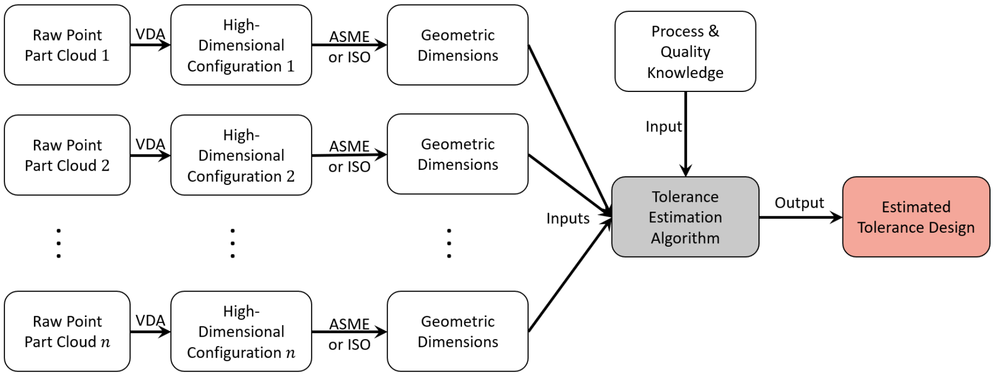

Figure 32: Process map of the tolerance estimation algorithm presented in Chapter 5.

specific dimensional values according to the standards. This toolset can be directly applied to re-manufacturing applications for legacy parts or spare parts reproduction process planning and inspection. The proposed methods are validated and evaluated through a case study of genuine machined parts. The empirical tolerance regions for different tolerancing types are close to the designed region.

AM is often used in the re-manufacturing system because of its flexibility and cost-saving for small-batch reproduction. The layer-by-layer fabrication nature makes the metrology method of AM drastically different from the traditional way. The algorithm for extracting dimensional values can inspect the AM-created parts for inspection and quality assurance.

However, since the primary objective of the presented work focuses on tolerance estimation for RE applications, algorithms for dimensional value extraction are not thorough. Specifically, we concentrate on tolerances regarding planar and cylindrical features; in our future work, we will consider other tolerancing types, such as profile and runout tolerances, which are also important. Furthermore, as shown in Section 5.1, current methodologies heavily rely on the normality assumption. However, the current-state-of-the-art nonparametric methods cannot be directly applied to our study since only a few parts are available in RE practices. One of the potential solutions is incorporating engineering knowledge into the nonparametric methodologies to speed up its convergence or relax these requirements using Bayesian methods.

6.0 Automated Variance Modeling for 3D Point Cloud

In Chapters 4 and 5, we address the process-planning problem in RE and discuss the methodologies to complete the tolerance information for RE-embedded re-manufacturing. We further observe that the variational behavior of the 3D scanners plays a critical role in both studies. Specifically, the accuracy of the prior information, or the variance of the scanner, in the Bayesian modeling determines the performance for process planning. In the tolerance estimation method, the scanning variance heavily influences the estimated width of the tolerance region. This chapter proposes an automated variance modeling procedure to predict the landmark variances based on geometric features. In Section 6.2, we first discuss the selection of geometric inputs for our automated variance prediction algorithm and procedures that transform the raw-point clouds to these inputs. In Sections 6.3 and 6.4, we present our algorithm in detail, including the components and structures of the Bayesian extreme learning machine (BELM) and the metric for the scanning history that we recommend to select an appropriate object from previous multiple scan experiments to achieve better predictive performance. Our case study is in Section 6.5. We conclude this chapter with remarks and a preview of future research directions in Section 6.6. Similar to Chapter 5, the presented variance modeling methodology plays two roles in this dissertation. It can be an independent algorithm for analysis and modeling the variational behavior of a targeting scanner. It can also complement the RE process-planning algorithm presented in Chapter 4 to learn and model the prior information regarding the 3D scanner. The remainder of this chapter appears in [59].

6.1 Introduction

From the RE and metrology perspectives, it is critical to perform statistical inferences on point-cloud data to model the variation in the deviations of the data from initial designs. Several challenges arise in RE and metrological analysis for AM due to the flexible design features and complex shapes inherent in the freeform objects of interest for these technologies. Two important challenges are (1) that existing analytical methods and metrology tools cannot provide detailed descriptions of objects of interest and (2) that they can be time-consuming. Methods such as measurement system analysis (MSA) [152] and gauge R&R [164, 115] studies analyze point-cloud data by modeling them as univariate or multivariate random variables; these methods are designed for data collected via classical metrology tools, such as manual coordinate measuring machines or gauges. These methods and tools are suitable for traditional manufacturing systems, in which constraints in design software often impose restrictions for a product design and manufacturing hardware [135]. One example of a product design restriction, which arises due to constraints in computational and visual capabilities [168], is introduced by using the primitive features involved in classical CAD packages. Traditional manufacturing processes can typically only produce such primitive features, and at best, can fabricate an approximation of freeform shapes via complex path planning [102]. The resulting metrology or inspection techniques for the fabricated products usually focus on accurately measuring shape dimensions through either a small number of points on the product or parametric fitting. However, these tools are not appropriate for the objects or designs of interest in RE and AM because their shapes (especially for freeform products) are not fully described or measured in this manner. In addition, since nearly all outer surfaces of additively manufactured parts are composed of the boundaries of a stack of layers of material, if only a small number of points are measured, then the measurements would provide an incomplete description of the products. Fast non-contact scanning techniques such as laser scanner [149] and photogrammetry [136] technologies have recently been developed to enable the rapid extraction of geometric information on objects. In contrast to the previously described classical tools, these non-contact techniques usually survey many points and construct point-cloud data in less time [13]. However, the complex structure and high volume of such data make the direct application of classical MSA and Gauge R&R techniques difficult. Variance modeling of point-cloud data remains an important issue for such applications as repetitive metrology design [24] and RE process planning in Chapter 4.

Recently developed approaches for RE and metrology analysis for AM do not satisfactorily address the previously described challenge. Wang and Tsung [171] developed a Bayesian generative modeling technique to address the calibration problem for a low-resolution scanner, considering both variance and bias for the scanner. However, their study focused only on the deviations and randomness of in-plane, or 2D, scanning profiles in the x-y plane, whereas variations in the z direction can be more severe in practice [41, 145]. Furthermore, their method highlighted the calibration of a specific shape profile based on a high-resolution system, while the application of the calibration model to other shapes of interest may require involved shape approximation methods [73]. Del Castillo et al. [41] modeled the point-cloud data of features using a geodesic Gaussian process that can account for pointwise randomness. However, the objective of their model was on surface fitting, not variance modeling. There is a significant trade-off between the number of initiation scans and the analytical performance of the variance estimator under their method.

An essential requirement for specifying variance models for point-cloud data is categorizing sources of variations. Point-cloud data incorporate three sources of information: objects of interest, scanner hardware, and measurement environment. Previous research primarily focused on noise arising from the hardware and measurement environments [62]. However, any data point is generated through interactions between the scanner and the object, in addition to the environment. For example, in laser scanning, the points received on the detector come from the laser source via reflection on the surface of the object [55], so that the variance of the surveyed point is strongly related to the object. The above three sources of information involve many distinct factors. Examples of such factors for a laser scanner appear in Figure 33. Some of these factors are usually controlled for metrology practices (e.g., environment and scanner hardware factors), whereas others are usually identical or similar for the same application purposes or AM processes (e.g., materials and colors). Creehan and Bidanda [37] conducted a fractional factorial experiment to investigate various RE settings (in terms of both hardware and software) and identified settings for optimum point-cloud data quality. One of the critical factors they identified is orientation, which essentially describes the impact of geometric shape on point-cloud variance. Ultimately, the geometric design and position of an object of interest relative to the scanner are two critical factors in variance modeling.

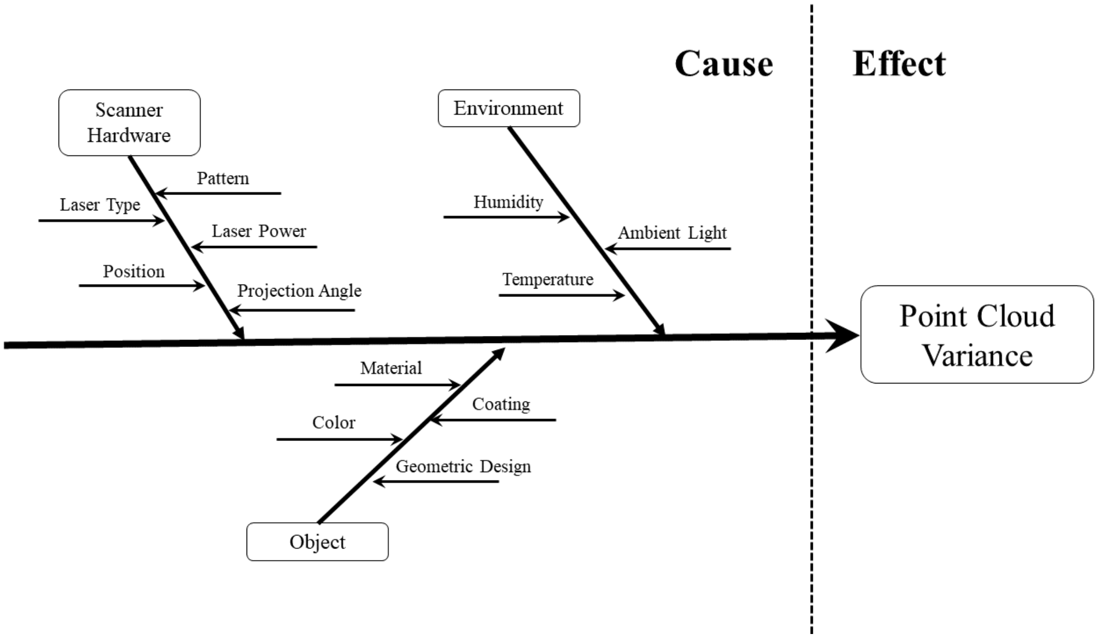

Figure 33: Fishbone diagram of a sample of factors related to the measured objects, scanning hardware, and environments that could influence the variance of a laser scanner.

We develop an algorithm for modeling the variance of point-cloud data based on a scanning history. Our algorithm utilizes the VDA framework to process point-cloud data for variance modeling. Two essential factors utilized in our algorithm are object shape designs and the interaction of object surface and the light source. Our algorithm is efficiently trained on high volume point-cloud data via a combination of Bayesian extreme learning machines (BELM) [48, 71] and a new empirical Kullback-Leibler divergence we developed to select the training set for the BELMs according to the scanning history of those objects that are geometrically similar to the object of interest. Moreover, two novel structural variants, ensemble- and residual-BELMs, are proposed to improve the prediction performance of the BELM algorithm. Significant applications of this algorithm include repetitive metrology design and RE process planning, and are illustrated by a case study that we conduct on variance modeling for additively-manufactured products.

6.2 Variance Modeling Algorithm

6.2.1 Components of the Algorithm

Our variance modeling algorithm consists of three essential components. First is the specification of the geometric features that can be used to model landmark variance and extraction of these features from point-cloud data. The second is the use of BELMs to model the relationships between the geometric features and landmark variances. The third is our new empirical Kullback-Leibler divergence for selecting a scanning history to train BELMs and yield improved variance predictions for objects of interest. Details on these components are provided in the remainder of this chapter.

6.2.2 Geometric Features for Landmarks

The variance of each point on an object is strongly affected by the object's geometric features and its interactions with the light source or ambient light. Although parts can range across an infinite variety of designs in principle, the nature of non-contact scanners implies that only local geometric information affects the variance of a point on a part. In the specific case of a laser scanner, the shape of the local area in which the laser is projected significantly impacts the variability of the extracted point coordinates. The randomness corresponds to the basic mechanism of a general laser scanner for inferring the coordinates of a point on the object surface by receiving the reflection of the laser strip projected on the camera receiver (Figure 34). The Law of Reflection states that the angle of incidence θ_i should equal the angle of reflection θ_r [130]. Therefore, if the incident laser is nearly orthogonal to the normal direction for a point, it becomes difficult to capture its reflection by the camera, increasing the measurement variance. Furthermore, it is difficult to accurately measure high curvature points via the laser stripe. The reason is that high curvature points are generally located in small regions that are difficult to capture by the laser strips; also, the tangent planes and normals of these points are relatively more sensitive to noise due to the high curvature.

To account for each landmark's local shape information for modeling variance, we include predictor variables that capture the local geometric features of the normal direction and

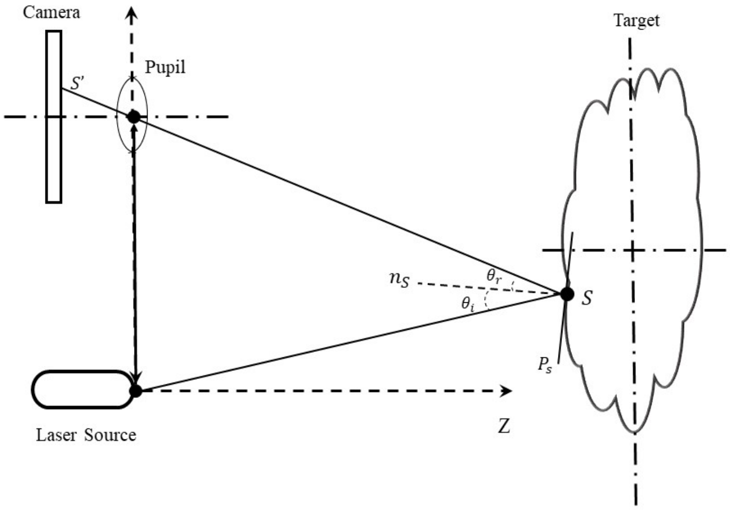

Figure 34: Mechanism of a laser scanner with a single laser strip. Here, P_S is the tangent plane of the surface at point S, and n_S indicates the normal direction. The incident angle θ_i equals the reflection angle θ_r.

curvature for each point. These variables can be found in CAD models. However, RE and metrology are highly object-dependent, and the combination of the lack of CAD models and the presence of local deviations on the parts can be problematic. Therefore, we first need to estimate these part-specific local geometric predictor variables in our algorithm. We proceed to describe the normal direction and curvature variables in more detail.

Two characteristics of the 3D normal direction vector—the angle θ between it and the z-axis and the normal of the scanning platform—directly impact scanning variability. As such, we incorporate only these two characteristics of the normal direction into variance models. The direction of the normal affects the incidence and reflection directions of the light source. As we assume the object is fixed on the scanning platform, the z-axis of the platform corresponds to the vector $(0, 0, 1)$. If a large angle exists between the point's normal direction vector and the z-axis, then capturing the point will be difficult, and its variance should be large. Alternatively, if a small angle exists between the normal direction vector and the z-axis, then capturing the point will be easier, and its variance should be small. RE or metrology software typically provides information on the normal of the screening platform in their output files. However, this information may not be sufficient for modeling variance in our context because the landmarks we consider are actively generated, and they may not correspond to landmarks in the original point-cloud data. Also, the normal direction predetermined by the scanner is usually facing either into or out of the material; hence, it may not differentiate between convex and concave features. For these reasons, the normal directions for the landmarks must still be estimated. In our algorithm, we infer the normal direction for each landmark by performing a PCA on its neighboring points selected using the fixed-radius nearest neighbors algorithm [138]. We recognize that the estimation problem is equivalent to inferring the normal of a plane tangent to the surface at the given point and that the tangent plane can be approximated via the least-squares fitting of the neighboring points. The accuracy of the approximated normal is closely related to the area of the neighborhood, with smaller areas providing more accurate estimation in general. The raw-point cloud data usually possess high-point density compared to the landmarks generated based on the grid structure, so we utilized the raw-point cloud data to estimate the normal directions. This estimation is accomplished by first calculating for each landmark i the 3×3 local covariance matrix $C_i = ||\Omega_i||_0^{-1} \sum_{\{j: p_j \in \Omega_i\}} (p_j - \bar{p}_i)(p_j - \bar{p}_i)^\intercal$, where Ω_i is the neighborhood of landmark i, the $p_j \in \mathbb{R}^3$ are from the raw-point cloud data, and $\bar{p}_i$ is the centroid for points in Ω_i. After C_i is calculated, we then obtain all of its eigenvalues $\lambda_{1i} \geq \lambda_{2i} \geq \lambda_{3i}$, and the corresponding eigenvectors w_{1i}, w_{2i}, w_{3i}. Finally, w_{1i} and w_{2i} determine the tangent plane, and w_{3i} is the estimate of the normal direction vector for landmark i.

Curvature is a geometric measure that describes how much a curve or surface deviates from a line or a plane, respectively. Variables based on curvature are widely used in RE and computer vision for registration and segmentation due to their robustness to noise, and translational and rotational invariances [53, 5]. Because we only consider discretized points, in this article, "curvature" refers to the curvature of a curve at a point. For illustrative curvatures in 2D, we note that the curvature of any point on a circle is the reciprocal of its radius, the curvature of a point on a straight line is zero, and the curvature of the intersection point for two lines is infinite. Curvature is not uniquely defined in 3D because infinitely many curves can pass through a point on a surface. Two commonly used curvature measures in 3D are the Gaussian and the mean curvatures, defined respectively as $G = \kappa_1\kappa_2$ and $H = (\kappa_1 + \kappa_2)/2$ in terms of the maximum and minimum values of all the curvatures as denoted by κ_1 and κ_2, respectively. Estimation of Gaussian and mean curvatures yields information on a local surface containing the surface change in a small region but not on an individual point. Therefore, we utilize the rate of the local curvature change ν_i for each landmark i in our algorithm, where this quantity is defined as $\nu_i = \lambda_{3i}/(\lambda_{1i} + \lambda_{2i} + \lambda_{3i})$ in terms of the previously defined eigenvalues.

6.3 Variance Modeling via Bayesian Extreme Learning Machines

Our models for the relationships between variances and predictor variables that capture local geometric features for landmarks in point cloud data are of the general form

$$t_{ij} = f_j(\cos(\theta_i), \nu_i) + \epsilon_{ij}, \tag{6-1}$$

where $i = 1, \ldots, k$ is the index for landmarks, $j \in \{x, y, z\}$ indicates whether the x-, y-, or z-coordinate is under consideration, $t_{ij} = \log(\sigma_{ij}^2)$ is the outcome variable that corresponds to the logarithmic transformation of the variance for coordinate j of landmark i, θ_i is the angle between the normal direction vector of landmark i and the z-axis, ν_i is the rate of the local curvature change of landmark i, and the error terms ϵ_{ij} are independent $\mathrm{N}(0, \tau^2)$ random variables. To fit such a model, we enter an estimate of σ_{ij}^2 obtained from the point-cloud data into equation (6-1). Specifying regression models for the f_j can be difficult in general. Flexible classes of models, such as Gaussian processes or neural networks, can instead be used to model complex trends in the f_j [93]. However, the high volume of landmarks results in standard implementations of these models incurring the prohibitive computational time and costs [173]. Hence, we utilize BELMs—a class of single-hidden layer feedforward neural networks (SLFNs)—to model the f_j (Figure 35). Bayesian extreme learning machines are universal approximators [71], and their predictive performances have been demonstrated to

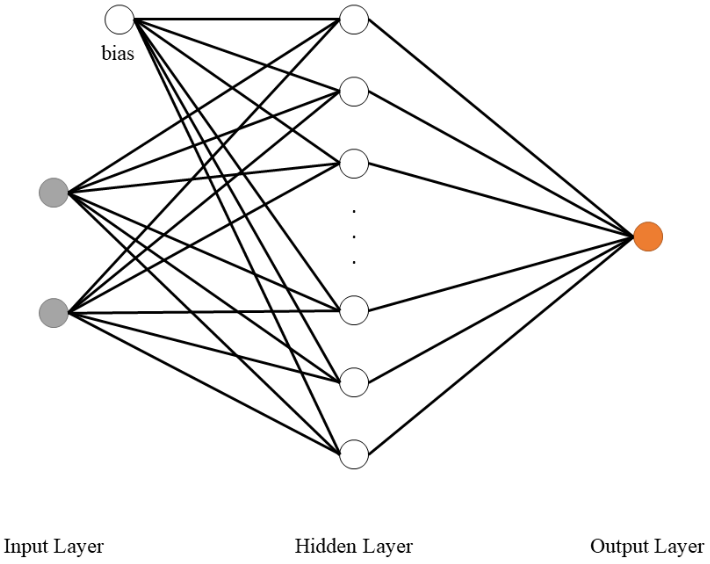

Figure 35: An example of the structure of a standard SLFN.

be comparable to those of Gaussian processes and neural networks [71, 72, 153]. These facts accordingly motivate our choice of BELMs to model variance. Further details on our BELMs are presented below.

Extreme learning machines (ELMs) were developed by [71] to increase the learning speed of SLFNs. In contrast to standard neural networks and their traditionally slow and iterative gradient-based learning algorithms, in an ELM, the input weights for the SLFN are randomly assigned, and the fitting process is performed only on the output weights. To formally describe this, let $y_i \in \mathbb{R}$ be the outcome and $x_i \in \mathbb{R}^p$ be the vector containing the values of p predictors for observation $i = 1, 2, \ldots, n$. Then the ELM model with m hidden neurons is

$$y_i = \sum_{q=1}^{m} \beta_q \; g(\omega_{0q} + x_i^\mathsf{T} \omega_q) + \epsilon_i, \tag{6-2}$$

where the errors terms ϵ_i are independent $\mathrm{N}(0, \tau^2)$ random variables, $\omega_{0q} \in \mathbb{R}$ and $\omega_q \in \mathbb{R}^p$ are the random intercept weight and the random vector of input weights, respectively, for neuron q, β_q is the output weight for neuron q that is to be inferred from the data, and the function $g : \mathbb{R} \to \mathbb{R}$ is the activation function. The random input weights are drawn from either the $\mathrm{Uniform}(-1, 1)$ or the standard $\mathrm{N}(0, 1)$ distributions. Many activation functions can be utilized, such as the sigmoid function, rectified linear unit, and radial basis functions [65]. We adopt the hyperbolic tangent function $g(x) = (e^x - e^{-x})/(e^x + e^{-x})$ in our algorithm. In general, ELMs possess an advantage over traditional neural networks in that they reduce computational costs and identifiability issues through the random assignment of input weights and instead focus on output weights. They are fitted according to a linear regression model on the outcome values and (random) hidden neurons, and they possess an additional advantage of enjoying the computational time of linear regression. An ELM is a universal approximator; with a sufficiently large number of hidden neurons, it can learn complex functional forms with similar predictive performances as other neural networks [72].

A disadvantage of ELMs that arises from their random assignment of input weights is the potentially high probability of saturation of hidden neurons. Saturation here refers to the activation function for a hidden neuron returning a relatively constant value for a range of inputs [48]. Multicollinearity among the random neurons will arise in the case of saturation, which results in increased prediction variance. Saturation in ELMs can be mitigated by fitting BELMs instead—specifically, by placing normal priors on the output weights β_q and fitting the corresponding Bayesian model. This BELM, which also corresponds to Bayesian ridge regression, effectively shrinks the output weights for the saturated neurons. [48] proposed a new class of BELMs that involve tuning the bounds of the uniform distributions for the input weights to further improve upon standard BELMs in terms of eliminating saturation issues. In this new class of BELMs, the input weights are sampled to yield a high probability that the input values of the activation functions are in the unsaturated region (e.g., in the interval $(-2.5, 2.5)$ for the hyperbolic tangent activation function). We accomplish this tuning by sampling the intercepts ω_{0q} from $\mathrm{Uniform}(-1, 1)$ sampling each random weight ω_{jq} from the $\mathrm{Uniform}(-5\alpha_j/(2\mathrm{max}_j), 5\alpha_j/(2\mathrm{max}_j))$ distribution, where $\alpha_j = \mathrm{sd}_j/(\sum_{l=1}^{p} \mathrm{sd}_l)$, with sd_j denoting the standard deviation of the values of predictor j and max_j denoting the maximum absolute value of predictor j.

Thus, similar to the work of [48], our algorithm utilizes a BELM with the previously described scaled sampling strategy for the input weights to model the relationships between the local geometric features and the variances for landmarks in point-cloud data. For each landmark $i = 1, \ldots, k$, we let $x_i = (\cos(\theta_i), \nu_i)$ denote its predictors as in equation (6-1). For each hidden neuron $q = 1, 2, \ldots, m$, we draw the input weights ω_{0q} and ω_q based on our scaled sampling strategy. We let H be the $k \times m$ matrix whose (i, q) entry is $g(\omega_{0q} + x_i^\mathsf{T}\omega_q)$. Our variance model is then

$$t_j = H\beta + \epsilon_j, \tag{6-3}$$

where $t_j = (t_{1j}, \ldots, t_{kj})$ is the vector of the natural logarithms of the landmark variances for coordinate $j \in \{x, y, z\}$, $\beta \in \mathbb{R}^m$ is the vector of output weights that are to be inferred, and ϵ_j is the vector of error terms that are independent and identically distributed $\mathrm{N}(0, \tau^2)$ random variables with unknown variance τ^2. Our prior probability density function on the unknown parameters is $p(\beta, \tau^2 \mid \eta^2) \propto \tau^{-2}\eta^{-m}\exp\{-\beta^\mathsf{T}\beta/(2\eta^2)\}$, and our hyperprior distribution on η^2 is the Inverse-Gamma density $p(\eta^2) \propto \eta^{-6}\exp(-0.01\eta^{-2})$. The joint posterior distribution of the unknown parameters can be calculated in a straightforward manner using a Gibbs sampling algorithm [54].

However, the performance of the BELM is constrained by its simple structure. The complex nonlinear relationship between the outcome and predictors can be hard to model due to the single-layer structure. Inspired by machine learning algorithms, we propose two structural variants of the BELM model to improve nonlinear approximation performance and lower the prediction variance.

6.3.1 Ensemble Bayesian Extreme Learning Machine

Ensemble methods are machine learning algorithms that integrate multiple learning models to have better predict performance than single ones. For example, the random forests algorithm combines many decision trees with a small number of branches, which reduces the overfitting of the decision trees and provides more accurate predictions [19]. With a similar spirit, we propose an ensemble version of the BELM, named ensemble Bayesian extreme learning machine (E-BELM), which is shown in Figure 36. The primary reason to utilize the ensemble method is to enhance the accuracy of predictive performance. Since the BELM is a "black-box" model, the model can be easily overfitted, within which the input weights are

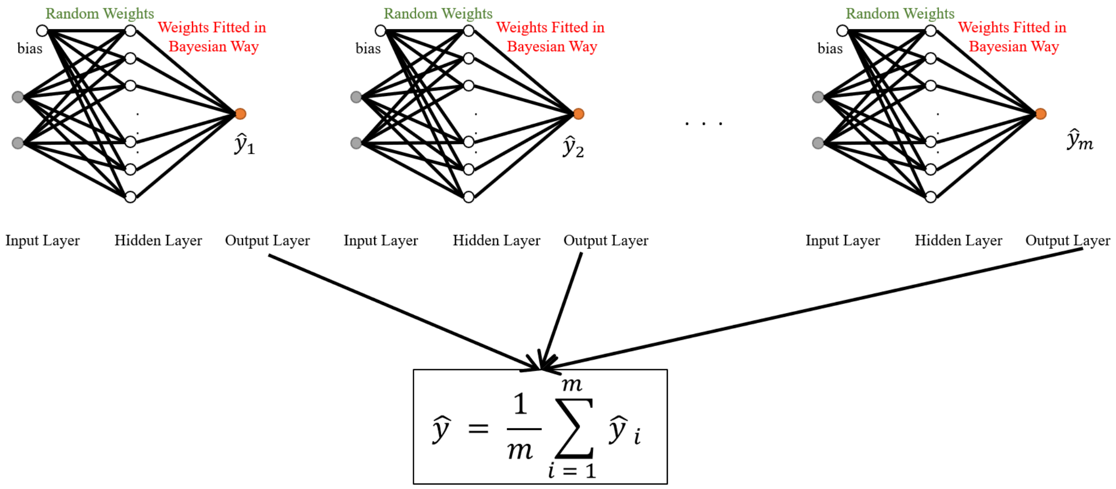

Figure 36: An example of the structure of an E-BELM.

randomly assigned. Using the ensemble method, much smaller BELMs with a small number of hidden layers are trained, which tend to be less overfitted, and the predictions are the combined effect of all the BELMs with relatively smaller variance.

6.3.2 Residual Bayesian Extreme Learning Machine

Another way to improve the BELM algorithm is to build a sequence of models—residual Bayesian extreme learning machine (Res-BELM)—as a generalized additive model, shown in Figure 37. The BELM models are stacked up and trained sequentially. The response values utilized for training each set of models are the residuals from previously trained models. That is, for the ith BELM model, the training response values are $\mathbf{y} - \sum_{j=1}^{i-1} \hat{\mathbf{y}}_j$, where $\mathbf{y} = \{y_1, y_2, \ldots, y_n\}$ is the observed outcomes and $\hat{\mathbf{y}}_j$ is the predictions of the jth BELM model. The Bayesian setup of the BELM provides a ridge effect to mitigate overfitting for a single BELM; however, it also deteriorates the model performance because of the randomly assigned input layer. Res-BELM adds multiple Bayesian neural networks to fit different patterns instead of increasing the number of hidden nodes, which prevents overfitting for any of the models and increases overall predictive performance.

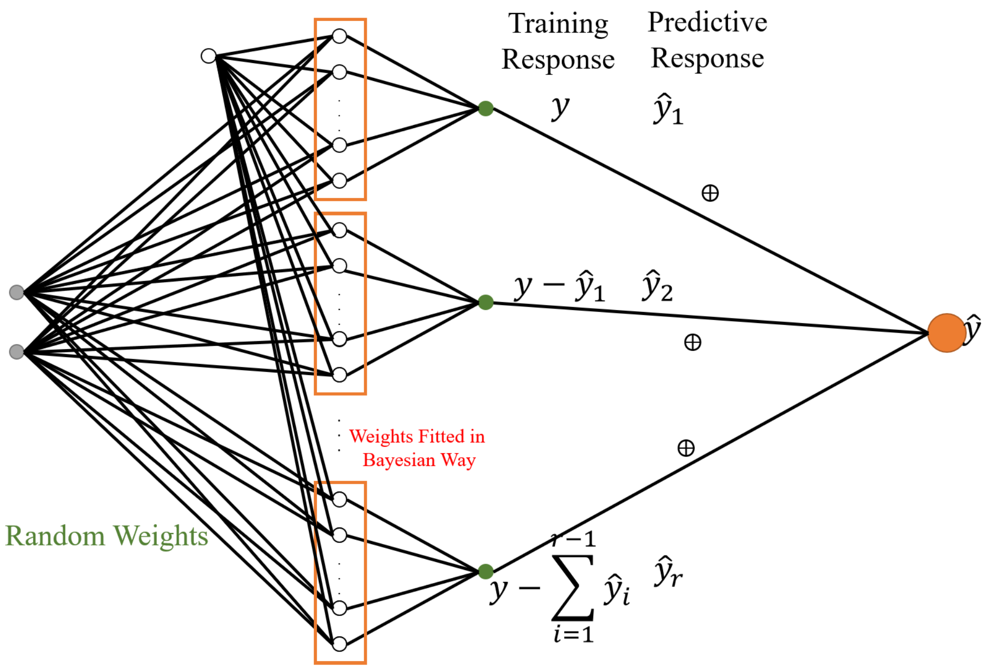

Figure 37: An example of the structure of an Res-BELM.

Two BELM architectures, E-BELM and Res-BELM, are proposed based on two different points of view to solve different issues: E-BELM is based on the ensemble method to prevent overfitting; Res-BELM is based on the idea of generalized additive models to improve the fitting performance. However, they share a common idea—integrating multiple BELMs to provide predictions. Each of these two architectures has different sets of hyper-parameters, e.g., the number of ensemble samples for the E-BELM and the number of stack-up models in the Res-BELM. These hyper-parameters for both architectures can be determined using cross-validation methods [49].

6.4 Selection of Scanning History for Training Variance Model

Multiple scans of objects must be performed to form the training data for a BELM variance model. In general, the scanning history should satisfy three conditions: (1) the scanner hardware is fixed, (2) the metrology environment is under control, and (3) the previous parts' materials and colors are similar. Dedicated and independent scanning trials could be conducted, or previously recorded scans of the same objects could be used for the training data, so long as the above three conditions are satisfied. An important issue that arises from the availability of multiple scanning records is selecting an appropriate scanning history to improve landmark variance predictions for an object of interest. If the training data and the object have similar joint distributions of the geometric features (e.g., if the scanning history is geometrically similar to the target object), we expect the variance model to yield a good predictive performance. Also, as a BELM's random selection of input weights can result in interpolation and extrapolation issues if the scanning history is missing geometric feature values that appear in the object of interest, then the variance prediction can be adversely affected.

Our algorithm selects a scanning history by a measure that compares the distributions of two random variables. Two common measures that have previously been utilized for this purpose are Wasserstein distance [167] and Kullback-Leibler (KL) divergence [45]. The first focuses on the similarity in the "shapes" of two distributions and is not sensitive to the missing parameter regions. KL divergence from distribution Q to P is defined as $D_{\mathrm{KL}}(P \mid\mid Q) = \sum_{x \in \Theta} P(x) \log\{P(x)/Q(x)\}$, where Θ is their shared parameter space. In our context, P is the distribution of the geometric features for previous parts in the scanning history, and Q is the distribution of the geometric features for the target part. In this definition, $Q(x) = 0$ always implies $P(x) = 0$ for any $x \in \Theta$. Moreover, if $P(x) = 0$, the contribution of this term is trivial because $\lim_{z \to 0^+} z \log(z) = 0$, where z represents the distribution function of P. Therefore, KL divergence is not sensitive to missing values in the distribution Q. Our algorithm measures the discrepancy between the geometric feature spaces of a scanning history and an object of interest using an empirical KL divergence with a penalty on missing values. In contrast to the classic application of KL divergence, in which parametric distributions are assumed in advance for both P and Q, the densities of the predictors need to be estimated in our setting. Histograms and kernel density estimators constitute two widely used density estimation methods. Although kernel density estimators provide favorable properties (e.g., smoothness and continuity), in our context, the

KL divergence must be integrated over the feature space, which is computationally difficult. Histograms are much easier to compute and implement, so we utilize them to calculate our empirical KL divergence.

The implementation of our method proceeds via three steps. First, for each of the two geometric features, the predictor values range is separated into l bins. Second, the empirical distributions of the two geometric features are captured by the frequency of the number of values located in each of the l^2 bins. Finally, the empirical KL divergence for variance prediction is calculated as

$$MD_{\mathrm{KL}}(P \mid\mid Q) = \sum_{\{x \in \Theta\} \cap \{x : Q(x) \neq 0\}} \left[P(x) \log \left\{ \frac{P(x)}{Q(x)} \right\} \mathbb{I}\{P(x) \neq 0\} + \psi(Q(x)) \mathbb{I}\{P(x) \neq 0\} \right], \tag{6-4}$$

where Θ is the set containing all l^2 bins, $\mathbb{I}(\cdot)$ is the indicator function, P and Q are the histograms of the predictor variables in the scanning history and the target object, respectively, and $\psi(Q(x))$ is the penalty function with respect to the density of $Q(x)$. The penalty function in equation (6-4) should be selected to satisfy the following three conditions: (1) when $Q(x) = 0$, the penalty $\psi(Q(x)) = 0$; (2) the penalty function ψ should be a monotone decreasing with respect to the density of Q; and (3) the supremum of $\psi(Q(x))$ should be less than or equal to the infimum of other values that contribute to the KL divergence in the parameter space, i.e.,

$$\sup_{\{x \in \Theta\} \cap \{x : Q(x) \neq 0 \cap P(x) \neq 0\}} \psi(Q(x)) \leq \inf_{\{x \in \Theta\} \cap \{x : Q(x) \neq 0 \cap P(x) \neq 0\}} P(x) \log \left\{ \frac{P(x)}{Q(x)} \right\}. \tag{6-5}$$

The first two conditions are straightforward to interpret and justify. The third condition and equation (6-4) ensure that the penalty values will not be overwhelmed by the other values. A straightforward example of a penalty function that satisfies all three conditions is the linear penalty function $\psi(Q(x)) = s\ Q(x)$, where $s \in \mathbb{R}$ is a fixed value chosen according to the third condition. If $MD_{\mathrm{KL}}(P \mid\mid Q)$ is close to zero in this case, then the scanning history has a predictor distribution close to the object of interest and, therefore, is recommended for training the BELM models. Also, if $MD_{\mathrm{KL}}(P \mid\mid Q)$ is far from 0, then the scanning history may have some missing predictor values compared to the target object, and thus is not recommended for training the BELM models.

In practice, we also recommend that the number of bins for the modified empirical KL divergence be chosen as $\underset{l}{\operatorname{argmax}} |MD_{\mathrm{KL}}(P^l \mid\mid Q_1^l) - MD_{KL}(P^l \mid\mid Q_2^l)|$, where Q_1^l and Q_2^l are the predictors' histograms of two training objects with l bins, and P^l is the histogram of the test object. This problem can be solved by screening a range of bin numbers.

6.5 Case Study of Variance Modeling for Additive Manufacturing Point Cloud Data

Our case study of the variance modeling algorithm involves a freeform additively manufactured object and different scanning histories, with four total additively-manufactured products considered (Figure 38). All four products were created by LulzBot TAZ 3D printer (Figure 22(b)) that utilized a gold metallic 2.85 mm polymer. The freeform object with two hills and one valley in the right panel of Figure 38 is the test object, which we refer to as "Test." The half-ball shape (referred to as "Half Ball"), the freeform with only one hill (referred to as "Freeform 1"), and the freeform with two hills that are flatter than those in Test and one valley (referred to as "Freeform 2") constitute the entire scanning history. Each of the four objects is scanned 30 times using one FARO Platinum 8' Arm Laser Scanner (Figure 22(a)) to obtain the landmarks' variances. A 0.5 mm thin plate is incorporated in each CAD model to remove noise from printing and scanning. The multiple scans yield variance estimates (i.e., sample variances) for the landmarks' coordinates, and these estimates are taken as the outcomes. The distributions of the coordinate variances of each object are shown in Figure 39, 40, 41, and 42.

We generate the objects' landmarks by the supporting plane version of F-CPP. Approximately $30,000$-$50,000$ landmarks are generated for each object. The objects' configurations are aligned by the registration of the landmarks' projections onto the supporting plane. We then calculate the variances for each landmark's coordinates. To extract the landmarks' geometric features, we utilize the original point cloud to train the fixed-radius nearest neighbors algorithm and apply the local PCA to the landmarks' neighbors to approximate the normal vectors and curvature change rates, as described in Section 6.2.2. This same procedure was

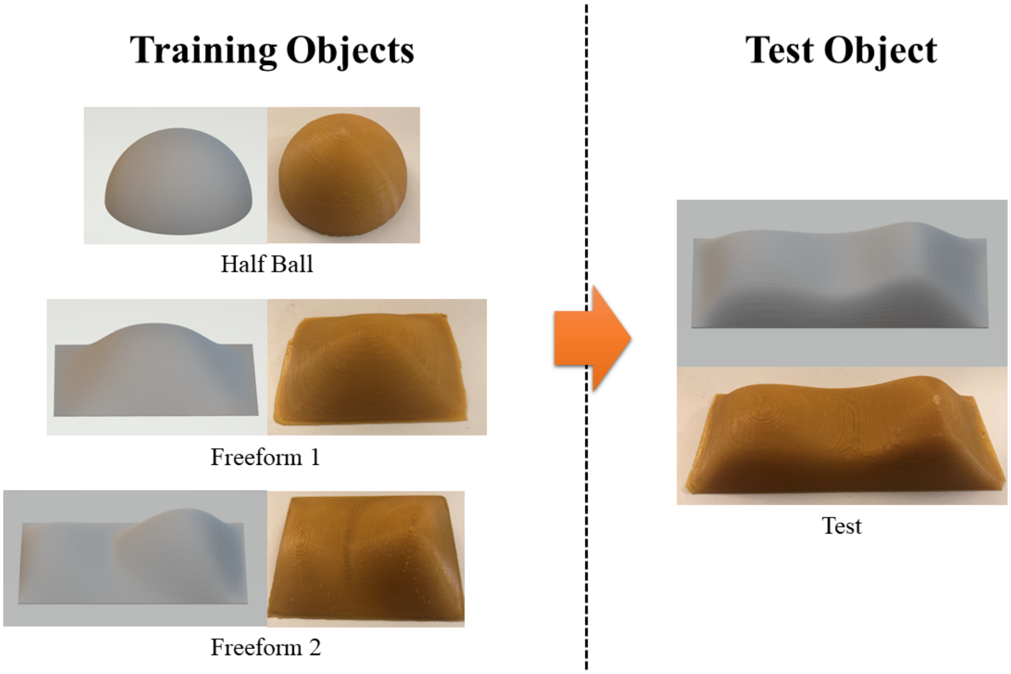

Figure 38: The training and test CAD models and physical objects considered in our case study. The CAD model for a product is to the left of the actual printed product's picture.

applied to all four objects. All landmarks for each training object were used to form the training data set for the single BELM, E-BELM, and Res-BELM models. Each BELM model utilized the hyperbolic tangent function as the activation function. The single BELM model has 50 hidden neurons. The E-BELM model had three layers for each of the 50 ensemble samples. The Res-BELM had 20 layers for each of the five stack-up BELM models. All these hyper-parameters are determined using the cross-validation technique [49].

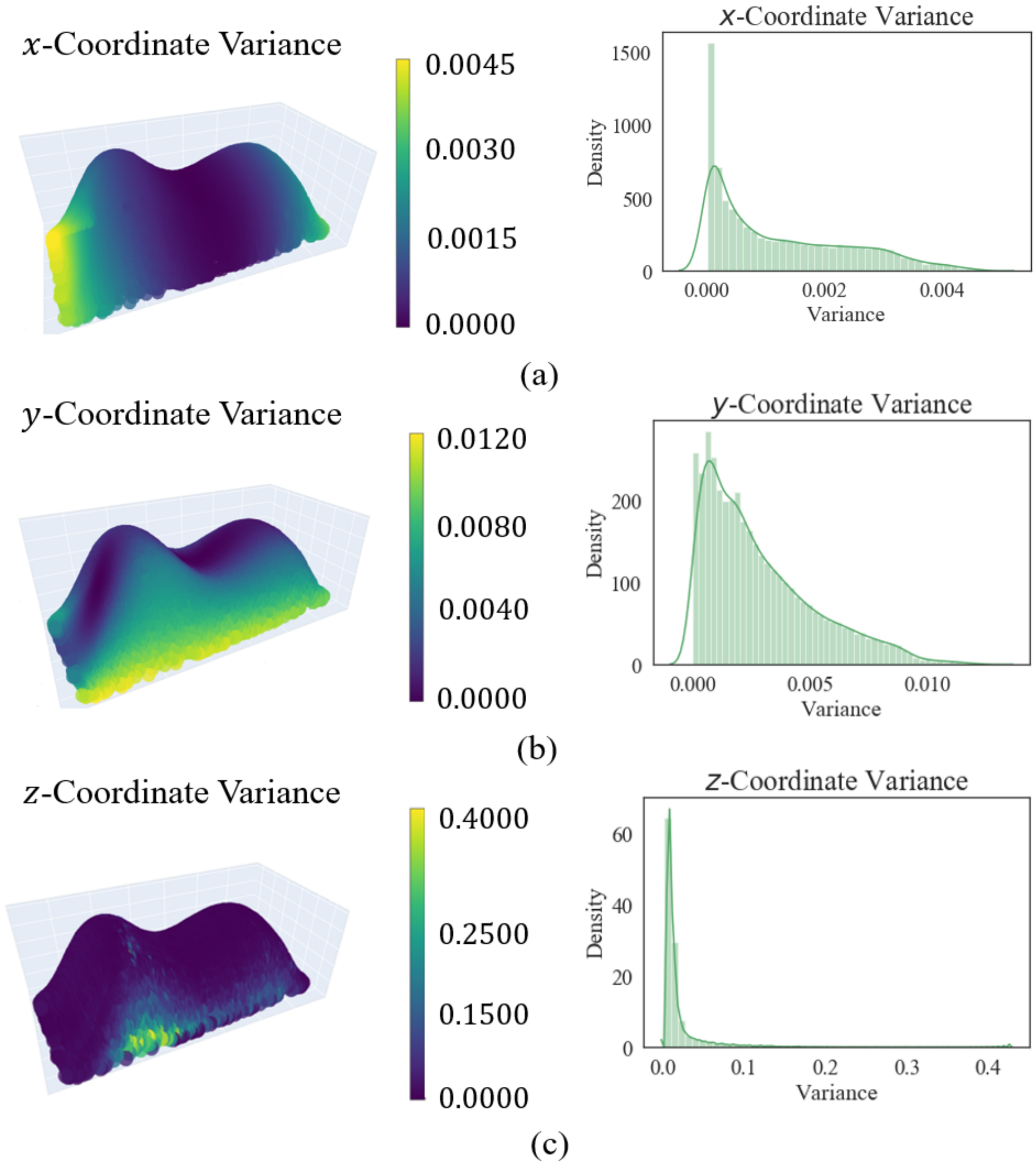

Figure 39: The variance distributions for each coordinate of the Test object.

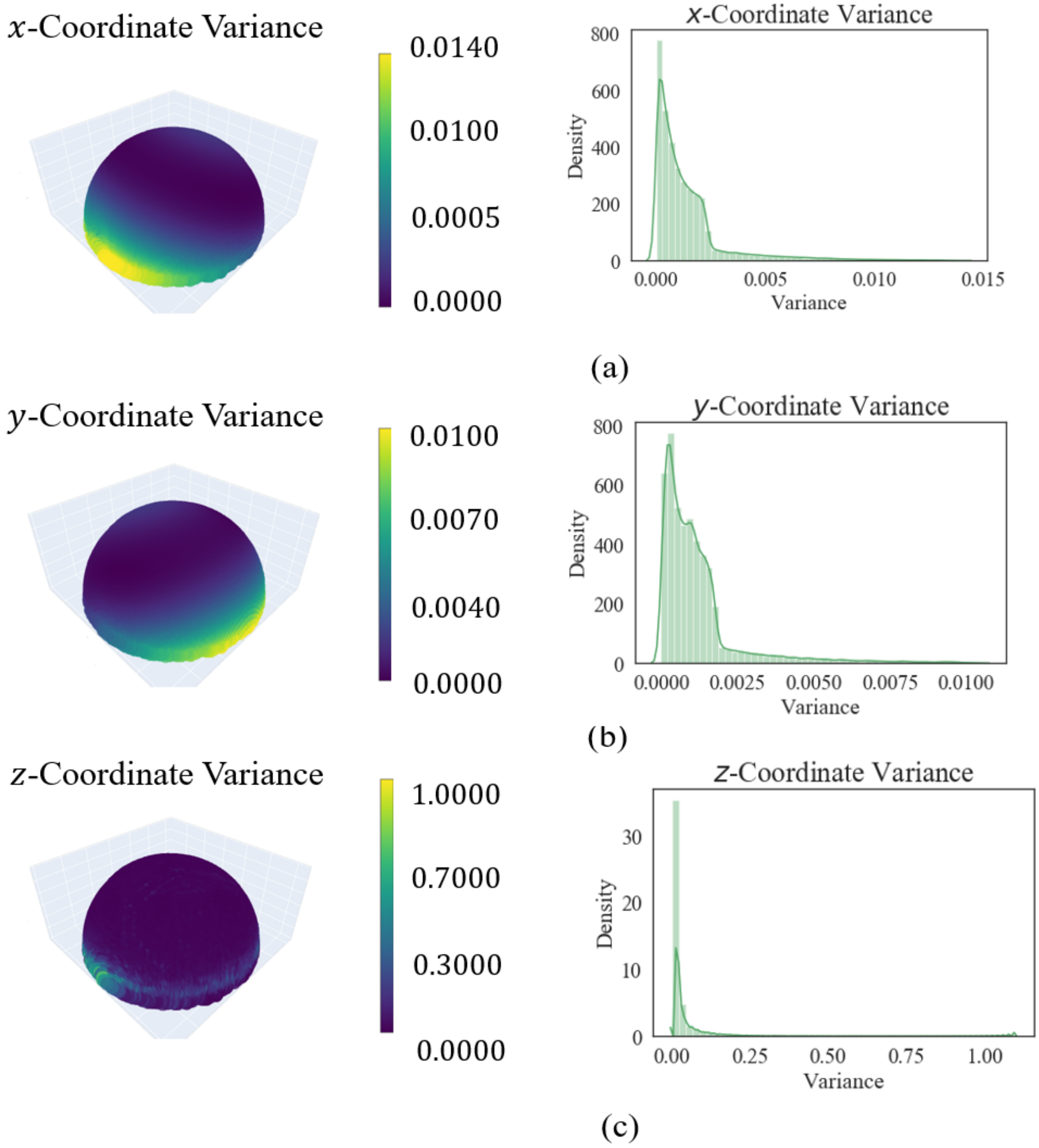

Figure 40: The variance distributions for each coordinate of the Half Ball object.

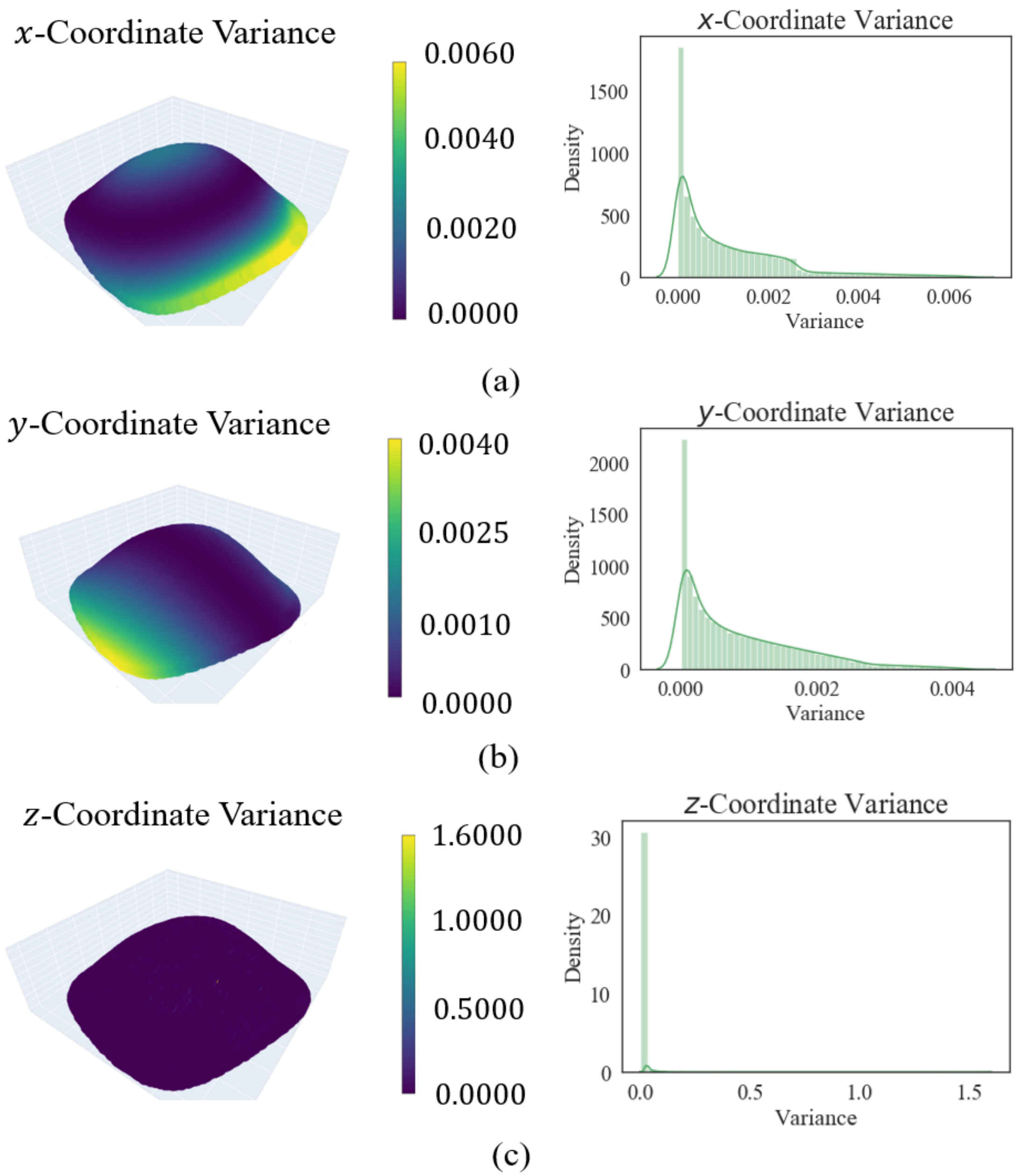

Figure 41: The variance distributions for each coordinate of the Freeform 1 object.

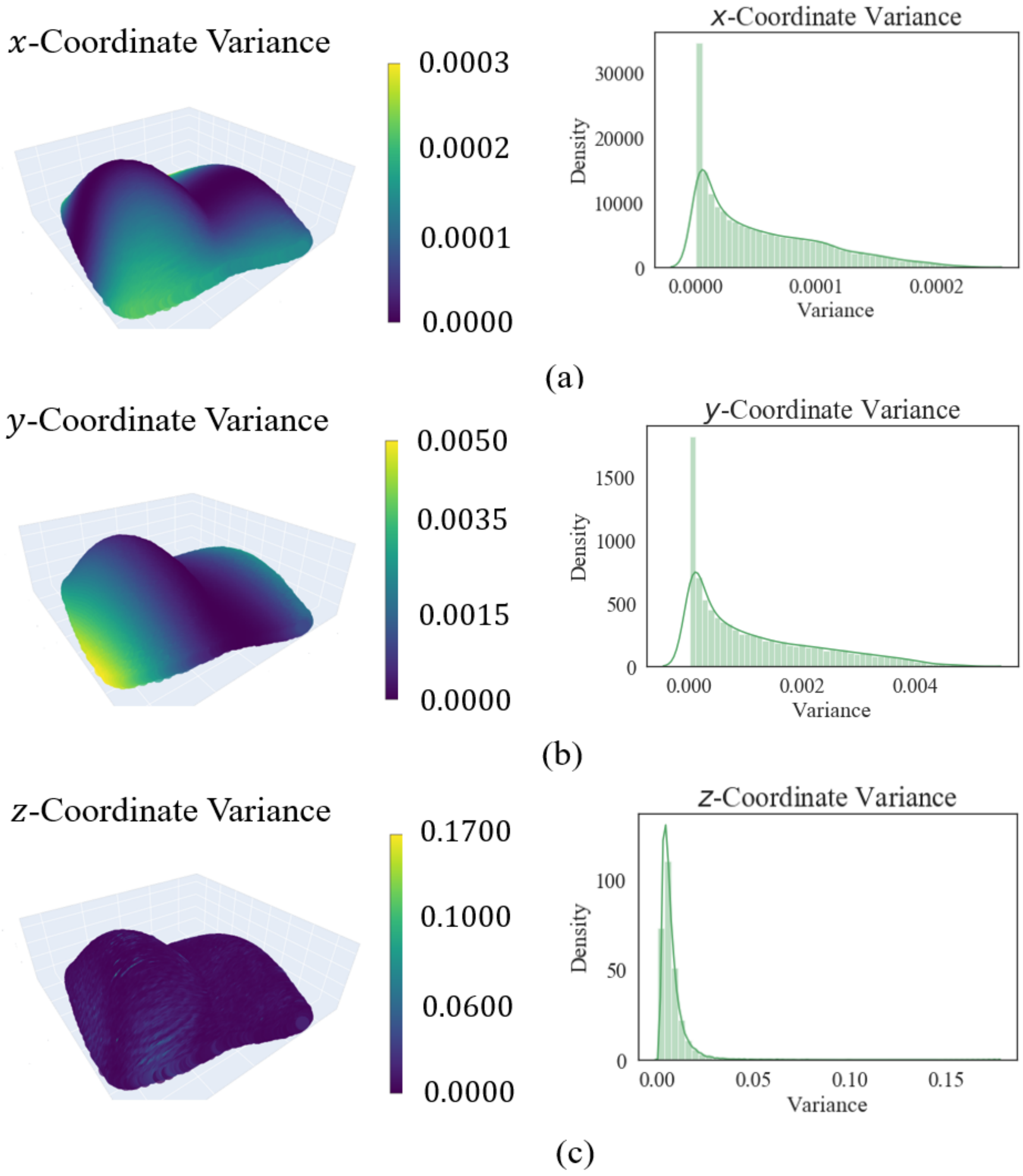

Figure 42: The variance distributions for each coordinate of the Freeform 2 object.

Tables 10, 11, and 12 contain the comparisons between the results obtained from our algorithms based on different scanning histories and those obtained from pre-experiment multiple initial scan trials in Chapter 4. A sampling method was utilized to compute the performances of the estimators obtained from multiple scans. First, c configurations, for $c = 2, 3, 4, 5$, were selected without replacement from the 30 total scans. Second, the PPA algorithm was performed on the selected configurations. Finally, the variances were estimated via the range statistics [114, p. 237] for each landmark. These comparisons are formally based on root mean square error (RMSE) as defined by

$$\mathrm{RMSE}_j = \sqrt{\frac{\sum_{i=1}^{k} (\sigma_{ij}^2 - \hat{\sigma}_{ij}^2)^2}{k}}, \tag{6-6}$$

where σ_{ij}^2 denotes the observed sample variance of landmark i for coordinate $j \in \{x, y, z\}$ of the test shape, and $\hat{\sigma}_{ij}^2 = \exp(\hat{t}_{ij})$ is its corresponding prediction, with $\hat{t}_{ij}$ being the predicted value from the BELM model for coordinate j.

The prediction error and its standard deviation of the z-coordinate are significantly higher than those of the x- and y-coordinates since the magnitude of the z-coordinate variances is greater than that of the other two coordinates [41, 145], which corresponds to the greater importance of predicting z-coordinate variance in RE and metrology process planning (Chapter 4). Furthermore, Freeform 1 and Freeform 2 yield better variance model performance than those obtained from the small number of initiation scans and those obtained from the BELM models trained by Half Ball (which exhibits comparatively worse performance). These results can be explained by examining the geometric features' distributions (Figure 43). Specifically, the shapes of the distributions for both features of Freeform 1 and Freeform 2 are much closer to those for the Test object, which indicates their expected better performance than the Half Ball. In addition, the ranges of both features for the Half Ball are smaller and more concentrated than those for the Test object, which indicates the increased possibility of extrapolation error for the trained BELM model. Furthermore, the empirical KL divergences under different numbers of bins (Table 13 and Figure 44) indicate that the Half Ball object should behave much worse than the Freeform 1 and 2 objects in terms of predicting variances for the Test object. Finally, we note that Freeform 1 has a

Table 10: Comparison of RMSEs (in mm) for x-coordinate variance prediction based on the three BELM architectures and multiple initiation scans involving 30 replicate scans.

Estimation Method	Training History	RMSE (Mean)	RMSE (Standard Deviation)
Multiple Initiation Scans	Two	0.0346	0.0294
	Three	0.0331	0.0190
	Four	0.0316	0.0166
	Five	0.0391	0.0111
Single BELM	Half Ball	0.0120	0.0033
	Freeform 1	0.0017	0.0002
	Freeform 2	0.0017	2.6401×10^{-6}
E-BELM	Half Ball	0.0019	0.0002
	Freeform 1	0.0014	6.2491×10^{-5}
	Freeform 2	0.0017	6.3368×10^{-7}
Res-BELM	Half Ball	0.0071	0.0018
	Freeform 1	0.0019	0.0003
	Freeform 2	0.0017	2.5983×10^{-6}

value closer to 0; therefore, the BELM model trained by this object is expected to yield a better variance modeling performance for the Test object. This conclusion can be verified by an examination of Table 12. These observations further support the conclusion that the Half Ball should not be chosen as the scanning history.

According to the RSME results in Tables 10, 11, and 12, Freeform 1 only performs significantly better in the variance estimation of the z-coordinate. This phenomenon can be explained by Figure 44, where the empirical KL divergence values for this training object are very close and related to the choice of the number of bins. As a result, no major difference should be expected between these two objects. This conclusion is verified with the number of bins $l = 30$ (Table 13 and Figure 44).

Table 11: Comparison of RMSEs (in mm) for y-coordinate variance prediction based on the three BELM architectures and multiple initiation scans involving 30 replicate scans.

Estimation Method	Training History	RMSE (Mean)	RMSE (Standard Deviation)
Multiple Initiation Scans	Two	0.0565	0.0360
	Three	0.0463	0.0217
	Four	0.0451	0.0168
	Five	0.0401	0.0142
Single BELM	Half Ball	0.0309	0.0016
	Freeform 1	0.0034	8.7623×10^{-6}
	Freeform 2	0.0032	8.5538×10^{-5}
E-BELM	Half Ball	0.0031	3.3726×10^{-5}
	Freeform 1	0.0034	6.2605×10^{-6}
	Freeform 2	0.0032	1.0992×10^{-5}
Res-BELM	Half Ball	0.0033	3.0234×10^{-5}
	Freeform 1	0.0033	9.9568×10^{-6}
	Freeform 2	0.0033	0.0001

Lastly, we observe that the E-BELM and Res-BELM models outperform the single BELM model. These two models have similar RSME results (Tables 10, 11, and 12), while the E-BELM provides a relatively smaller prediction variance. Even for the Half Ball, which has extensive extrapolation areas according to Table 13, both models can provide stable predictions with tolerable accuracy compared to the single BELM.

Table 12: Comparison of RMSEs (in mm) for z-coordinate variance prediction based on the three BELM architectures and multiple initiation scans, involving 30 replicate scans.

Estimation Method	Training History	RMSE (Mean)	RMSE (Standard Deviation)
Multiple Initiation Scans	Two	0.1694	0.0504
	Three	0.1470	0.0327
	Four	0.1632	0.0256
	Five	0.1324	0.0237
Single BELM	Half Ball	0.5242	0.0857
	Freeform 1	0.0048	0.0002
	Freeform 2	0.0063	0.0004
E-BELM	Half Ball	0.0239	0.0027
	Freeform 1	0.0034	5.1544×10^{-5}
	Freeform 2	0.0050	8.8159×10^{-5}
Res-BELM	Half Ball	0.0085	0.0008
	Freeform 1	0.0046	0.0002
	Freeform 2	0.0062	0.0004

6.6 Concluding Remarks

We presented an algorithm for variance modeling of 3D point-cloud data, as shown in Figure 45. Under the structure of the landmarks in VDA, our algorithm models the landmarks' variances as a function of two geometric features: the angle for the normal direction vector and the curvature change rate. The models utilized in our algorithm are structural variants of the BELM model: E-BELM and Res-BELM. An essential component in our algorithm is our new metric on point-cloud data that enables us to select scanning history for improved variance modeling.

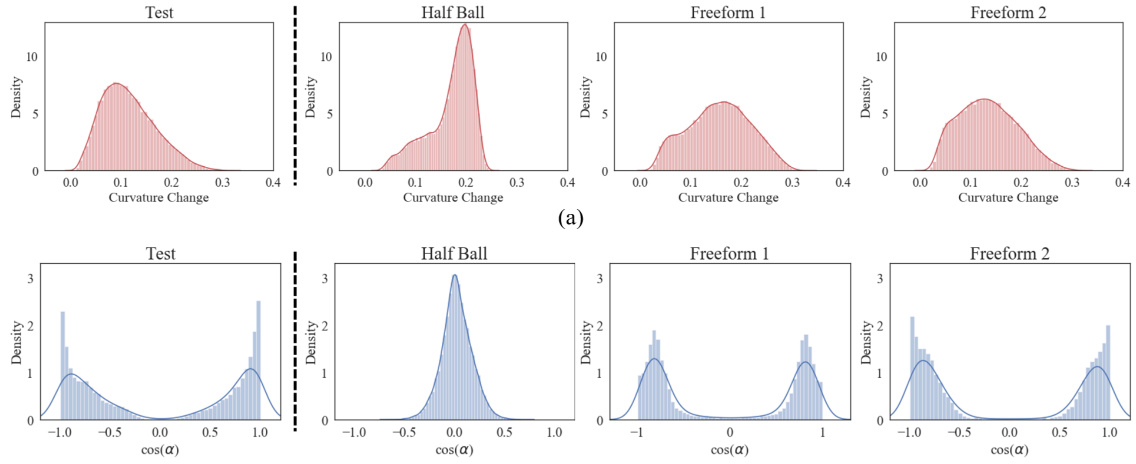

(a)

(b)

Figure 43: Empirical distributions of the geometric features for both the Test and training objects: (a) the rate of curvature change and (b) the cosine of the angles between landmarks' normal and the normal of the scanning platform, $(0, 0, 1)$.

Table 13: Values of the empirical KL divergence between the Test object and different choices of scanning histories, with penalty $s = 1000$ and number of bins $l = 30$.

Training Objects	Empirical KL Divergence
Half Ball	-466.3029
Freeform 1	-1.8424
Freeform 2	-24.2890

In contrast to the pre-experiment scanning procedure or prior knowledge in Chapter 4, our empirical KL divergence method can directly utilize one scan model to automatically perform variance modeling. The proposed history selection algorithm could be employed to find appropriate training objects to yield high prediction performance. Ultimately, our usage of local geometric descriptors as regressors in our model plays a critical role in enabling automated deviation modeling across various geometric specifications. Any RE and metrology

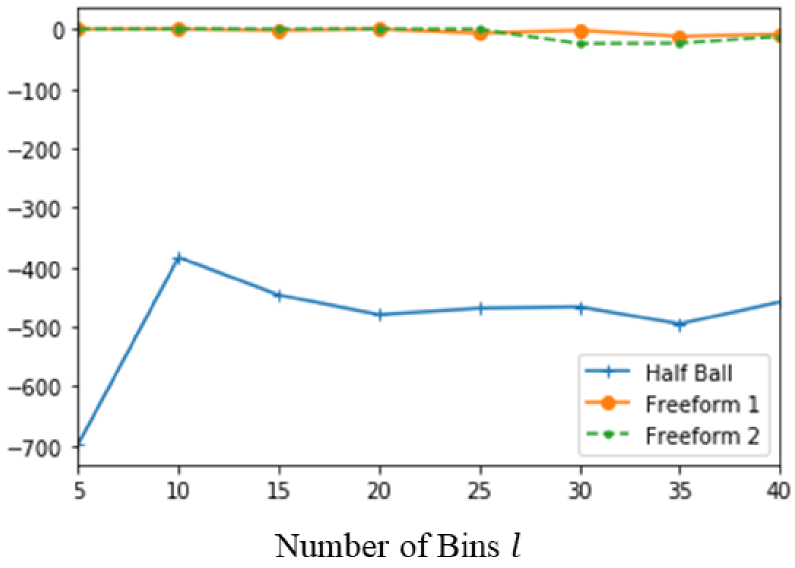

Figure 44: Empirical KL divergence for three scanning histories under different numbers of bins $l = 5, 10, \ldots, 40$.

experiments could be recorded and summarized as a training model for future applications. Furthermore, the two structural variants, the E-BELM and Res-BELM, outperform the original BELM model, providing more accurate predictions with lower prediction variances.

Our algorithm is an extension of the current VDA framework. Instead of analyzing an entire configuration, as in classical statistical shape analysis applications, the landmark-wise analysis is connected to local geometric information. Our proposed methodology can be widely used for RE and metrology applications, such as repetitive measurement process planning and scanning process capability analysis. For example, in place of multiple pre-experiment scans, only one single-scan is required as the input to the RE process planning model to develop the repetitive measurement plans. Furthermore, the design-independent feature of our algorithm can be generalized to analyze general 3D point cloud data. Although we only focused on variance modeling, other outcomes can be considered for our algorithm. Our methodology can be applied for applications such as scanner calibration and AM compensation schemes, whose factors of interest can be related to local geometric information.

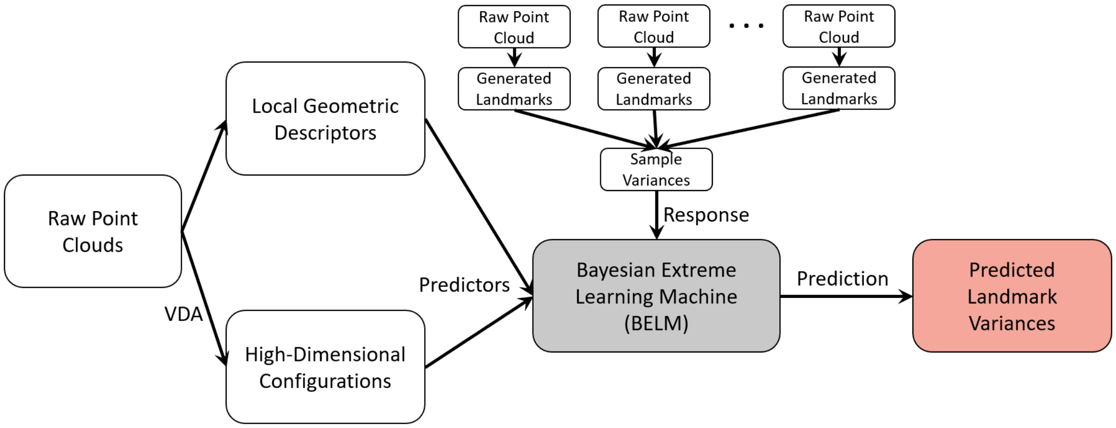

Figure 45: Process map of the point-cloud variance modeling technique presented in Chapter 6.

7.0 Geometric Accuracy Analysis for AM: A Comparative Study

In this chapter, we utilize the VDA framework to analyze the effect of process parameters on the accuracy of the AM fabricated parts. This framework bridges the gap between 3D point-cloud data and statistical inferential techniques to learn AM process knowledge from the printed parts. A novel projection-based statistic is proposed in Section 7.1 for comparative study under two different AM process settings. Section 7.2 presents simulated results to show the statistical power of the proposed test statistic. An actual experiment is designed in Section 7.3 to compare the geometric accuracy of the part samples printed under two levels of layer thickness using the FDM process. The remainder of this chapter can be found in [57].

7.1 A Two-Sample Comparative Study

This study focuses on developing a hypothesis testing scheme for two sample mean configurations under the VDA umbrella. Hypothesis testing is critical in statistical methodology development, especially the ones in quality engineering. Specifically, DOE techniques utilize hypothesis testing to compare experimental outcomes and discover the critical process parameters; SPC techniques use hypothesis testing to detect the shift in continuous production processes.

7.1.1 Data Model for the Configurations

To analyze the landmarks under different AM process settings, we first need to build an observation model for the configurations. After performing the landmark generation and registration steps in the VDA framework, the registered landmarks are transformed into the size-and-shape space, where the translational and rotational factors are removed from the configurations. A data model for the configurations needs to be set up to separate the different sources of variations. Considering the point clouds collected from the 3D scanner, the uncertainty in the data comes from three major sources: (1) the variations in the AM process and different process settings; (2) the scanning and measurement process; and (3) the interference between the object and the scanner. Therefore, the data model can be written as

$$X = \mu_{AM} + \epsilon, \tag{7-1}$$

where $\mu_{AM} = \mu + \delta_{AM}$ that μ is the true design configuration and δ_{AM} is the deviation caused by the process setting, and $\epsilon = \epsilon_{AM} + \epsilon_{RE} + \epsilon_I$ that ϵ_{AM}, ϵ_{RE}, and ϵ_I are the noise terms caused by the AM, RE, and interference, respectively.

7.1.2 Hypothesis Testing Scheme

Assume the configurations collected from two different AM process settings are random matrices. The first moment, the mean, of a random matrix describes the center of location for a random variable. Therefore, the equality of the means indicates the distributions are centered around the same region in the parameter space. For AM-created parts, if the parts produced by two-process settings have the same mean, these parameter settings could produce the same accuracy. Then, the decision-making regarding process settings can be determined solely based on the time or cost considerations. Otherwise, a setting that provides the products with higher accuracy is preferable.

Suppose the two configuration variables can be characterized by their means, $X \sim F(\cdot, \mu_1)$ and $Y \sim G(\cdot, \mu_2)$, where $\mu_1, \mu_2 \in \mathbb{R}^{k\times 3}$ are the mean configurations. The hypothesis of comparing mean configurations can be stated as

$$\begin{aligned} H_0 &: \mu_1 = \mu_2 \\ H_a &: \mu_1 \neq \mu_2. \end{aligned} \tag{7-2}$$

Since μ_1 and μ_2 are $k \times 3$ matrices, testing the matrix hypothesis is cumbersome. One widely used hypothesis testing scheme is the Goodall's F statistic in SSA [63]. However, the two degrees of freedom of this F statistic are q and $(2n-2)q$, where n is the sample size for both configuration samples, and $q = 3k - 7$, where k is the number of landmarks. As k becomes larger, both degrees of freedom increase linearly with respect to k. Therefore, in a high dimensional setting, Goodall's F statistic may not be sensitive to small deviation or even inaccessible. Luckily, the approximation after PPA proposed by [64] provides the independence of the coordinates for each landmark, as shown in Chapter 3. Therefore, testing the hypothesis in equation 7-2 is equivalent to test

$$\begin{aligned} &H_0 : vec(\mu_1) = vec(\mu_2) \\ &H_a : vec(\mu_1) \neq vec(\mu_2). \end{aligned} \tag{7-3}$$

Testing the equality of mean configurations is equivalent to testing the hypothesis of a pair of high-dimensional mean vectors. High-dimensional inference regarding mean vectors has attracted lots of research interest during the past decades. Several major techniques have been developed in this area for hypothesis testing purposes. One major field is the extension of the traditional Hotelling's T^2 [156] test statistic in high-dimensional parameter space. The key idea is to construct the statistic based on the Euclidean norm of the difference in sample means with excellent asymptotic properties. One representative work is proposed by Bai and Saranadasa [9]. However, a significant constraint of this methodology is that strict assumptions are required on either the sample size or covariance structure.

Another methodology is the projection-based test statistic. For $p \leq 3k$, consider a matrix $\Gamma \in \mathbb{R}^{p \times 3k}$ with full row rank. In this case, the difference in means, $vec(\mu_1) - vec(\mu_2)$, is equal to zero if and only if $\Gamma(vec(\mu_1) - vec(\mu_2)) = 0$. That is, the hypothesis in lower column dimension space of Γ is equivalent to the original hypothesis. Then, the hypothesis can be rewritten as

$$\begin{aligned} &H_0 : \Gamma\ vec(\mu_1) = \Gamma\ vec(\mu_2) \\ &H_a : \Gamma\ vec(\mu_1) \neq \Gamma\ vec(\mu_2). \end{aligned} \tag{7-4}$$

The equivalence holds for any matrices Γ with full row rank satisfying $p \leq 3k$. There is a large collection of matrices that satisfy this condition. One natural choice of such Γ is the first p principal components calculated from the pooled sample covariance matrix

$$
\begin{aligned}
S \;=\; \frac{1}{2n-2}\Bigg\{ & \sum_{i=1}^{n} \big(vec(X_i) - vec(\bar{X})\big)\big(vec(X_i) - vec(\bar{X})\big)^T \\
& + \sum_{i=1}^{n} \big(vec(Y_i) - vec(\bar{Y})\big)\big(vec(Y_i) - vec(\bar{Y})\big)^T \Bigg\}
\end{aligned} \tag{7-5}
$$

using PCA. In equation 7-5, X_i's and Y_i's, $i = 1, \dots, n$, are the registered configurations after performing the PPA algorithm, $\bar{X} = \frac{1}{n}\sum_{i=1}^{n} X_i$ and $\bar{Y} = \frac{1}{n}\sum_{i=1}^{n} Y_i$ are the sample mean configurations. The calculation of PCA is well-studied in [2, 84, 177].

Following the projection, we can calculate the Hotelling's T^2 statistic using the projected data,

$$
T_p^2 = \frac{2n-p-1}{(2n-2)p}\,\frac{n^2}{2n}\sum_{j=1}^{p}\frac{(\bar{X}_j^* - \bar{Y}_j^*)^2}{\lambda_j}, \tag{7-6}
$$

where $X_i^* = \Gamma^T X_i$ and $Y_j^* = \Gamma^T Y_j$, the columns of Γ are the first p principal components of the pooled sample covariance matrix, and λ_j is the jth eigenvalues. For any $k \leq p$, the null distribution of T^2 will be $F_{p,2n-p-1}$. Suppose the significance level is controlled at α. Then, if $T^2 > F_{p,2n-p-1}(\alpha)$, we could reject the null hypothesis and concludes that the AM process parameter affects the geometric accuracy of the produced parts; otherwise, the process parameter may not affect the parts' geometric quality.

7.2 Power Analysis

Statistical power is the probability that a test procedure will detect an effect, given that this effect truly exists. It is usually utilized to either determine the sample size for a predetermined power level or compare the sensitivity among different testing procedures for a given sample size. In the AM applications, various sources of variations are presented in the registered configurations offered in the previous sections. These variations are usually given in significant quantities and could potentially be detrimental to the significance of the test. Therefore, a hypothesis testing that is more sensitive to the difference in means is preferable. In other words, the test procedure with a higher power in small sample sizes is necessary for the AM applications. We study the statistical performance of the following four methods used to determine the difference in geometric accuracy of the configuration samples: (1) the projection-based test (Section 7.1); (2) the Goodall's F test proposed in [43]; (3) the permutation test based on Goodall's F statistic (based on 100 permutations) [23]; and (4) the Bai-Saranadasa's test statistic [9]. Configurations are simulated from a half-ball-shaped design. In the AM processes, the shape of a circular layer could be changed to a less circular profile because of layer warping [127] or thermal shrinkage [74]. A sine noise with period 2π and amplitude δ is added to the circular layer simulating this phenomenon, whose shape is close to the results in [48]. One hundred fifty layers are simulated, while the sine noise is only simulated on the layers in the range of 30-60 and 100-120. Fifty landmarks are simulated on each layer. A sequence of δ values is tested to simulate the power curve. Rather than a constant error, the amplitude δ is assumed to be a multiple of w of the ratio σ/R_i as in [23], where σ is the standard deviation of the random noise, and R_i is the radius of the ith layer. Thus, the amplitude shift is given by $\delta = w\sigma/R$. The values tested for w are in the range of $[0, 3.25]$, with a 0.25 step size.

Twenty parts ($n = 20$) are simulated at the amplitude level of 0 and δ. For each value of the w multiplier, 100 simulations are performed, and $i.i.d.$ errors with $\mathrm{N}(0, \sigma^2)$ distribution are added to each coordinate of the landmarks. The desired level of significance α is set at 5%. A value of $\sigma = 0.1$ and $R_0 = 20$ is used to generate the plot, as shown in Figure 46.

From Figure 46, it is obvious that Bai-Saranadasa's test statistic cannot detect differences in simulated configurations. The low power is probably caused by the violation of its strict model assumptions. Furthermore, the performance of the projection-based test is bad with a smaller number of components ($p = 3$). However, when $p = 3$, its performance is close to Goodall's F test and the permutation test. With the increase of p, the projection-based test scheme outperforms these classic shape-based test procedures. The projection-based test achieves the desired α level and has a probability of difference detection that is much higher than that of the traditional methodologies.

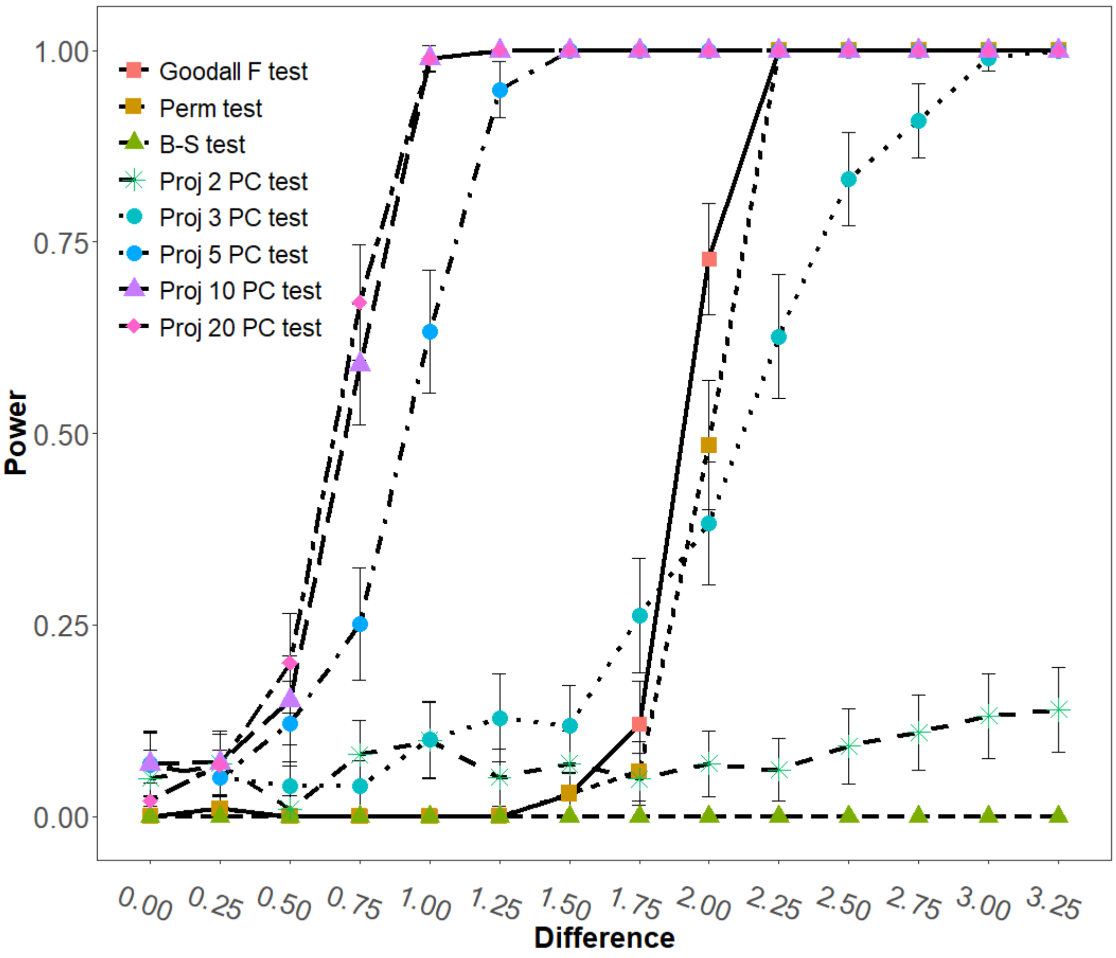

Figure 46: Power results for simulated Half-Ball configurations ($\alpha = 0.5$) for the comparative study based on the sine form noise on 30-60 and 100-120 layers.

7.3 Case Study: Layer Thickness

Layer thickness, θ, is a unique process parameter of AM processes. The values of layer thickness heavily affect the production time of the AM processes. For a fixed design, the greater the value of layer thickness, the smaller the number of layers that need to be printed. Since the printing time of each layer is almost identical for different layer thicknesses, it can be sharply reduced with larger layer thicknesses. However, this could cause the sacrifice of the resolution of the final production. Therefore, it is important to know how the layer

Table 14: Results for FDM printing experiments with batch size 5, where θ denotes the layer thickness (in mm); t represents the printing time (in hour); and G_P and Δ are the Procrustes distance (in mm^2) and maximum deviation (in mm), respectively.

θ	t	G_P	Δ
0.18	8:42	451.2676	0.2951
0.38	4:38	110.3738	0.1244

thickness affects the geometric accuracy of the AM-created parts. More importantly, it is critical to determine the optimal layer thickness to meet the accuracy requirements and shorten the production time.

An experiment is designed to test whether the layer thickness could affect the accuracy and, if so, which setting is preferable. Specifically, a half-ball-shaped design is selected for the experiment. The LulzBot TAZ printer (Figure 22(b)) is utilized to perform the experiment using a 2.85 mm gold metallic polymer filament. A two-level of layer thickness, 0.18 mm and 0.38 mm, are selected for a comparative study. For each level, 20 samples are created, which are printed in four batches. The printed samples are scanned by FARO Platinum 8' Arm Laser Scanner (Figure 22(a)). The p value is calculated by the projection-based testing procedure, whose value is 3.5527×10^{-15}. The result shows that there is a significant difference regarding the geometric accuracy for these two levels.

To further discover which printing setting provides the products with higher geometric accuracy, the mean configurations for both settings are compared with the configuration from the design. Table 14 reports both Procrustes distance and maximum deviation values. It shows that the parts printed under $\theta = 0.38$ mm are much closer to the design than the 0.18 mm ones. The result is somewhat counterintuitive but still reasonable. Even though the design printed with a smaller layer thickness could provide a better resolution, the number of layers is almost doubled compared to $\theta = 0.38$. With more layers, if each real layer thickness is modeled as a random variable with a small constant deviation, the variance and cumulative deviation of the overall height of $\theta = 0.18$ would be much higher. Therefore, the vertical deviation and variance may cause a larger deviation from the design.

Table 15: Comparisons between the points collected from the Renishaw CMM machine (CMM) and the laser scanner (LS), where $sG_p = G_p/n$ is the average of the standardized Procrustes distance (in mm^2) of each setting andΔ is the average of the maximum deviation (in mm) of each setting.

θ	sG_P(LS)	sG_P(CMM)	Δ(LS)	Δ(CMM)
0.18	0.0605	0.0577	0.2951	0.2540
0.38	0.0148	0.0135	0.1244	0.0976

The Renishaw Cyclone Touch Probe Scanner is utilized to measure the AM-created objects under these two settings. The average of the standardized Procrustes distance, $sG_p = G_p/n$, where n is the number of landmarks or points, and the average of the maximum deviation is utilized as the measures to compare the points collected by the CMM and the laser scanner, which is shown in Table 15. As for the point clouds surveyed by the laser scanner, 7450 landmarks are generated for analysis compared to the 225 surveyed points by CMM.

7.3.1 Visualization Diagnostics

One of the major contributions of the VDA is to provide one-on-one correspondence of the landmarks among point clouds. Therefore, the deviation of the mean configuration of each process setting from the design could be directly visualized with little effort. The deviation plots of both settings are shown in Figure 47. The landmarks are generated through a support plane projection algorithm (Figure 15), so the deviations along the x- and y-direction can be negligible. According to the plot, it is obvious that the deviations of the 0.18 mm setting are more smoothly changed when compared to the ones of 0.38 mm. However, the overall deviation of 0.38 mm seems to be much smaller.

Furthermore, it can be seen that large deviations can be identified around the middle in the height of both parts. This phenomenon is possibly caused by the change of material

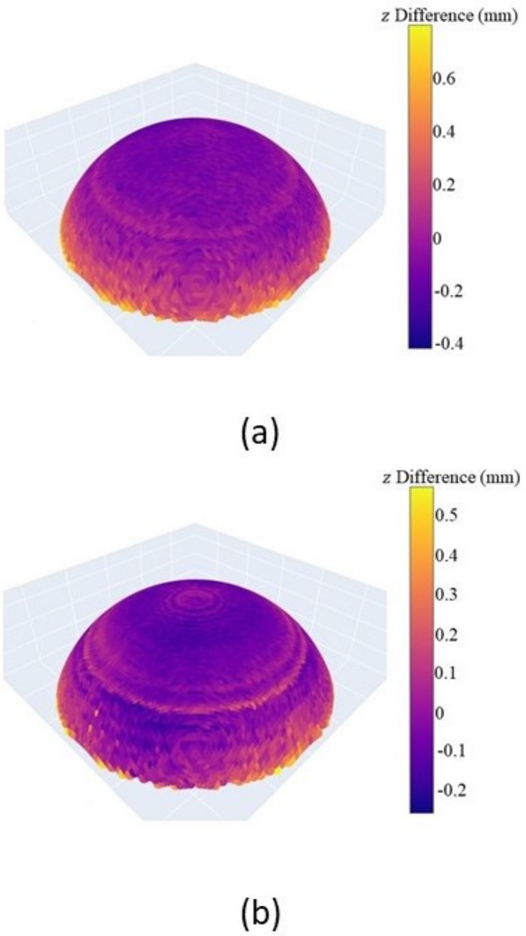

Figure 47: Visualization of the pointwise deviations: (1) 0.18 mm and (2) 0.38 mm.

behavior or the change of infill by the printer. Since the design is half-ball-shaped objects, the angle between the point-wise normal direction and builds orientation, ϕ, ranges from 0° to 90°. Due to gravity, the materials tend to have a sink effect after 45 degrees. AM packages usually solve this problem by changing the infill rate or pattern, which could potentially cause the deviation. On the other hand, the effectiveness of this algorithm on increasing geometric accuracy is also unknown. More designed experiments are required to further investigate the causality of this behavior and find the solutions to improve the geometric accuracy. In summary, this diagnostic tool could provide both researchers and practitioners with direct visualization capability for knowledge discovery and process analysis.

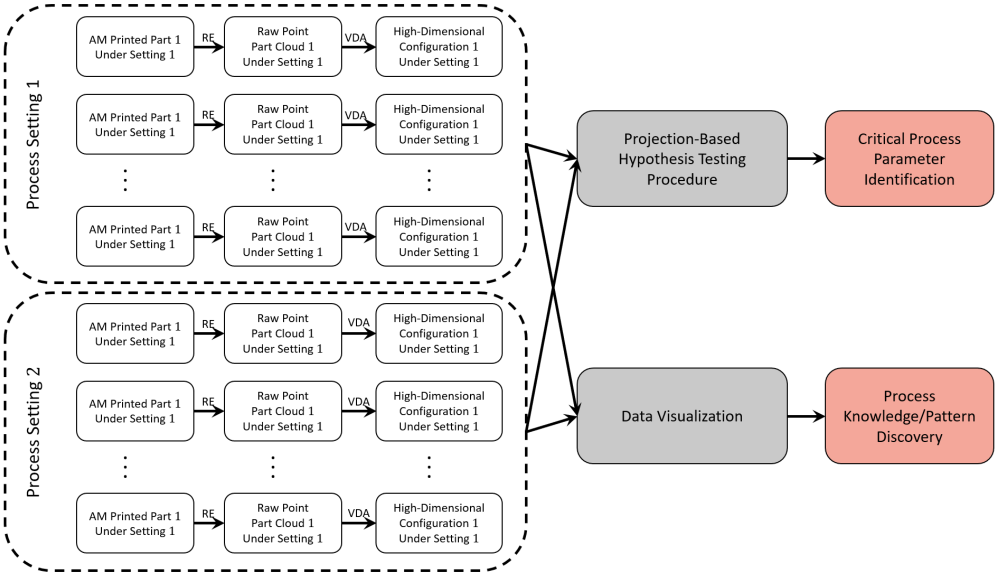

Figure 48: Process map of the two-sample high-dimensional hypothesis testing procedure in the size-and-shape space presented in Chapter 7.

7.4 Summary and Conclusions

In this chapter, a high-dimensional test procedure in a low-dimensional projection space is proposed to compare the part accuracy under different AM process settings. The process map of this test procedure is presented in Figure 48. Power analysis is presented to show that the proposed testing scheme is much more powerful and sensitive than other procedures. A practical experiment is discussed for the analysis of layer thickness. One important finding is that, even though a small layer thickness could provide the parts with high resolution, it may not necessarily provide more accurate parts when compared to large layer thickness. In addition, a simple deviation diagnostic tool is proposed to visualize the deviation pattern for knowledge discovery and process analysis.

8.0 Conclusions and Future Work

8.1 Concluding Remarks

The primary contribution of this study is to link current advanced analytical methodologies and advanced manufacturing processes, e.g., RE and AM. This dissertation bridges the gap by introducing a novel statistical framework, VDA, that extends the current point-based or profile-based inspection and analytical tools to deal with 3D closed-shape point clouds. Auto landmark generation algorithms are developed while maintaining the precision requirements for manufacturing. Modern statistical methodologies, such as statistical shape analysis, statistical learning, and high dimensional statistical techniques, are first introduced into the field of advanced manufacturing processes through this framework.

The proposed framework is utilized to solve several critical research problems in RE and AM. A novel method to (re)construct a more accurate description of the initial design by several scans of multiple parts occurs in Chapter 4. Furthermore, a unique registration method that mimics the original design, production, and quality inspection processes is introduced for better RE precision. This research expands RE's definition from an isolated information extraction process to a more general 3D "manufacturing process" that connects the physical objects and re-manufacturing processes through producing CAD models. Therefore, the complete re-manufacturing system analysis should incorporate the tolerancing and process planning for REP to produce more accurate products.

The presented method can solve the critical process-planning problems in RE, e.g., how many scans and parts are required to meet the predetermined precision requirements for RE practitioners. A tolerance-inference strategy is proposed to extract more design and production information for re-manufacturing process design and quality assurance. Furthermore, a unique variance-prediction technique is introduced to utilize machine learning algorithms, together with local geometric descriptors, to model the variability behavior of a given scanner. Two structural variants of the BELM are proposed with more accurate prediction performance. It is worth noting that both the tolerance-estimation methodology and the variance-modeling algorithm presented in Chapters 5 and 6, respectively, can be utilized in two ways. On the one hand, either can be implemented as an independent procedure for purposes such as re-manufacturing or scanning-process planning. On the other hand, they are also a nice complement to the RE process-planning model as prior information in the Bayesian modeling of the configurations.

Even more importantly, the VDA framework provides an opportunity to analyze unique AM characteristics, such as printing orientation and layer thickness, which are not possible for traditional techniques. As a first step, Chapter 7 introduces a high-dimensional hypothesis testing procedure to the VDA framework to compare the accuracy of the parts printed under different AM process settings. Therefore, this study is transformative because it integrates this novel statistical framework into classical analysis tools, such as experimental design tools, optimization models, and SPC methods, for better decision-making and process planning of advanced manufacturing processes. Expansions to other modern statistical methods, such as efficient experimental design strategy and SPC methods, could be developed along this direction to push forward the AM technology.

RE and AM are emerging manufacturing technologies that have a substantial impact on shortening life cycles and more flexible designs for new products and personalization manufacturing. We have a responsibility to advance the boundary of the current development in RE and AM based on their unique process characteristics. Also, it would be best to bridge the uniqueness of these modern manufacturing processes and the ample analytical tools available for traditional manufacturing processes. To address this challenge, we propose a novel framework in place of the multivariate or functional data analysis framework for a better understanding of 3D closed-shape point clouds. Manufacturing practitioners can directly implement the proposed methodologies to increase both the variety and quality of their products by using the combination of RE and AM. Using our framework, advanced manufacturing researchers and practitioners can design efficient process design and planning, engage in better decision-making, and implement effective control strategies to increase revenue and provide high-quality AM or re-manufacturing products.

8.2 Future Work

There are several lines of future work that can be raised based on this research. Potential research areas are presented as follows:

1. In Chapter 4, the design estimation procedure focused on using mechanical parts to estimate the original design. The configuration model considers the original production error and scanning error. As for some applications, especially legacy products remanufacturing, the parts may have been under heavy usage, which makes them either degraded, worn, or even broken. In such cases, the landmarks should be generated for each RE model created by ”repair” algorithms [8, 97], and then the original design should be estimated through the VDA framework applied to the ”repaired” configuration. In this case, expert knowledge, including design intention and process knowledge, combining with machine learning techniques, can be utilized to design reconstruction and re-manufacturing process planning.
2. Another potential improvement of the current tolerance-estimation method in Chapter 5 is incorporating the domain knowledge of assembly. The presented work concentrates on the estimation of the parts with the same design. However, the original tolerance designs, especially the one related to the mating features, also take the assemble capability into consideration. By incorporating the empirical tolerances for their counterparts, the estimated tolerances are likely to be more robust.
3. One of the major advantages of AM is its capability to produce parts with complex designs, which are usually constrained by traditional manufacturing systems. Therefore, instead of solely producing parts, the assemblies could be directly printed via AM through part consolidation. Low quality, high cost, and substantial time consumptions are the significant drawbacks of AM processes that prevent them from broader industrial applications. However, if the parts are integrated through part consolidation, the tolerance regions for the assemblies are comparatively larger than each of the sub-assemblies because of the stack-up effect. On the other hand, part consolidation could avoid the production costs for each sub-assembly and the assembly cost. One of our ongoing research topics is to develop a framework—named reducing assembly tolerance analysis

(RATA)—to analyze and estimate the tolerance design for part consolidation. Therefore, another line of future work will focus on extending the presented framework to tolerance design and estimation for consolidated legacy parts to further make decisions regarding process selection and planning for consolidated parts re-manufacturing applications.

4. New directions of research can be developed based on our algorithm for variance modeling of point-cloud data. One involves further extensions of the idea of virtual metrology. Two major research topics in both RE and metrology are measurement planning, in which the objective is to automate the scanning process while providing a precise description of the object, and multi-resolution scanning data fusion or calibration, in which the objective is to reduce time or cost requirements for high accuracy and precision scanning. Our variance modeling algorithm effectively attempts to merge both research topics to identify a common solution. A set of virtual measured points can be simulated according to the designed or RE-generated CAD model, together with the variance model trained by the scanning history. Therefore, instead of time-consuming physical measurements, such a virtual measurement system could quickly identify high variance regions that may require additional, high precision measurement. Another area of future research is to incorporate the tolerances for the RE process into the general tolerance stack-up analysis in a re-manufacturing setting. Current RE practice assumes that the RE-generated model is the ”true” description of the object of interest. However, we demonstrated that point-wise variance exists and could cause deviations between the actual object and the RE-generated model. In the biomedical or aviation industries, it could be necessary to incorporate the tolerance for RE processes in the entire (re)manufacturing process planning.
5. Our future research will also focus on expanding the current hypothesis testing procedure to general experimental settings with multiple factors, e.g., the effects of the interaction between layer thickness and build-orientation regarding the part accuracy. VDA provides a scientific path to analyze AM process parameters, while traditional methods may not be appropriate. Also, each component of the VDA framework will be investigated in detail. Although the current research focuses on applying the parts produced by the FDM process, the VDA framework, in general, can be applied to analyze the parts

created by metal AM processes. In this case, one of the future topics will increase the power for even higher dimensional configurations to deal with the significant amount of the measurement error due to high roughness in the AM-created metal parts.

Even though the analysis of high dimensional geometric data, e.g., 3D point clouds, is still at an early age, the VDA framework provides a new way of thinking about the analysis of manufacturing processes and processing the product's geometric data. The point cloud can be analyzed in a more reasonable way by using this framework when compared to classical feature or profile-based analysis. The VDA framework also provides the possibility to analyze and compare the accuracy and precision of the 3D scanners to bridge the gap between high dimensional 3D point clouds and statistical inferential techniques, such as analysis of variance, statistical process monitoring, and machine learning, for process analysis and improvement.

Bibliography

[1] Abdel-Salam G Abdel-Salam, Jeffrey B Birch, and Willis A Jensen. A semiparametric mixed model approach to phase i profile monitoring. *Quality and Reliability Engineering International*, 29(4):555–569, 2013.

[2] Hervé Abdi and Lynne J Williams. Principal component analysis. *Wiley interdisciplinary reviews: computational statistics*, 2(4):433–459, 2010.

[3] Mukesh Agarwala, David Bourell, Joseph Beaman, Harris Marcus, and Joel Barlow. Direct selective laser sintering of metals. *Rapid Prototyping Journal*, 1995.

[4] Vijay Andrew Albuquerque, Frank W Liou, and Owen Robert Mitchell. Inspection point placement and path planning algorithms for automatic cmm inspection. *International Journal of Computer Integrated Manufacturing*, 13(2):107–120, 2000.

[5] Abdalla Alrashdan, Saeid Motavalli, and Behrooz Fallahi. Automatic segmentation of digitized data for reverse engineering applications. *IIE transactions*, 32(1):59–69, 2000.

[6] G Ameta, S Serge, and Max Giordano. Comparison of spatial math models for tolerance analysis: tolerance-maps, deviation domain, and ttrs. *Journal of Computing and Information Science in Engineering*, 11(2), 2011.

[7] Yi An, Peng Zhao, Zhuohan Li, and Cheng Shao. Self-adaptive polygon mesh reconstruction based on ball-pivoting algorithm. *International Journal of Computer Applications in Technology*, 54(1):51–60, 2016.

[8] Eyup Bagci. Reverse engineering applications for recovery of broken or worn parts and re-manufacturing: Three case studies. *Advances in Engineering Software*, 40(6):407–418, 2009.

[9] Zhidong Bai and Hewa Saranadasa. Effect of high dimension: by an example of a two sample problem. *Statistica Sinica*, pages 311–329, 1996.

[10] C Bradford Barber, David P Dobkin, and Hannu Huhdanpaa. The quickhull algorithm for convex hulls. *ACM Transactions on Mathematical Software (TOMS)*, 22(4):469–483, 1996.

[11] Igor Bešić, Nick Van Gestel, Jean-Pierre Kruth, Philip Bleys, and Janko Hodolič. Accuracy improvement of laser line scanning for feature measurements on cmm. *Optics and Lasers in Engineering*, 49(11):1274–1280, 2011.

[12] Guijun Bi and Andres Gasser. Restoration of nickel-base turbine blade knife-edges with controlled laser aided additive manufacturing. *Physics Procedia*, 12:402–409, 2011.

[13] B Bidanda, S Motavalli, and K Harding. Reverse engineering: an evaluation of prospective non-contact technologies and applications in manufacturing systems. *International Journal of Computer Integrated Manufacturing*, 4(3):145–156, 1991.

[14] Bopaya Bidanda and Yasser A Hosni. Reverse engineering and its relevance to industrial engineering: a critical review. *Computers & industrial engineering*, 26(2):343–348, 1994.

[15] Gabriel R Bitran, Elizabeth A Haas, and Hirofumi Matsuo. Production planning of style goods with high setup costs and forecast revisions. *Operations Research*, 34(2):226–236, 1986.

[16] Francois Blais, Marc Rioux, and J-Angelo Beraldin. Practical considerations for a design of a high precision 3-d laser scanner system. In *Optomechanical and electro-optical design of industrial systems*, volume 959, pages 225–246. International Society for Optics and Photonics, 1988.

[17] Edwin Boender. A survey of intersection algorithms for curved surfaces. *Computers & graphics*, 15(1):109–115, 1991.

[18] C Bradley and V Chan. A complementary sensor approach to reverse engineering. *J. Manuf. Sci. Eng.*, 123(1):74–82, 2001.

[19] Leo Breiman. Random forests. *Machine learning*, 45(1):5–32, 2001.

[20] Thomas Ditlev Brunoe, Ann-Louise Andersen, Daniel GH Sorensen, Kjeld Nielsen, and Mads Bejlegaard. Integrated product-process modelling for platform-based co-development. *International Journal of Production Research*, 58(20):6185–6201, 2020.

[21] Richard K Burdick, Connie M Borror, and Douglas C Montgomery. *Design and analysis of gauge R&R studies: making decisions with confidence intervals in random and mixed ANOVA models*. SIAM, 2005.

[22] V Carbone, M Carocci, E Savio, G Sansoni, and L De Chiffre. Combination of a vision system and a coordinate measuring machine for the reverse engineering of freeform surfaces. *The International Journal of Advanced Manufacturing Technology*, 17(4):263–271, 2001.

[23] Enrique Castillo and Bianca M Colosimo. Statistical shape analysis of experiments for manufacturing processes. *Technometrics*, 53(1):1–15, 2011.

[24] Sofia Catalucci, Nicola Senin, Samanta Piano, and Richard Leach. Intelligent systems for optical form measurement : automated assessment of pose and coverage. In *Proceedings of 2019 ASPE Annual Conference*, pages 1–6, October 2019.

[25] Bong Kuen Cha, Jae Yong Lee, Paul-Georg Jost-Brinkmann, and Noriaki Yoshida. Analysis of tooth movement in extraction cases using three-dimensional reverse engineering technology. *The European Journal of Orthodontics*, 29(4):325–331, 2007.

[26] VH Chan, C Bradley, and GW Vickers. A multi-sensor approach to automating co-ordinate measuring machine-based reverse engineering. *Computers in Industry*, 44(2):105–115, 2001.

[27] Kuen-Suan Chen, Kung-Jeng Wang, and Tsang-Chuan Chang. A novel approach to deriving the lower confidence limit of indices c_{pu}, c_{pl}, and c_{pk} in assessing process capability. *International Journal of Production Research*, 55(17):4963–4981, 2017.

[28] Jun-Ting Cheng, Cong-Jun Wang, Can Zhao, and Jian-Hua Mo. Design of a servo motion system and an image sampling and processing system on a 3d laser scanner. *The International Journal of Advanced Manufacturing Technology*, 33(11-12):1143–1148, 2007.

[29] Longwei Cheng, Andi Wang, and Fugee Tsung. A prediction and compensation scheme for in-plane shape deviation of additive manufacturing with information on process parameters. *IISE Transactions*, 50(5):394–406, 2018.

[30] YM Chiang and FL Chen. Sculptured surface reconstruction from cmm measurement data by a software iterative approach. *International journal of production research*, 37(8):1679–1695, 1999.

[31] Pramod N Chivate and Andrei G Jablokow. Review of surface representations and fitting for reverse engineering. *Computer Integrated Manufacturing Systems*, 8(3):193–204, 1995.

[32] Charles K Chui and Min-Jun Lai. Filling polygonal holes using c1 cubic triangular spline patches. *Computer Aided Geometric Design*, 17(4):297–307, 2000.

[33] Bianca M Colosimo, Qiang Huang, Tirthankar Dasgupta, and Fugee Tsung. Opportunities and challenges of quality engineering for additive manufacturing. *Journal of Quality Technology*, 50(3):233–252, 2018.

[34] Bianca M Colosimo, Quirico Semeraro, and Massimo Pacella. Statistical process control for geometric specifications: on the monitoring of roundness profiles. *Journal of quality technology*, 40(1):1–18, 2008.

[35] Bianca Maria Colosimo, Massimo Pacella, and Nicola Senin. Multisensor data fusion via gaussian process models for dimensional and geometric verification. *Precision Engineering*, 40:199–213, 2015.

[36] Bianca Maria Colosimo, Quirico Semeraro, and Massimo Pacella. Statistical process control for geometric specifications. *Statistical analysis of profile monitoring. Wiley*, pages 217–52, 2011.

[37] Kevin D Creehan and Bopaya Bidanda. Computer-aided reverse engineering of the human musculoskeletal system. *Virtual and Physical Prototyping*, 1(2):83–91, 2006.

[38] Kevin D Creehan and Bopaya Bidanda. Reverse engineering: a review & evaluation of non-contact based systems. *Rapid Prototyping*, pages 87–106, 2006.

[39] Brian Curless and Marc Levoy. A volumetric method for building complex models from range images. In *Proceedings of the 23rd annual conference on Computer graphics and interactive techniques*, pages 303–312, 1996.

[40] Enrique Del Castillo, Bianca M Colosimo, and Hussam Alshraideh. Bayesian modeling and optimization of functional responses affected by noise factors. *Journal of Quality Technology*, 44(2):117–135, 2012.

[41] Enrique Del Castillo, Bianca M Colosimo, and Sam Davanloo Tajbakhsh. Geodesic gaussian processes for the parametric reconstruction of a free-form surface. *Technometrics*, 57(1):87–99, 2015.

[42] Salil Desai and Bopaya Bidanda. Reverse engineering: a review & evaluation of contact based systems. *Rapid Prototyping*, pages 107–131, 2006.

[43] Ian L Dryden and Kanti V Mardia. *Statistical shape analysis: with applications in R*, volume 995. John Wiley & Sons, 2016.

[44] G Echevarría, Andrés Iglesias, and Akemi Gálvez. Extending neural networks for b-spline surface reconstruction. In *International Conference on Computational Science*, pages 305–314. Springer, 2002.

[45] Shinto Eguchi and John Copas. Interpreting Kullback–Leibler divergence with the Neyman–Pearson lemma. *Journal of Multivariate Analysis*, 97(9):2034–2040, 2006.

[46] Diaa F ElKott and Stephen C Veldhuis. Isoparametric line sampling for the inspection planning of sculptured surfaces. *Computer-Aided Design*, 37(2):189–200, 2005.

[47] Mohamad Ivan Fanany and Itsuo Kumazawa. A neural network for recovering 3d shape from erroneous and few depth maps of shaded images. *Pattern Recognition Letters*, 25(4):377–389, 2004.

[48] Raquel de Souza Borges Ferreira, Arman Sabbaghi, and Qiang Huang. Automated geometric shape deviation modeling for additive manufacturing systems via bayesian neural networks. *IEEE Transactions on Automation Science and Engineering*, 2019.

[49] Jerome Friedman, Trevor Hastie, and Robert Tibshirani. *The Elements of Statistical Learning*. Springer, 2nd edition, 2001.

[50] Akemi Gálvez, Andrés Iglesias, Angel Cobo, Jaime Puig-Pey, and Jesús Espinola. Bézier curve and surface fitting of 3d point clouds through genetic algorithms, functional networks and least-squares approximation. In *International Conference on Computational Science and Its Applications*, pages 680–693. Springer, 2007.

[51] Akemi Galvez, Andrés Iglesias, and Jaime Puig-Pey. Iterative two-step genetic-algorithm-based method for efficient polynomial b-spline surface reconstruction. *Information Sciences*, 182(1):56–76, 2012.

[52] Jian Gao, Xin Chen, Oguzhan Yilmaz, and Nabil Gindy. An integrated adaptive repair solution for complex aerospace components through geometry reconstruction. *The International Journal of Advanced Manufacturing Technology*, 36(11-12):1170–1179, 2008.

[53] Silvère Gauthier, William Puech, Roseline Bénière, and Gérard Subsol. Analysis of digitized 3d mesh curvature histograms for reverse engineering. *Computers in Industry*, 92:67–83, 2017.

[54] S. Geman and D. Geman. Stochastic relaxation, gibbs distributions, and the bayesian restoration of images. *IEEE Transactions on Pattern Analysis and Machine Intelligence*, PAMI-6(6):721–741, 1984.

[55] Zhaohui Geng and Bopaya Bidanda. Review of reverse engineering systems–current state of the art. *Virtual and Physical Prototyping*, 12(2):161–172, 2017.

[56] Zhaohui Geng and Bopaya Bidanda. Tolerance estimation and metrology for reverse engineering based remanufacturing systems. *International Journal of Production Research*, 2020. Accepted.

[57] Zhaohui Geng and Bopaya Bidanda. Geometric precision analysis for additive manufacturing processes: A comparative study. *Precision Engineering*, 69:68–76, 2021.

[58] Zhaohui Geng and Bopaya Bidanda. Medical applications of additive manufacturing. In *Bio-Materials and Prototyping Applications in Medicine*, pages 97–110. Springer, 2021.

[59] Zhaohui Geng, Arman Sabbaghi, and Bopaya Bidanda. Automated variance modeling for three-dimensional point cloud data via bayesian neural networks. *IISE Transactions*, 2021. Under review.

[60] Zhaohui Geng, Arman Sabbaghi, and Bopaya Bidanda. Reconstructing original design: process planning for reverse engineering. *IISE Transactions*, 2021. Under review.

[61] Ian Gibson, David Rosen, Brent Stucker, and Mahyar Khorasani. *Additive manufacturing technologies*, volume 17. Springer, 2014.

[62] Deepak Giri, Musa Jouaneh, and Brent Stucker. Error sources in a 3-D reverse engineering process. *Precision Engineering*, 28:242–251, 2004.

[63] Colin Goodall. Procrustes methods in the statistical analysis of shape. *Journal of the Royal Statistical Society: Series B (Methodological)*, 53(2):285–321, 1991.

[64] Colin R Goodall and Kanti V Mardia. Multivariate aspects of shape theory. *The Annals of Statistics*, pages 848–866, 1993.

[65] Ian Goodfellow, Yoshua Bengio, and Aaron Courville. *Deep learning.* MIT press, Cambridge, MA, 2016.

[66] Robert B Gramacy. *Surrogates: Gaussian Process Modeling, Design, and Optimization for the Applied Sciences.* CRC Press, 2020.

[67] Junkang Guo, Baotong Li, Zhigang Liu, Jun Hong, and Xiaopan Wu. Integration of geometric variation and part deformation into variation propagation of 3-d assemblies. *International Journal of Production Research*, 54(19):5708–5721, 2016.

[68] YS Hong and TC Chang. A comprehensive review of tolerancing research. *International Journal of Production Research*, 40(11):2425–2459, 2002.

[69] Berthold K.P. Horn and Michael J. Brooks. *Shape from shading.* MIT Press, 1989.

[70] Berthold KP Horn, Hugh M Hilden, and Shahriar Negahdaripour. Closed-form solution of absolute orientation using orthonormal matrices. *JOSA A*, 5(7):1127–1135, 1988.

[71] Guang-Bin Huang, Qin-Yu Zhu, and Chee-Kheong Siew. Extreme learning machine: a new learning scheme of feedforward neural networks. *Neural networks*, 2:985–990, 2004.

[72] Guang-Bin Huang, Qin-Yu Zhu, and Chee-Kheong Siew. Extreme learning machine: theory and applications. *Neurocomputing*, 70(1-3):489–501, 2006.

[73] Qiang Huang, Hadis Nouri, Kai Xu, Yong Chen, Sobambo Sosina, and Tirthankar Dasgupta. Statistical predictive modeling and compensation of geometric deviations of three-dimensional printed products. *Journal of Manufacturing Science and Engineering*, 136(6):61008, 2014.

[74] Qiang Huang, Jizhe Zhang, Arman Sabbaghi, and Tirthankar Dasgupta. Optimal offline compensation of shape shrinkage for three-dimensional printing processes. *Iie transactions*, 47(5):431–441, 2015.

[75] Charles W. Hull. Apparatus for production of three-dimensional objects by stereolithography, U.S. Patent US4575330A, Mar. 1986.

[76] Andrés Iglesias, G Echevarría, and Akemi Gálvez. Functional networks for b-spline surface reconstruction. *Future Generation Computer Systems*, 20(8):1337–1353, 2004.

[77] Andrés Iglesias and Akemi Gálvez. Memetic electromagnetism algorithm for surface reconstruction with rational bivariate bernstein basis functions. *Natural Computing*, 16(4):511–525, 2017.

[78] ASTM International. Standard Terminology for Additive Manufacturing Technologies (Withdrawn 2015). Standard, ASTM International, West Conshohocken, PA, 2012.

[79] J Jamshidi, AR Mileham, GW Owen, et al. Dimensional tolerance approximation for reverse engineering applications. In *DS 36: Proceedings DESIGN 2006, the 9th International Design Conference, Dubrovnik, Croatia*, pages 855–862, 2006.

[80] Mohd Javaid and Abid Haleem. Additive manufacturing applications in medical cases: A literature based review. *Alexandria Journal of Medicine*, 54(4):411–422, 2018.

[81] Young-Seon Jeong, Myong K Jeong, Jye-Chyi Lu, Ming Yuan, and Jionghua Jin. Statistical process control procedures for functional data with systematic local variations. *IISE Transactions*, 50(5):448–462, 2018.

[82] Ran Jin, Chia-Jung Chang, and Jianjun Shi. Sequential measurement strategy for wafer geometric profile estimation. *Iie transactions*, 44(1):1–12, 2012.

[83] Yuan Jin, S Joe Qin, and Qiang Huang. Offline predictive control of out-of-plane shape deformation for additive manufacturing. *Journal of Manufacturing Science and Engineering*, 138(12), 2016.

[84] Ian T Jolliffe and Jorge Cadima. Principal component analysis: a review and recent developments. *Philosophical Transactions of the Royal Society A: Mathematical, Physical and Engineering Sciences*, 374(2065):20150202, 2016.

[85] Yongtae Jun. A piecewise hole filling algorithm in reverse engineering. *Computer-aided design*, 37(2):263–270, 2005.

[86] George John Kaisarlis, Stefanos C Diplaris, and Michael M Sfantsikopoulos. Geometrical position tolerance assignment in reverse engineering. *International Journal of Computer Integrated Manufacturing*, 21(1):89–96, 2008.

[87] GJ Kaisarlis, SC Diplaris, and MM Sfantsikopoulos. A knowledge-based system for tolerance allocation in reverse engineering. In *Proceedings of the 33rd International Matador Conference*, pages 527–532. Springer, 2000.

[88] Victor E Kane. Process capability indices. *Journal of quality technology*, 18(1):41–52, 1986.

[89] Mehdi Koosha, Rassoul Noorossana, and Fadel Megahed. Statistical process monitoring via image data using wavelets. *Quality and Reliability Engineering International*, 33(8):2059–2073, 2017.

[90] Samuel Kotz and Norman L Johnson. Process capability indices—a review, 1992–2000. *Journal of quality technology*, 34(1):2–19, 2002.

[91] Venkat Krishnamurthy and Marc Levoy. Fitting smooth surfaces to dense polygon meshes. In *Proceedings of the 23rd annual conference on Computer graphics and interactive techniques*, pages 313–324, 1996.

[92] Atul Kumar, Pramod Kumar Jain, and Pushparaj Mani Pathak. Reverse engineering in product manufacturing: an overview. *DAAAM international scientific book*, 39:665–678, 2013.

[93] Neil D Lawrence. Gaussian process latent variable models for visualisation of high dimensional data. In *Advances in neural information processing systems*, pages 329–336, 2004.

[94] Jacqueline Le Moigne and Allen M Waxman. Projected light grids for short range navigation of autonomous robots. In *Proc. 7th Int. Conf. Pattern Recognition*, pages 203–206, 1984.

[95] Jacqueline Le Moigne and Allen M Waxman. *Multi-resolution grid patterns for building range maps.* Society of Manufacturing Engineers, 1985.

[96] Feng Li, Andrew Peter Longstaff, Simon Fletcher, and Alan Myers. Rapid and accurate reverse engineering of geometry based on a multi-sensor system. *The International Journal of Advanced Manufacturing Technology*, 74(1-4):369–382, 2014.

[97] Lingling Li, Congbo Li, Ying Tang, and Yanbin Du. An integrated approach of reverse engineering aided remanufacturing process for worn components. *Robotics and Computer-Integrated Manufacturing*, 48:39–50, 2017.

[98] Ye Li and Prashanth Reddy Nomula. Surface-opening feature measurement using coordinate-measuring machines. *The International Journal of Advanced Manufacturing Technology*, 79(9):1915–1929, 2015.

[99] Ye Li, Naveen P Surisetti, and Joseph C Chen. Measuring external profiles of porous objects using cmm. *The International Journal of Advanced Manufacturing Technology*, 64(5-8):875–887, 2013.

[100] Ye Li and Yuliang Wei. Scanning data reduction and accuracy enhancement through hybrid probing and bicubic surface construction. *The International Journal of Advanced Manufacturing Technology*, 87(1):303–314, 2016.

[101] Peter Liepa. Filling holes in meshes. In *Proceedings of the 2003 Eurographics/ACM SIGGRAPH symposium on Geometry processing*, pages 200–205, 2003.

[102] Rong-Shine Lin and Y Koren. Efficient tool-path planning for machining free-form surfaces. *Journal of Engineering for Industry*, 118, 1996.

[103] Zone-Ching Lin and Chein-Chung Chen. Collision-free path planning for coordinate measurement machine probe. *International Journal of Production Research*, 39(9):1969–1992, 2001.

[104] Jie Liu, Guan Ping Dong, and Yan Bin Fan. Personalized ring design and rapid manufacturing based on reverse engineering and 3d printing. In *Applied mechanics and materials*, volume 851, pages 599–602. Trans Tech Publ, 2016.

[105] Keqing Lu and Wen Wang. A multi-sensor approach for rapid and precise digitization of free-form surface in reverse engineering. *The International Journal of Advanced Manufacturing Technology*, 79(9):1983–1994, 2015.

[106] Brett Lyons. Additive manufacturing in aerospace: Examples and research outlook. *The Bridge*, 44(3), 2014.

[107] Weiyin Ma and J-P Kruth. Nurbs curve and surface fitting for reverse engineering. *The International Journal of Advanced Manufacturing Technology*, 14(12):918–927, 1998.

[108] Minoru Maruyama and Shigeru Abe. Range sensing by projecting multiple slits with random cuts. *IEEE Transactions on Pattern Analysis and Machine Intelligence*, 15(6):647–651, 1993.

[109] Massimiliano Marziale and Wilma Polini. A review of two models for tolerance analysis of an assembly: Jacobian and torsor. *International Journal of Computer Integrated Manufacturing*, 24(1):74–86, 2011.

[110] Mark H Michalski and Joseph S Ross. The shape of things to come: 3d printing in medicine. *Jama*, 312(21):2213–2214, 2014.

[111] Michael J Milroy, Colin Bradley, Geoffrey W Vickers, and DJ Weir. G1 continuity of b-spline surface patches in reverse engineering. *Computer-Aided Design*, 27(6):471–478, 1995.

[112] Kamran Mohaghegh, MH Sadeghi, and A Abdullah. Reverse engineering of turbine blades based on design intent. *The International Journal of Advanced Manufacturing Technology*, 32(9):1009–1020, 2007.

[113] Douglas C. Montgomery. *Design and Analysis of Experiments*. John Wiley & Sons, 2012.

[114] Douglas C Montgomery. *Introduction to statistical quality control*. John Wiley & Sons, 2020.

[115] Douglas C Montgomery and George C Runger. Gauge capability and designed experiments. Part I: basic methods. *Quality Engineering*, 6(1):115–135, 1993.

[116] Hiroyoshi Morita, Kaanyasn Yajima, and Shojiro Sakata. Reconstruction of surfaces of 3-d objects by m-array pattern projection method. In *1988 Second International Conference on Computer Vision*, pages 468–469. IEEE Computer Society, 1988.

[117] Saeid Motavalli and Bopaya Bidanda. A part image reconstruction system for reverse engineering of design modifications. *Journal of Manufacturing Systems*, 10(5):383–395, 1991.

[118] Saeid Motavalli, Vithaya Suharitdamrong, and Abdalla Alrashdan. Design model generation for reverse engineering using multi-sensors. *IIE transactions*, 30(4):357–366, 1998.

[119] Shree K Nayar and Yasuo Nakagawa. Shape from focus. *IEEE Transactions on Pattern analysis and machine intelligence*, 16(8):824–831, 1994.

[120] Rassoul Noorossana, Abbas Saghaei, and Amirhossein Amiri. *Statistical analysis of profile monitoring*, volume 865. John Wiley & Sons, 2011.

[121] Fergal J O'brien. Biomaterials & scaffolds for tissue engineering. *Materials today*, 14(3):88–95, 2011.

[122] The American Society of Mechanical Engineers. Mathematical Definition of Dimensioning and Tolerancing Prrinciples. Standard, The American Society of Mechanical Engineers, New York, NY, 1994.

[123] The American Society of Mechanical Engineers. Dimensioning and Tolerancing. Standard, The American Society of Mechanical Engineers, New York, NY, 2009.

[124] The American Society of Mechanical Engineers. Engineering Drawing Practices. Standard, The American Society of Mechanical Engineers, New York, NY, 2017.

[125] Joseph O'Rourke. Finding minimal enclosing boxes. *International journal of computer & information sciences*, 14(3):183–199, 1985.

[126] Nikhil R Pal and Sankar K Pal. A review on image segmentation techniques. *Pattern recognition*, 26(9):1277–1294, 1993.

[127] Biranchi N Panda, K Shankhwar, Akhil Garg, and Zhang Jian. Performance evaluation of warping characteristic of fused deposition modelling process. *The International Journal of Advanced Manufacturing Technology*, 88(5-8):1799–1811, 2017.

[128] G Pandya, E Amine Lehtihet, and TM Cavalier. Tolerance design of datum systems. *International journal of production research*, 40(4):783–807, 2002.

[129] Chiwoo Park and Abhishek K Shrivastava. Multimode geometric-profile monitoring with correlated image data and its application to nanoparticle self-assembly processes. *Journal of Quality Technology*, 46(3):216–233, 2014.

[130] Frank L Pedrotti, Leno M Pedrotti, and Leno S Pedrotti. *Introduction to optics.* Cambridge University Press, Cambridge, UK, 2017.

[131] Alan M Polansky. A smooth nonparametric approach to process capability. *Quality and Reliability Engineering International*, 14(1):43–48, 1998.

[132] Alan M Polansky. An algorithm for computing a smooth nonparametric process capability estimate. *Journal of Quality Technology*, 32(3):284–289, 2000.

[133] Wilma Polini and Andrea Corrado. Digital twin of composite assembly manufacturing process. *International Journal of Production Research*, 58(17):5238–5252, 2020.

[134] Peihua Qiu. *Image processing and jump regression analysis*, volume 599. John Wiley & Sons, 2005.

[135] Vinesh Raja and Kiran J Fernandes. *Reverse engineering: an industrial perspective.* Springer Science & Business Media, 2007.

[136] Carsten Reich. 3-D shape measurement of complex objects by combining photogrammetry and fringe projection. *Optical Engineering*, 39(1):224, 2000.

[137] Javier Roca-Pardiñas, Henrique Lorenzo, Pedro Arias, and Julia Armesto. From laser point clouds to surfaces: Statistical nonparametric methods for three-dimensional reconstruction. *Computer-Aided Design*, 40(5):646–652, 2008.

[138] Radu Bogdan Rusu. Semantic 3d object maps for everyday manipulation in human living environments. *KI-Künstliche Intelligenz*, 24(4):345–348, 2010.

[139] Arman Sabbaghi, Tirthankar Dasgupta, Qiang Huang, and Jizhe Zhang. Inference for deformation and interference in 3d printing. *The Annals of Applied Statistics*, pages 1395–1415, 2014.

[140] Arman Sabbaghi, Qiang Huang, and Tirthankar Dasgupta. Bayesian model building from small samples of disparate data for capturing in-plane deviation in additive manufacturing. *Technometrics*, 60(4):532–544, 2018.

[141] Arman Sabbaghi, Qiang Huang, et al. Model transfer across additive manufacturing processes via mean effect equivalence of lurking variables. *Annals of Applied Statistics*, 12(4):2409–2429, 2018.

[142] Mika Salmi. Possibilities of preoperative medical models made by 3d printing or additive manufacturing. *Journal of Medical Engineering*, 2016, 2016.

[143] M Sarfraz. Computer-aided reverse engineering using simulated evolution on nurbs. *Virtual and Physical Prototyping*, 1(4):243–257, 2006.

[144] Muhammad Sarfraz, Syed Arshad Raza, and M Humayun Baig. Computing optimized curves with nurbs using evolutionary intelligence. In *International Conference on Computational Science and Its Applications*, pages 806–815. Springer, 2005.

[145] S. Sartori and G. X. Zhang. Geometric Error Measurement and Compensation of Machines. *CIRP Annals - Manufacturing Technology*, 44(2):599–609, 1995.

[146] Benjamin Schleich and Sandro Wartzack. Evaluation of geometric tolerances and generation of variational part representatives for tolerance analysis. *The International Journal of Advanced Manufacturing Technology*, 79(5):959–983, 2015.

[147] Benjamin Schleich and Sandro Wartzack. Novel approaches for the assembly simulation of rigid skin model shapes in tolerance analysis. *Computer-Aided Design*, 101:1–11, 2018.

[148] Tzung-Sz Shen, Jianbing Huang, and Chia-Hsiang Menq. Multiple-sensor integration for rapid and high-precision coordinate metrology. *IEEE/ASME transactions on mechatronics*, 5(2):110–121, 2000.

[149] Ramandeep Singh, Britty Baby, Ashish Suri, and Sneh Anand. Comparison of laser and structured light scanning techniques for neurosurgery applications. In *2016 3rd International Conference on Signal Processing and Integrated Networks (SPIN)*, pages 301–305. IEEE, 2016.

[150] H Sirringhaus, T Kawase, RH Friend, T Shimoda, M Inbasekaran, W Wu, and EP Woo. High-resolution inkjet printing of all-polymer transistor circuits. *Science*, 290(5499):2123–2126, 2000.

[151] Jerzy Sładek, Paweł M Błaszczyk, Magdalena Kupiec, and Robert Sitnik. The hybrid contact–optical coordinate measuring system. *Measurement*, 44(3):503–510, 2011.

[152] R Smith, Steven W McCrary, and R Neal Callahan. Gauge repeatability and reproducibility studies and measurement system analysis: a multimethod exploration of the state of practice. *Journal of Industrial Technology*, 23(1):2–12, 2007.

[153] Emilio Soria-Olivas, Juan Gomez-Sanchis, José D Martin, Joan Vila-Frances, Marcelino Martinez, José R Magdalena, and Antonio J Serrano. BELM: Bayesian

extreme learning machine. *IEEE Transactions on Neural Networks*, 22(3):505–509, 2011.

[154] Venugopal Srinivasan, Hsin-Chu Liu, and Maurice Halioua. Automated phase-measuring profilometry of 3-d diffuse objects. *Applied optics*, 23(18):3105–3108, 1984.

[155] TS Srivatsan and TS Sudarshan. *Additive manufacturing: innovations, advances, and applications.* CRC Press, 2015.

[156] Charles Stein et al. The admissibility of hotelling's t^2-test. *The Annals of Mathematical Statistics*, 27(3):616–623, 1956.

[157] Richard Szeliski. *Computer vision: algorithms and applications.* Springer Science & Business Media, 2010.

[158] Shouhong Tang and Yau Y Hung. Fast profilometer for the automatic measurement of 3-d object shapes. *Applied Optics*, 29(20):3012–3018, 1990.

[159] Jos MF Ten Berge. Orthogonal procrustes rotation for two or more matrices. *Psychometrika*, 42(2):267–276, 1977.

[160] Adam Thompson, Ian Maskery, and Richard K Leach. X-ray computed tomography for additive manufacturing: a review. *Measurement Science and Technology*, 27(7):072001, 2016.

[161] Beau Tippetts, Dah Jye Lee, Kirt Lillywhite, and James Archibald. Review of stereo vision algorithms and their suitability for resource-limited systems. *Journal of Real-Time Image Processing*, 11(1):5–25, 2016.

[162] Kun Tong, Sanjay Joshi, and E Amine Lehtihet. Error compensation for fused deposition modeling (fdm) machine by correcting slice files. *Rapid Prototyping Journal*, 2008.

[163] Kun Tong, E Amine Lehtihet, and Sanjay Joshi. Parametric error modeling and software error compensation for rapid prototyping. *Rapid Prototyping Journal*, 2003.

[164] Pingfang Tsai. Variable gauge repeatability and reproducibility study using the analysis of variance method. *Quality Engineering*, 1(1):107–115, 1988.

[165] Erkan Ülker and Veysi İşler. An artificial immune system approach for b-spline surface approximation problem. In *International Conference on Computational Science*, pages 49–56. Springer, 2007.

[166] Adrián Uriondo, Manuel Esperon-Miguez, and Suresh Perinpanayagam. The present and future of additive manufacturing in the aerospace sector: A review of important aspects. *Proceedings of the Institution of Mechanical Engineers, Part G: Journal of Aerospace Engineering*, 229(11):2132–2147, 2015.

[167] S S Vallender. Calculation of the Wasserstein distance between probability distributions on the line. *Theory of Probability & Its Applications*, 18(4):784–786, 1974.

[168] Tamas Varady, Ralph R Martin, and Jordan Cox. Reverse engineering of geometric models—an introduction. *Computer-aided design*, 29(4):255–268, 1997.

[169] Rene Vidal, Yi Ma, and Shankar Sastry. Generalized principal component analysis (gpca). *IEEE transactions on pattern analysis and machine intelligence*, 27(12):1945–1959, 2005.

[170] Jianjun Wang, Ting Mao, and Yiliu Tu. Simultaneous multi-response optimisation for parameter and tolerance design using bayesian modelling method. *International Journal of Production Research*, pages 1–25, 2020.

[171] Kai Wang and Fugee Tsung. A cost-effective and reliable measurement strategy for 3d printed parts by integrating low-and high-resolution measurement systems. *IISE Transactions*, 50(10):900–912, 2018.

[172] Kun Wang, Guilong Li, Shichang Du, Lifeng Xi, and Tangbin Xia. State space modelling of variation propagation in multistage machining processes for variable stiffness structure workpieces. *International Journal of Production Research*, pages 1–20, 2020.

[173] Christopher K I Williams and Carl Edward Rasmussen. Gaussian processes for regression. In *Advances in neural information processing systems*, pages 514–520, 1996.

[174] J Michael Wilson, Cecil Piya, Yung C Shin, Fu Zhao, and Karthik Ramani. Remanufacturing of turbine blades by laser direct deposition with its energy and environmental impact analysis. *Journal of Cleaner Production*, 80:170–178, 2014.

[175] Christian Wöhler and Kia Hafezi. A general framework for three-dimensional surface reconstruction by self-consistent fusion of shading and shadow features. *Pattern Recognition*, 38(7):965–983, 2005.

[176] TT Wohlers, I Campbell, O Diegel, R Huff, and J Kowen. *Whohlers Report 2019*. Wohlers Associates, 2019.

[177] Svante Wold, Kim Esbensen, and Paul Geladi. Principal component analysis. *Chemometrics and intelligent laboratory systems*, 2(1-3):37–52, 1987.

[178] William H Woodall. Current research on profile monitoring. *Production*, 17(3):420–425, 2007.

[179] William H Woodall, Dan J Spitzner, Douglas C Montgomery, and Shilpa Gupta. Using control charts to monitor process and product quality profiles. *Journal of Quality Technology*, 36(3):309–320, 2004.

[180] Chien-Wei Wu, WL Pearn, and Samuel Kotz. An overview of theory and practice on process capability indices for quality assurance. *International journal of production economics*, 117(2):338–359, 2009.

[181] Mei-Fang Wu, Hsuan-Yu Chen, Tsang-Chuan Chang, and Chih-Feng Wu. Quality evaluation of internal cylindrical grinding process with multiple quality characteristics for gear products. *International Journal of Production Research*, 57(21):6687–6701, 2019.

[182] Haifeng Xia, Yu Ding, and Bani K Mallick. Bayesian hierarchical model for combining misaligned two-resolution metrology data. *IIE Transactions*, 43(4):242–258, 2011.

[183] Xun Xu. *Integrating Advanced Computer-Aided Design, Manufacturing, and Numerical Control: Principles and Implementations: Principles and Implementations*. IGI Global, 2009.

[184] Hao Yan, Kamran Paynabar, and Jianjun Shi. Image-based process monitoring using low-rank tensor decomposition. *IEEE Transactions on Automation Science and Engineering*, 12(1):216–227, 2014.

[185] Wai Yee Yeong and Chee Kai Chua. *Bioprinting: principles and applications*, volume 1. World Scientific Publishing Co Inc, 2014.

[186] Mingrang Yu, Yingjie Zhang, Yunlong Li, and Ding Zhang. Adaptive sampling method for inspection planning on cmm for free-form surfaces. *The International Journal of Advanced Manufacturing Technology*, 67(9-12):1967–1975, 2013.

[187] Yizhou Yu and Johnny T Chang. Shadow graphs and 3d texture reconstruction. *International Journal of Computer Vision*, 62(1-2):35–60, 2005.

[188] Xiaowei Yue, Jin Gyu Park, Zhiyong Liang, and Jianjun Shi. Tensor mixed effects model with application to nanomanufacturing inspection. *Technometrics*, 62(1):116–129, 2020.

[189] Yangyang Zang and Peihua Qiu. Phase i monitoring of spatial surface data from 3d printing. *Technometrics*, 60(2):169–180, 2018.

[190] Yangyang Zang and Peihua Qiu. Phase ii monitoring of free-form surfaces: An application to 3d printing. *Journal of Quality Technology*, 50(4):379–390, 2018.

[191] Pai Zheng, Zhiqian Sang, Ray Y Zhong, Yongkui Liu, Chao Liu, Khamdi Mubarok, Shiqiang Yu, Xun Xu, et al. Smart manufacturing systems for industry 4.0: Conceptual framework, scenarios, and future perspectives. *Frontiers of Mechanical Engineering*, 13(2):137–150, 2018.

[192] Yin Zhongwei. Direct integration of reverse engineering and rapid prototyping based on the properties of nurbs or b-spline. *Precision Engineering*, 28(3):293–301, 2004.